# MEASUREMENT OF ELASTIC PROPERTIES OF HARD FILMS USING BRILLOUIN SCATTERING

**Wenjun Pang**

*A thesis submitted to the Faculty of Science*
*University of the Witwatersrand, Johannesburg*
*in fulfilment of the requirements for the degree of*

**Doctor of Philosophy**

Johannesburg, 1997

# DECLARATION

I declare that this thesis is my own, unaided work. It is being submitted for the degree of Doctor of Philosophy in the University of the Witwatersrand, Johannesburg. It has not been submitted previously for any degree or examination in any other university.

(Signature of candidate)

10 Day of Jan 1992

# Abstract

Brillouin scattering of light is used to study the various surface acoustic modes that are predicted theoretically to be supported by $TiN$ thin films on high speed steel ($HSS$). Information is thereby obtained on the elastic properties and adhesion of the films, which range in thickness from $20nm$ to $4180nm$. A Green's function method, invoking the surface ripple mechanism for the inelastic scattering of light, is used to calculate the Brillouin spectrum for scattering from the surface acoustic excitations. For the $TiN/HSS$ combination, guided modes take the form of true SAW, highly damped p-SAW, "pre-Rayleigh" and "quasi-Rayleigh" and its higher order modes as the film thickness increases. On comparison between the measured and calculated dispersion relation, excellent agreement is found for the thicker films ($> 870nm$) and bare substrates, but the measured SAW velocities have lower values than calculated for thinner films ($< 500nm$). This implies that the elastic moduli of the thicker films are close to those of bulk $TiN$, but the effective elastic moduli of the thinner films decrease with reducing film thickness. This conclusion is reinforced by backscattering measurements of Brillouin spectra at incident angles between 50° and 80° for a film thickness of $350nm$, in which p-SAW and its higher order modes are present as double peaks in the spectrum. The lower measured sound velocities for the thinner films are attributed to a reduction in the effective elastic moduli of $TiN$ caused, most likely, by compositional variations at the interface.

Brillouin scattering measurements are also presented of the SAW velocity of $TiN$ hard films on steel as a function of nitrogen partial pressure during film growth and temperature. Good correlation has been found between the SAW velocity and residual stress and adhesion force (critical load) of the films. The residual stress in the films has a trend opposite to that of the SAW velocity while the adhesion force has the same trend as that of the SAW velocity. This indicates that Brillouin scattering can be used as a nondestructive method for investigating the mechanical properties of coatings. High-temperature (up to $600°C$) SAW velocities of a thick $TiN$ film are measured using Brillouin scattering and the temperature dependence of the elastic constants of $TiN$ deduced for the first time. There is a downward trend of the SAW velocity and hence elastic moduli with increasing temperature.

The initial chapters provide the fundamental theoretical background of the theory of elasticity, but also include original work of relevance and importance to the studies undertaken. Averaged elastic constants have been calculated for a polycrystal solid from a single crystal elastic constants for both random and preferred orientations of the crystallites, using a tensor averaging method. For the first time, the algebraic results of the averaged elastic constants for crystallites of any symmetry are obtained through symbolic computation. The three dimensional computer visualization of the slowness of bulk $TiN$ is plotted to show the effects of anisotropy in the wave propagation behaviour of $TiN$. Four different methods of recovering the elastic constants of crystals from measured bulk velocity data are compared and discussed. It is found that some methods can be applied in the general case while others are only effective in limited situations.

# Dedication

To MY PARENTS

Zhenjie Pang and Furong Zhang

献给我的父母

庞振杰（父）　　张芙蓉（母）

# Acknowledgment

I would like to thank my supervisors Prof. A. G. Every and Prof. J. D. Comins for their expert guidance, their financial support, and for what I have learned from them. I am deeply grateful to Mr. D. Pietersen and Mr. P. Marais for their kind assistance in preparing the hard film samples, and to my colleague, Mr. P.R. Stoddart whose contribution to the experimental arrangement was invaluable to my work. Prof. J. M. Witcomb, Mr. S. H. Coetzee, Ms. J. M. Salemi, Mr. W. Louw, Mr. M. van Staden, Prof. T. E. Derry and Mr. D. B. Rebuli are acknowledged for their assistance with SEM, EDX, X-ray diffraction, XPS and Rutherford backscattering. I am also grateful to all the staff in the mechanical, electronics and grass blowing workshops for the construction of apparatus and their assistance. I wish to thank my parents and my wife for their constant support and encouragement throughout this work.

# Contents

# List of Figures

# List of Tables

# Chapter 1

# Introduction

Hard ceramic films, which usually refer to group IVB transition metal carbides and nitrides such as $TiN$, $TiC$ and $TiAlN$ etc., are widely used as protective coatings to minimize wear and corrosion on drill bits, bearings and other machine components. They render protection due to their very high hardness ($Hv > 2100\ kg/mm^2$) and chemical inertness [1]. Among these materials, $TiN$ films are the most widely studied and their use as diffusion barriers in silicon integrated circuits [2] and as a high temperature photothermal conversion material [3] has also been explored. Extensive researches on the structure [4], the properties such as hardness, adhesion, electric resistivity and optical reflectivity of $TiN$ films have been done in the past [5]. However, the study of the elastic properties of this type of film, and their dependence on internal stress, crystalline defects, preferential crystallographic orientation and adhesion are fairly sparse. Most earlier studies concerning the elastic properties of ceramic films were carried out by X-ray residual stress measurements using the Bragg X-Ray Diffraction(XRD) geometry [6] - [8] or using the Seemann-Bohlin focusing geometry

[9]. Kim et al. [10]-[11] have determined the elastic constants of single crystal $TiN$ by the line-focus acoustic microscopy technique.

The investigation of the elastic properties of the $HSS$ coated with $TiN$ is of practical significance. This combination is widely used in industry for cutting tools and drill bits, which are exposed to considerable impact and abrasion forces in operating conditions well above room temperature. The residual stress state in a $TiN$ film is crucial to its properties of adhesion, anti-corrosion and wear resistance. Using the surface Brillouin scattering technique to derive the elastic properties from the various acoustic modes can provide important information regarding the physical and mechanical properties of the films.

Brillouin scattering is the inelastic scattering of light by thermally excited acoustic phonons in solids. This interaction was first investigated early this century by Brillouin (1922) and Mandelshtam (1926), and has received considerable interest since the advent of the laser as a powerful source of monochromatic light. The measurements of Brillouin scattering signals were mainly restricted to bulk modes of transparent materials at both ambient [12]-[13] and high temperature [14]-[16] until the tandem multipass Fabry-Perot interferometer with high resolution and a large free spectral range became available in 1978, allowing the detection of thermally excited surface acoustic phonons in opaque solid materials [17]. For opaque materials the scattering occurs at or near the surface and is usually sensitive to the dynamic response of a few hundreds of atomic layers of the surface. Brillouin scattering is an ideal technique for characterizing thin films and near surface properties affected by radiation damage, ion-implantation and ion exchange, mechanical polishing and other surface

modifications [18]-[20]. The use of conventional ultrasonic techniques in these situations is difficult because of the large wavelength in relation to the layer thickness. Brillouin scattering is also a valuable nondestructive evaluation (NDE) technique for the characterization of materials at high temperatures and pressures.

It has been reported that the use of surface Brillouin scattering as a valuable tool for the characterization of the physical and mechanical properties of bulk solids of semiconductors [21] and metals [22]-[23], thin supported solid films, [24]-[27], unsupported films [28]-[29], interfaces [30]-[31] and multilayers [32]. High-temperatures Brillouin scattering measurements of opaque solids have also been presented [33]-[34]. Surface Brillouin scattering probes thermally excited phonons in the $GHz$ frequency range which give rise to surface displacements in opaque or semi-opaque materials. Where there is little penetration of the light into the medium, the scattering is mediated principally by the surface ripple mechanism. Depending on the substrate and film combination, there are various acoustic excitations localized near the surface that can be probed, including Rayleigh or surface acoustic waves (SAWs), Sezawa waves [35]-[36], Lamb waves, pseudo-surface acoustic waves (p-SAWs) and Stoneley waves. By analyzing Brillouin scattering (BS) spectra, identifying the presence of particular acoustic modes and comparing these with calculations, one can extract information pertaining to the texture, adhesion, stress, film thickness and elastic properties of supported solid films [37]-[40].

The theory of Brillouin scattering from surface acoustic phonons in opaque bulk materials due to the "ripple mechanism" was first developed by Loudon through the Green's function approach in 1978 [41] and by Marvin et al. [42] using a direct

matching of the electromagnetic field at the surface. Bortolani et al. [43] followed the latter treatment to extend the theory to the supported films by taking all the possible scattering mechanisms into account, i.e. the scattering from the surface and interface ripples and elasto-optic coupling in the film and in the substrate. This theory explains the experimental results for transparent $SiO_2$ films on a Si substrate [44] very well while the scattering from metallic surfaces like aluminum has been successfully explained in term of ripple mechanism only. It is found in their study that there is strong interference between the ripple and elasto-optic contributions to the scattering amplitude.

A theoretical study of elastic wave propagation in bounded media involves solving the wave equation with appropriate boundary conditions on the basis of elastic continuum theory [45]. Surface waves on the free surface of an elastic half-space are known as "Rayleigh waves" and have been extensively studied and the results of many numerical calculations have been published [46]. Elastic wave propagation in a plate and in a thin layer on a substrate has also been investigated with more complicated boundary conditions being taken into account [47], [48]. In this work, numerical calculations for dispersion relations ($v$ vs. $k_{\|}h$) are limited to true surface modes (Rayleigh waves) which are available only in a narrow range of $k_{\|}h$, where $k_{\|}$ is the component of wavevector parallel to the surface.

The use of surface Brillouin scattering to study the elastic behaviour of $TiN$ films on glass substrates [49], on <111> oriented silicon wafers [50] and $TiN/(V_zNb_{1-x})N$ superlattices [51] has been reported recently. In these measurements, only true SAWs have been reported, and then only for a very limited range of film thicknesses and no

systematic study has been done on the elastic properties of hard films both experimentally and theoretically using Brillouin scattering.

Interest has grown recently to study the fast-on-slow system. The $CaF_2/GaAs(111)$ heterostructure [52] was investigated using Brillouin scattering, where a pre-Rayleigh mode was identified. Recent acoustic microscopy studies of leaky surface waves in $AlO/Al$ [53]-[54] and $TiN$ coatings on steel [55]-[56] are presented. A theoretical study has been reported of the leaky p-SAWs by looking for dips in the magnitude of the reflectance function [57].

In this study, we have conducted Brillouin scattering measurements of the SAW velocity of $TiN$ hard films on steel as a function of film thickness, nitrogen partial pressure used in the deposition process, and temperature. This is an example of a fast on slow system in which the layer has the effect of increasing the SAW velocity over that of the substrate. We have been drawn to this combination because of its important practical applications, and also because it offers a "stiffening" situation where the existence of the film increases the SAW velocity over that of the substrate. In contrast to the case of softening, little has been published on the effects of stiffening, particularly with regard to pseudo-SAWs and their higher order modes in the region beyond where the Rayleigh wave degenerates into the bulk wave continuum. From these measurements, we have obtained information about the variation of the effective elastic constants of $TiN$ with film thickness, for thick films the correlation between the SAW velocity and residual stress and adhesion force (critical load), and elastic constants of $TiN$ films as a function of temperature.

In order to interpret the experimental results, we use a Green's function method to

predict surface displacement amplitudes and Brillouin scattering spectra of acoustic excitations at the surface. For $TiN$ films deposited on high speed steel, ripple scattering at the free surface dominates elasto-optic scattering in the film. By taking into account ripple scattering at the surface only, we have calculated the Brillouin spectra and the dispersion relation of $TiN$ polycrystalline films on $HSS$, and the results enable us to identify the existence of a p-SAW, "pre-Rayleigh", and their higher order modes [52] in this system. It is found that the elastic constants of the $TiN$ film have a profound effect on the acoustic behaviour of $TiN/HSS$. There is a discontinuity in the calculated dispersion curve for normal $TiN/HSS$ - a strong stiffening system where the shear velocity of the film is much greater than that of the substrate, but not for reduced $TiN$ elastic moduli on $HSS$ - a relatively weak stiffening system. There is a "pre-Rayleigh" mode existing only under the strong stiffening system in the discontinuity region of the dispersion curve. However, the acoustic modes in both situations evolve into a "quasi-Rayleigh" wave of the corresponding systems at large $k_{\|}h$, which are very close to the Rayleigh waves of $TiN$.

The samples used in the measurements of the dispersion relation were prepared using the D.C. magnetron sputtering technique with three $Ti$ targets and a bias voltage of $70V$ at a temperature of approximately $250°C$. A rotational shutter system was designed and mounted inside the deposition chamber in order to have most of the samples deposited under exactly the same conditions. Samples of the stressed $TiN_x$ films were deposited on both mild and $HSS$ in $Ar/N_2$ plasma by a hollow cathode discharge plating. Various states of stress and composition in $TiN_x$ films were obtained by altering the nitrogen partial pressure in the deposition process from

$6.7 \times 10^{-3}$ to $6.0 \times 10^{-1}$ $Pa.$, while keeping the substrate at temperature $500°C$ and negatively biased at $-50V$. The coated samples were further mechanically polished to a flatness of $0.05\mu m$ using diamond and $Al_2O_3$ powders in order to reduce the elastic scattering of light and detect the weak inelastic scattering peaks in the spectrum.

The topography and chemical composition of $TiN$ films are investigated using SEM and EDX-ray techniques. The rather complicated compositional variations at the interface region are investigated by XPS measurements as a function of depth on the samples of various thicknesses, showing there is mixing region at $TiN/HSS$ interface with $TiO$ and/or $TiO_2$ being the largest components which are about 100nm thick for most of samples. The preferred orientation of $TiN$ polycrystalline films is detected using the X-Ray diffraction technique. The deviation of the lattice parameter of the films from that of a single crystal is explained in terms of stress in the films formed in the deposition procedure. With the deposition rate approximately $0.12\mu m$ $min^{-1}$, a figure we arrive at on the basis of measurements on thick films, the film thicknesses are controlled by the deposition time, i.e. the period in which the shutter is open to a sample. The thicknesses of the films are subsequently confirmed using SEM on sample fracture sections and Rutherford backscattering measurements where the bulk density of $TiN$ is assumed. XPS depth profile measurements can also provide the thickness ratio between the samples. Based on an accurately measured thickness for a thick sample, the thicknesses of the rest of the samples can be inferred. The values of the film thicknesses obtained from different methods conform reasonably well.

In practice, the film thickness is one of the most important parameters to be ob-

served since it affects the acoustic behaviour and internal stress in the films directly. It is necessary to study the dependence of the elastic properties on the thickness of films. This can be done through the measurements of the dispersion relations from the surface acoustic modes using the Brillouin scattering. With a convenient backscattering geometry, the dispersion relation ($v$ vs. $k_{\parallel}h$) is obtained from the measured peak positions (frequency shifts) of the inelastically scattered light in a spectrum and thus the wave velocity as a function of film thickness. For room temperature measurements, the samples were kept in air and the incident light was focused on the surface by a 50mm focal length lens of aperture f/2.3. In the back scattering geometry, the scattered light was collected by the same lens.

For the $TiN/HSS$ system, we have conducted Brillouin scattering measurements on various acoustic modes for $TiN$ thickness ranging from $20nm$ to $4180nm$. With increasing film thickness $h$, the Rayleigh wave of $HSS$ increases in velocity and then merges into the bulk wave continuum and becomes a highly damped p-SAW. Its higher order modes can also be observed which are shown as double or a series of peaks in the spectrum. The Rayleigh mode of bulk $TiN$ is measured for even larger film thicknesses. A comparison between the measured and calculated Brillouin spectra reveals that the elastic moduli of the thicker films are close to those of bulk $TiN$, but the effective elastic moduli of the thinner films ($< 500nm$) are found to decrease with reducing film thickness, being overall about 25% smaller than those of bulk $TiN$. This conclusion is reinforced by backscattering measurements of Brillouin spectra at incident angles between 50° and 80° for a film thickness of $350nm$. A possible explanation for the lowered elastic moduli of the thinner films could be composition

variations at the $TiN/HSS$ interface [59]. It is clear from the measured results that there is good mechanical contact between the $TiN$ and $HSS$, since otherwise the SAW velocity would drop below that of the substrate for the thinner films.

As an extension to the usefulness of Brillouin scattering in the characterization of mechanical properties in engineering, we have carried out Brillouin scattering measurements on $TiN_x$ films on both mild and high speed steel as a function of the nitrogen partial pressure during deposition. All the films in these measurements were $3.5\mu m$ thick, a typical thickness in tool coating applications. The lattice parameter and preferred orientation of the $TiN_x$ films were measured using X-ray diffraction and the compressive stress determined using the $\sin^2\theta$ method [60]. The stress in the films has a trend opposite to that of the SAW velocity. The adhesion force of the film to the substrate is measured by the critical load method which has the same trend as that of the SAW velocity. The critical load $Lc$ is defined as the smallest load at which the film is damaged when an increasingly loaded diamond stylus is drawn across the film. The damage is judged by emitted acoustic signals. The good correlation between the SAW velocity and stress and critical load indicates that Brillouin scattering can thus be used as a nondestructive method for investigating the stress states and adhesion force of coatings.

Since the working temperature of a $TiN$ protective coating on cutting tools is usually fairly high, it is of practical significance to study their elastic properties at high temperatures. For the first time, the elastic constants of thick $TiN$ films at temperatures up to $600^{\circ}C$ have been extracted from measured SAW velocities. There is a downward near-linear trend in the SAW velocity and hence elastic moduli with

increasing temperature. In our high-temperature measurements the samples were mounted in a specially designed optical furnace with rotatable sample holder and a 120$mm$ focal length lens of aperture f/5.3 was used to illuminate the sample and collect the scattered light. The sample temperature was monitored by a thermocouple placed adjacent to the sample. A temperature controller was used to maintain thermal stability of better than 1°$C$ during the rather lengthy measurement series.

In the theoretical calculations of Brillouin scattering spectrum, the elastic constants of the polycrystalline $TiN$ film must be known first. This raises the subject of the average of elastic constants of the polycrystalline aggregates from the single crystal data which are available from references [7] and [11]. Polycrystalline aggregates with randomly distributed crystallites and preferred orientations are both discussed. For the first time, the algebraic results of the averaged elastic constants for crystallites of any symmetry are obtained through symbolic computation.

Prior to discussions of surface acoustic wave (SAW) propagation problems, the basic knowledge of wave propagation in bulk modes of anisotropic solids is necessary. Computer visualization of 2$D$ and 3$D$ slowness surfaces is used to illustrate the wave propagation behaviour in an arbitrary direction on any of the crystal planes. It is also useful in deciding where the Rayleigh velocity exists in a half space of anisotropic media for the surface wave problem [61]. In addition, the anisotropy ratio for a medium can easily be estimated from the 3-dimensional slowness surfaces. This has be done for cubic $TiN$ showing that it can be simplified to the isotropic case for the purpose of calculating acoustic modes in a supported film.

One of the objectives of the project was to develop an algorithm for inverting SAW

velocity data to obtain elastic constants. As a preliminary to this it was deemed useful to carry out a comparative review of the methods that are available for extracting the elastic constants of anisotropic solids from bulk velocity data [62] - [66]. The convergence of each of the algorithms of the four methods was studied through numerical computation with a set of synthetic velocity data. It is found that some of the methods can be applied in the general case while others are only effective in limited situations. From a practical point of view, the best method of extracting elastic constants is a hybrid one. If possible, the measurements should first be chosen along the highly symmetry directions such as crystal axes, in which some of the elastic constants can be obtained. The numerical computation for the rest of elastic constants by measuring the phase velocities of waves propagating in any arbitrary directions can be much simplified if these elastic constants are known.

As a basis of understanding SAW in solid films, we use a classical method [46] to study the SAW propagation in a half space medium and illustrate the numerical seeking procedure for the SAW velocity. The angular dispersion curves are calculated for cubic $TiN$ on any crystal plane by this method. For the $TiN/HSS$ combination, a classical method has been used to calculate dispersion relations on the basis of the averaged elastic constants of polycrystal $TiN$ films with the boundary conditions at the upper free surface and the interface between the film and substrate being taken into account. This method is easily understood and forms a useful base for the understanding the propagation nature of guided acoustic modes. The classical method involves seeking the boundary determinant minimums on the basis of wave equations in an elastic continuum while the Green's function method based on the scattering

mechanism for a supported film. The latter theory is developed for the most general case of an elastically anisotropic film on an anisotropic substrate, although for the particular problem we address here, both are shown to be effectively isotropic. Comparison between the results from the two methods reveals that the Green's function approach can provide the details of the higher order acoustic modes in addition to p-SAW. The calculated results using the Green's function method successfully explain the measured various acoustic modes for the thick films and bare substrate, and also for the thinner films as suitably reduced effective elastic moduli are used.

In this thesis, methods of averaging elastic constants of polycrystalline aggregates with random distributions of crystallites and also with preferred orientation distribution are developed in chapter 2. In chapter 3, basic information on elastic wave propagation in bulk modes of anisotropic solids is provided through the computer visualization of slowness surfaces and the extraction of elastic constants from bulk velocity data in arbitrary directions is discussed. Chapter 4 describes the basic concept of SAWs using a classical model and the calculations of the SAW velocity as a function of propagation directions. Here extensive numerical calculations of SAW velocities of crystal $TiN$ and $TiN/HSS$ are carried out using a suitable seeking procedure. In chapter 5, the theory of Brillouin scattering and scattering mechanism are outlined. The calculations of the inelastic scattering of light from a supported film are described in details using a Green's function method on the basis of ripple scattering mechanism at the free surface. Brillouin spectra and dispersion relation have been calculated for $TiN/HSS$ system, where p-SAW, pre-Rayleigh and their higher order modes are identified. In chapter 6, the kinematics of the inelastic scattering of

light and experimental arrangement are outlined. The details of sample preparation and physical properties are discussed in chapter 7. Brillouin scattering measurements of various acoustic modes of $TiN/HSS$ as a function of thickness, nitrogen partial pressure in deposition process and temperature are presented in chapter 8. These results are compared with theoretically calculated values. The thesis is concluded in chapter 9.

# Chapter 2

# Elastic Properties of Various Types of Polycrystalline Aggregates

The tensor averaging method is used here to calculate the elastic constants of polycrystalline aggregates from the known elastic constants of single crystals for different orientation distributions of crystallites, i.e. a random distribution or with preferred orientation. Based on Voigt's assumption (a uniform strain field) and Reuss' assumption (a uniform stress field), two different averaging methods of elastic constants are developed. To carry out the calculation, knowledge of the rotation of the elastic constant tensor of crystallites with different orientations to fixed axes is necessary. It is the first time, as far as we know, that the algebraic results for the average elastic constants of any crystal classes have been obtained directly by symbolic computation rather than from an analytical method or numerical computation. Suitable computer programs have been coded to carry out the complex computation involved. As an application of these methods, the elastic constants of polycrystalline aggre-

gates of randomly distributed trigonal crystals and some hard ceramic films with $< 111 >$preferred orientation are calculated. The obtained results will be used to study the elastic wave propagation properties of hard films in latter chapters.

## 2.1 Random Distribution of Crystallites

### 2.1.1 Rotation of Elastic Constant Tensors in an Arbitrary Coordinate System

For a random distribution of crystallites, the distribution function $f(\theta, \phi, \psi)$, which describes statistically the way in which the basic units are aggregated, is a constant. Thus the average has to be made over all the orientations of crystal axes of crystallites with respect to a fixed specimen axes. Three Euler angles $(\theta, \phi, \psi)$ are involved in order to specify the transformation relationship between the crystal axes $x_i$ of any crystallites in the aggregate and the orthogonal reference axes $X_i$ of a macroscopic polycrystalline specimen by a set of direction cosines functions $a_{ij}(\theta, \phi, \psi)$ as follows:

$$
\begin{aligned}
&a_{11} = \cos\psi\cos\phi - \sin\psi\sin\phi\cos\theta, \quad a_{12} = \sin\psi\cos\phi + \cos\psi\sin\phi\cos\theta, \\
&a_{13} = \sin\phi\sin\theta, \qquad\qquad a_{21} = -\cos\psi\sin\phi - \sin\psi\cos\phi\cos\theta, \\
&a_{22} = -\sin\psi\sin\phi + \cos\psi\cos\phi\cos\theta, \qquad\qquad a_{23} = \cos\phi\sin\theta, \\
&a_{31} = \sin\psi\sin\theta, \qquad a_{32} = -\cos\psi\sin\theta, \qquad a_{33} = \cos\theta.
\end{aligned}
\tag{2.1}
$$

If $c_{ijkl}$ and $s_{ijkl}$ are the fourth rank elastic stiffness tensor and compliance tensor respectively with respect to the $x_i$ axes, the elastic tensors $c'_{mnop}$ and $s'_{mnop}$ referred

to axes $X_i$ are then given by reference [67] as

$$c'_{mnop} = a_{mi}\, a_{nj}\, a_{ok}\, a_{pl}\, c_{ijkl}$$
$$s'_{mnop} = a_{mi}\, a_{nj}\, a_{ok}\, a_{pl}\, s_{ijkl}. \tag{2.2}$$

The usual convention regarding summation over repeated subscripts is used here, with $i, j, k, l = 1, 2, 3$.

### 2.1.2 Algorithm of Averaging of Elastic Constants by Symbolic Computation

For a random distribution, the orientations of the crystallites (i.e. their crystal axes $x_i$ ) in an aggregate are supposed to fill all of space, thus the average is carried out by integrating $c'_{mnop}$ or $s'_{mnop}$ through the range of $0 \leq \theta \leq \pi$, $0 \leq \phi \leq 2\pi$, and $0 \leq \psi \leq 2\pi$. Under a uniform strain field(Voigt's assumption), the average stiffness constants $\overline{c_{mnop}}$ of the polycrystalline material are expressed as:

$$\overline{c_{mnop}} = \frac{\int_0^{2\pi}\int_0^{\pi}\int_0^{2\pi} c'_{mnop}\, f(\theta,\phi,\psi)\, \sin\theta\, d\phi\, d\theta\, d\psi}{8\pi^2} \tag{2.3}$$

Similarly, under a uniform stress field (Reuss' assumption), the average compliance constants $\overline{s_{mnop}}$ of the polycrystalline material are expressed as:

$$\overline{s_{mnop}} = \frac{\int_0^{2\pi}\int_0^{\pi}\int_0^{2\pi} s'_{mnop}\, f(\theta,\phi,\psi)\, \sin\theta\, d\phi\, d\theta\, d\psi}{8\pi^2}. \tag{2.4}$$

It is found that stiffness constants such as $c_{1111}$and $c_{2323}$ from Voigt's assumption always exceed those from Reuss' assumption, i.e. $c^v_{1111} \geq [[\overline{s_{1111}}]]^{-1}$ etc. Each $[[\overline{s_{mnop}}]]^{-1}$ is an element of the inverse of matrix $[\overline{s_{mnop}}]$,or a stiffness constant by the inversion of compliance constant matrix obtained using formulae (2.4). Similarly, we

have that the compliance constants such as $s_{1111}$and $s_{2323}$ obtained from Reuss' assumption always exceed those from Voigt's assumption, i.e.$|\overline{s_{2323}}| \geq |[[\overline{c_{2323}}]]^{-1}|$ etc. A very successful prediction but without any rigorous justification is taking the average elastic constants to be the arithmetical mean of the values obtained from the Voigt and Reuss averages.

### 2.1.3 Application to Crystallites with Trigonal Symmetry

As an example, we calculate the average stiffness constants of aggregates of trigonal (32 point group) crystals under Voigt's assumption. The calculation is carried out symbolically, the specific values of elastic constants are unnecessary. For randomly distributed crystallites, the distribution function $f(\theta, \phi, \psi)$ is a constant and is chosen to be 1 in the latter calculations. The six non-zero independent stiffness constants of the crystals of the 32 point group symmetries are (in abbreviated notations) $c_{11}$, $c_{33}$, $c_{44}$, $c_{12}$ ,$c_{13}$ and $c_{14}$. The tensor notation of these stiffness constants needs to be resumed in order to carry out the transformation (see reference [67] for the convention of the relation between $c_{ij}$ and $c_{ijkl}$).

If the axes of a crystallite $x_i$ have the direction cosines in axes $X_i$ defined by formulae (2.1), the transformed stiffness constant $c'_{3333}$ of crystallites with respect to $X_i$ is

$$\begin{aligned} c'_{3333} = (&3c_{1111} + 2c_{1133} + 3c_{3333} + 4c_{2323} - 4c_{1111}\cos 2\theta + \\ &4c_{3333}\cos 2\theta + c_{1111}\cos 4\theta - 2c_{1133}\cos 4\theta + c_{3333}\cos 4\theta - \\ &4c_{2323}\cos 4\theta + 2c_{1123}\sin(3\psi - 4\theta) - 4c_{1123}\sin(3\psi - 2\theta) + \\ &4c_{1123}\sin(3\psi + 2\theta) - 2c_{1123}\sin(3\psi + 4\theta))/8, \end{aligned} \tag{2.5}$$

and the remaining 20 transformed independent stiffness constants of the single crystal ($c'_{1112}$, $c'_{11222}$ etc.) referring to $X_i$ also usually involve all the elastic constants $c_{ijkl}$ with respect to $x_i$ axes and the three Euler angles specifying the relation between $x_i$ and $X_i$ axes, i.e. as a function of $c_{ijkl}, \theta, \phi, \psi$, which are too tedious to be presented here.

The averaged stiffness constant $\overline{c_{3333}}$ can be obtained by substituting $c'_{3333}$ into (2.3). All the other average stiffness constants are calculated using the same routine and the results are as follows (in abbreviated notations):

$$\begin{aligned}
&\overline{c_{11}}^v = \overline{c_{22}}^v = \overline{c_{33}}^v = \frac{8c_{11}+4c_{12}+3c_{33}+8c_{44}}{15}, \\
&\overline{c_{12}}^v = \overline{c_{13}}^v = \overline{c_{23}}^v = \frac{c_{11}+5c_{12}+8c_{13}+c_{33}-4c_{44}}{15}, \\
&\overline{c_{44}}^v = \overline{c_{55}}^v = \overline{c_{66}}^v = \frac{7c_{11}-5c_{12}-4c_{13}+2c_{33}+12c_{44}}{30}, \\
&\overline{c_{14}}^v = \overline{c_{24}}^v = \ldots\ldots = \overline{c_{56}}^v = 0.
\end{aligned} \tag{2.6}$$

where the supper subscript $v$ indicates the stiffness constants are obtained using Voigt's assumption.

It is found that 12 averaged stiffness constants are non-zero and only $\overline{c_{11}}$ and $\overline{c_{12}}$ are independent due to the existence of the relation

$$\overline{c_{44}}^v = \frac{(\overline{c_{11}}^v - \overline{c_{12}}^v)}{2}. \tag{2.7}$$

In fact, this is just the case for stiffness constant tensors of isotropic materials.

Similarly, the average compliance constants of trigonal crystals calculated using

equation (2.4) under Reuss' assumption are (in abbreviated notations):

$$\begin{aligned}
&\overline{s_{11}}^r = \overline{s_{22}}^r = \overline{s_{33}}^r = \frac{(8s_{11}+4s_{12}+3s_{33}+2s_{44})}{15},\\
&\overline{s_{12}}^r = \overline{s_{13}}^r = \overline{s_{23}}^r = \frac{(s_{11}+5s_{12}+8s_{13}+s_{33}-s_{44})}{15},\\
&\overline{s_{44}}^r = \overline{s_{55}}^r = \overline{s_{66}}^r = \frac{4(7s_{11}-5s_{12}-4s_{13}+2s_{33}+3s_{44})}{30},\\
&\overline{s_{14}}^r = \overline{s_{15}}^r = ..... = \overline{s_{24}}^r = 0.
\end{aligned} \tag{2.8}$$

where the relation

$$\overline{s_{44}}^r = 2(\overline{s_{11}}^r - \overline{s_{12}}^r). \tag{2.9}$$

exists and $r$ indicates the compliance constants obtained using Reuss' assumption. This is also the case for compliance constants of isotropic media. The convention for the relation between abbreviated notations and fourth rank tensors of compliance constants is different from those of stiffness constants and should be noted in calculation (also see reference [67] for the convention to the relation between $s_{ij}$ and $s_{ijkl}$).

The compliance constants obtained using formulae (2.8) can be expressed in matrix form. The inverse of the matrix gives the stiffness constant matrix. In this way, the stiffness constants (elements of the matrix) from Reuss' assumption are

$$\begin{aligned}
&\overline{c_{11}}^r = \overline{c_{22}}^r = \overline{c_{33}}^r = \frac{3(9s_{11}+5s_{12}+12s_{13}+4s_{33}+s_{44})}{((2s_{11}+2s_{12}+4s_{13}+s_{33})(7s_{11}-5s_{12}-4s_{13}+2s_{33}+3s_{44}))},\\
&\overline{c_{12}}^r = \overline{c_{13}}^r = \overline{c_{23}}^r = \frac{-3(s_{11}+5s_{12}+8s_{13}+s_{33}-s_{44})}{((2s_{11}+2s_{12}+4s_{13}+s_{33})(7s_{11}-5s_{12}-4s_{13}+2s_{33}+3s_{44}))},\\
&\overline{c_{44}}^r = \overline{c_{55}}^r = \overline{c_{66}}^r = \frac{15}{2(7s_{11}-5s_{12}-4s_{13}+2s_{33}+3s_{44})},\\
&\overline{c_{14}}^r = \overline{c_{15}}^r = .....\overline{c_{25}}^r = 0.
\end{aligned} \tag{2.10}$$

where we also have the relation

$$\overline{c_{44}}^r = \frac{(\overline{c_{11}}^r - \overline{c_{12}}^r)}{2}. \tag{2.11}$$

The compliance constants $\overline{s_{ij}}^{v}$ can be calculated from Voigt's assumption using the same method.

From the above results, it is proved that, for a random distribution of crystallites, the general elastic properties of polycrystalline aggregates of trigonal crystals are the same as the isotropic materials.

Due to forces between crystallites, the existence of residual stress and distorted crystallites, Voigt's assumption for an uniform strain and Reuss' assumption for an uniform stress throughout the aggregates are just an approximation to real polycrystalline aggregates. It is found that the calculated values of $\overline{c_{ij}}^{v}$ and $\overline{s_{ij}}^{v}$ are respectively different from $\overline{c_{ij}}^{r}$ and $\overline{s_{ij}}^{r}$. The average elastic constants of polycrystalline aggregates lie between the two values from Voigt's and Reuss' methods and can be chosen as the arithmetic average of the two values for a good approximation, i.e.

$$\begin{aligned} \overline{c_{ij}} &= \frac{(\overline{c_{ij}}^{v}+\overline{c_{ij}}^{r})}{2}; \\ \overline{s_{ij}} &= \frac{(\overline{s_{ij}}^{v}+\overline{s_{ij}}^{r})}{2}. \end{aligned} \tag{2.12}$$

There is no theoretical justification for this averaging, but it works well in practice.

### 2.1.4 General Symbolic Results for any Crystal Symmetry

For an even more general case, the calculations have been carried out using computer symbolic algebra for polycrystalline aggregates of the triclinic crystal system with

21 independent elastic constants. The results from Voigt's assumption are

$$\begin{aligned}
&\overline{c_{11}}^{v} = \overline{c_{22}}^{v} = \overline{c_{33}}^{v} = \frac{(3c_{11}+2c_{12}+3c_{22}+2c_{23}+2c_{13}+3c_{33}+4c_{44}+4c_{55}+4c_{66})}{15},\\
&\overline{c_{12}}^{v} = \overline{c_{13}}^{v} = \overline{c_{23}}^{v} = \frac{(c_{11}+4c_{12}+c_{22}+4c_{23}+4c_{13}+c_{33}-2c_{44}-2c_{55}-2c_{66})}{15},\\
&\overline{c_{44}}^{v} = \overline{c_{55}}^{v} = \overline{c_{66}}^{v} = \frac{(c_{11}-c_{12}+c_{22}-c_{23}-c_{13}+c_{33}+3c_{44}+3c_{55}+3c_{66})}{15},\\
&\overline{c_{14}}^{v} = \overline{c_{24}}^{v} = \ldots\ldots = \overline{c_{56}}^{v} = 0.
\end{aligned} \tag{2.13}$$

The average stiffness constants from Reuss' assumption are

$$\begin{aligned}
&\overline{c_{11}}^{r} = \overline{c_{22}}^{r} = \overline{c_{33}}^{r} =\\
&\frac{3(8s_{11}+12s_{12}+8s_{22}+12s_{23}+12s_{13}+8s_{33}+s_{44}+s_{55}+s_{66})}{((s_{11}+2s_{12}+s_{22}+2s_{23}+2s_{13}+s_{33})(4s_{11}-4s_{12}+4s_{22}-4s_{23}-4s_{13}+4s_{33}+3s_{44}+3s_{55}+3s_{66}))},\\
&\overline{c_{12}}^{r} = \overline{c_{13}}^{r} = \overline{c_{23}}^{r} =\\
&\frac{3(-2s_{11}-8s_{12}-2s_{22}-8s_{23}-8s_{13}-2s_{33}+s_{44}+s_{55}+s_{66})}{((s_{11}+2s_{12}+s_{22}+2s_{23}+2s_{13}+s_{33})(4s_{11}-4s_{12}+4s_{22}-4s_{23}-4s_{13}+4s_{33}+3s_{44}+3s_{55}+3s_{66}))},\\
&\overline{c_{44}}^{r} = \overline{c_{55}}^{r} = \overline{c_{66}}^{r} = \frac{15}{(4s_{11}-4s_{12}+4s_{22}-4s_{23}-4s_{13}+4s_{33}+3s_{44}+3s_{55}+3s_{66})},\\
&\overline{c_{14}}^{r} = \overline{c_{15}}^{r} = \ldots\ldots\overline{c_{25}}^{r} = 0.
\end{aligned} \tag{2.14}$$

where the relations (2.7) and (2.11) are still applicable.

Thus we conclude that the general elastic properties of polycrystalline aggregates with random distribution of anisotropic crystallites of any symmetry classes are the same as those of isotropic materials. It should also be noted that only nine of the 21 independent elastic constants appear in above results. In other words, the macroscopic elastic properties of polycrystalline aggregates are only contributed to by these nine elastic constant tensor elements and the elastic effects caused by other elastic constant tensor elements cancel out each other for a randomly distributed crystallites.

### 2.1.5 Discussion on the Results from Voigt's and Reuss's Assumption

It has been stated in reference [68] that the Voigt's stiffness constants are always greater than Reuss's stiffness constants, which we have proved is only true for the diagonal elastic constants $c_{11}$ and $c_{44}$ etc., but not for $c_{12}$ etc. On the contrary, $c_{12}$ or $s_{12}$ from Reuss's assumption are usually greater than those from Voigt's assumption.

The aggregates of cubic crystallites are chosen as an example to establish the above conclusions. The relation between stiffness and compliance constants for cubic crystals are

$$\begin{aligned} c_{11} &= \frac{s_{11}+s_{12}}{(s_{11}-s_{12})(s_{11}+2s_{12})} \\ c_{12} &= \frac{-s_{12}}{(s_{11}-s_{12})(s_{11}+2s_{12})} \\ c_{44} &= \frac{1}{s_{44}} \end{aligned} \tag{2.15}$$

which are substituted into the right hand side of (2.13) to obtain the Voigt's stiffness $c^v_{ij}(s_{ij})$ expressed by compliance constants $s_{ij}$. Calculating the differences of $c^v_{ij}(s_{ij})$ and $c^r_{ij}$, we have

$$\begin{aligned} c^v_{11}-c^r_{11} = c^v_{22}-c^r_{22} = c^v_{33}-c^r_{33} &= \frac{4(-2s_{11}+2s_{12}+s_{44})^2}{5(-s_{11}+s_{12})(-4s_{11}+4s_{12}-3s_{44})} \\ c^v_{44}-c^r_{44} = c^v_{55}-c^r_{55} = c^v_{66}-c^r_{66} &= \frac{3(-2s_{11}+2s_{12}+s_{44})^2}{5(-s_{11}+s_{12})(-4s_{11}+4s_{12}-3s_{44})} \\ c^v_{12}-c^r_{12} = c^v_{13}-c^r_{13} = c^v_{23}-c^r_{23} &= \frac{2(-2s_{11}+2s_{12}+s_{44})^2}{5(-s_{11}+s_{12})s_{44}(4s_{11}-4s_{12}+3s_{44})} \end{aligned} \tag{2.16}$$

where the numerators of three equations are positive. For normal cubic crystals, $s_{11} > s_{12}$, the denominators in the first two equations are also positive. Thus the stiffness constants of $c_{11}, c_{44}$ and their equalities obtained by Voigt's assumption are greater than those by Reuss' assumption. On the other hand, the denominator of third equation less than zero for $s_{11} > s_{12}$ and thus the Voigt's stiffness constant

of $c_{12}$ is less than Reuss' stiffness constant in this case. These results conform with the conclusion that the bulk and rigidity moduli obtained from Voigt's assumption exceed those obtained from Reuss's assumption in reference [69] and the true values lie between these two values, i.e.

$$K^r \leq K \leq K^v; \qquad G^r \leq G \leq G^v \tag{2.17}$$

where the $K = (c_{11} + 2c_{12})/3$, $G = (c_{11} - c_{12})/2$ are the bulk and shear moduli of polycrystalline aggregates. The same results have been found for the aggregates of other symmetry class crystals.

## 2.2 Polycrystalline Aggregates with Preferred Orientation Distribution

Polycrystalline materials, especially thin solid films, usually exist with different preferred orientations depending on the types of deposition techniques. If only one preferred orientation direction is assumed to be predominant in the aggregate, the elastic constants of this aggregate can be obtained through the rotation of elastic constants to the coordinates whose $z'$ axis is parallel to the orientation and the average taken over all directions on the $x', y'$ plane.

### 2.2.1 A Simple Method for Coordinate Transformation

If the $z'$ axis direction is chosen parallel to the orientation, the $x'$ and $y'$ can be chosen as any directions on the plane perpendicular to the $z'$ axis. For simplicity of

calculation, the $x'$ axis is chosen to lie in the $x$, $y$ plane and $y'$ is then determined so as to preserve a right handed coordinate system. If the direction cosines of preferred orientation $z'$ are $d_1$, $d_2$ and $d_3$ with respect to $x$, $y$,and $z$ axes, the direction cosines of $x'$ and $y'$ with $x$, $y$ and $z$ can be easily obtained. The coordinate transformation matrix describing the relations between two axes is as follows:

$$[a_{ij}] = \begin{bmatrix} -d_2\alpha^{-1} & d_1\alpha^{-1} & 0 \\ -d_1d_3\alpha^{-1} & -d_2d_3\alpha^{-1} & \alpha \\ d_1 & d_2 & d_3 \end{bmatrix}. \tag{2.18}$$

where $\alpha = \sqrt{d_1^2 + d_2^2}$ and $i, j = x, y, z$.

### 2.2.2 Averaging Method

#### Rotation of Elastic Constants in Abbreviated Subscript Notation

In order to carry out the transformation of elastic constants directly in abbreviated subscript notation without converting back to full subscripts to complicate calculations, the Bond method [45] is used here. The $6 \times 6$ stiffness and $6 \times 6$ compliance

transformation matrices for the above chosen axis system are

$$[M] =$$

$$\begin{bmatrix} d_2^2\alpha^{-2} & d_1^2\alpha^{-2} & 0 & 0 & 0 & -2d_1d_2\alpha^{-2} \\ d_1^2d_3^2\alpha^{-2} & d_2^2d_3^2\alpha^{-2} & \alpha^2 & -2d_2d_3 & -2d_1d_3 & 2d_1d_2d_3^2\alpha^{-2} \\ d_1^2 & d_2^2 & d_3^2 & 2d_2d_3 & 2d_1d_3 & 2d_1d_2 \\ -d_1^2d_3\alpha^{-1} & -d_2^2d_3\alpha^{-1} & d_3\alpha & d_2(\alpha - d_3^2\alpha^{-1}) & d_1(\alpha - d_3^2\alpha^{-1}) & -2d_1d_2d_3\alpha^{-1} \\ -d_1d_2\alpha^{-1} & d_1d_2\alpha^{-1} & 0 & d_1d_3\alpha^{-1} & -d_2d_3\alpha^{-1} & (d_1^2 - d_2^2)\alpha^{-1} \\ d_1d_2d_3\alpha^{-2} & -d_1d_2d_3\alpha^{-2} & 0 & d_1 & -d_2 & d_3(d_2^2 - d_1^2)\alpha^{-2} \end{bmatrix}, \tag{2.19}$$

$$[N] =$$

$$\begin{bmatrix} d_2^2\alpha^{-2} & d_1^2\alpha^{-2} & 0 & -d_1^2d_3\alpha^{-1} & -d_2^2d_3\alpha^{-1} & d_3\alpha \\ d_1^2d_3^2\alpha^{-2} & d_2^2d_3^2\alpha^{-2} & \alpha^2 & -d_1d_2\alpha^{-1} & d_1d_2\alpha^{-1} & 0 \\ d_1^2 & d_2^2 & d_3^2 & d_1d_2d_3\alpha^{-2} & -d_1d_2d_3\alpha^{-2} & 0 \\ 0 & 0 & -2d_1d_2\alpha^{-2} & d_2(\alpha - d_3^2\alpha^{-1}) & d_1(\alpha - d_3^2\alpha^{-1}) & -2d_1d_2d_3\alpha^{-1} \\ -2d_2d_3 & -2d_1d_3 & 2d_1d_2d_3^2\alpha^{-2} & d_1d_3\alpha^{-1} & -d_2d_3\alpha^{-1} & (d_1^2 - d_2^2)\alpha^{-1} \\ 2d_2d_3 & 2d_1d_3 & 2d_1d_2 & d_1 & -d_2 & d_3(d_2^2 - d_1^2)\alpha^{-2} \end{bmatrix}. \tag{2.20}$$

The $6 \times 6$ stiffness and compliance constant matrices $c'$ and $s'$ with respect to $x'$, $y'$ and $z'$ axes are

$$[c'] = [M][c][\widetilde{M}]; \tag{2.21}$$

$$[s'] = [N][s][\widetilde{N}]. \tag{2.22}$$

where $[c]$ and $[s]$ are the stiffness and compliance constant matrices of crystallites with respect to $x$, $y$, $z$ axes and $[\widetilde{M}]$ and $[\widetilde{N}]$ are the transposes of the matrices $[M]$

and $[N]$.

Following the same procedure, $[c']$ and $[s']$ are transformed from $x'$, $y'$, $z'$ axes to cylindrical coordinates $(\phi, z')$ using the coordinate transformation matrix

$$[a_c] = \begin{bmatrix} \cos\phi & \sin\phi & 0 \\ -\sin\phi & \cos\phi & 0 \\ 0 & 0 & 1 \end{bmatrix}. \tag{2.23}$$

The corresponding stiffness and compliance transformation matrices are

$$[M_c] = \begin{bmatrix} \cos^2\phi & \sin^2\phi & 0 & 0 & 0 & \sin 2\phi \\ \sin^2\phi & \cos^2\phi & 0 & 0 & 0 & -\sin 2\phi \\ 0 & 0 & 1 & 0 & 0 & 0 \\ 0 & 0 & 0 & \cos\phi & -\sin\phi & 0 \\ 0 & 0 & 0 & \sin\phi & \cos\phi & 0 \\ \cos^2\phi\sin^2\phi & \cos^2\phi\sin^2\phi & 0 & 0 & 0 & \cos^2\phi - \sin^2\phi \end{bmatrix}, \tag{2.24}$$

$$[N_c] = \begin{bmatrix} \cos^2\phi & \sin^2\phi & 0 & 0 & 0 & 0 \\ \sin^2\phi & \cos^2\phi & 0 & 0 & 0 & 0 \\ 0 & 0 & 1 & \cos^2\phi\sin^2\phi & \cos^2\phi\sin^2\phi & 0 \\ 0 & 0 & \sin 2\phi & \cos\phi & -\sin\phi & 0 \\ 0 & 0 & -\sin 2\phi & \sin\phi & \cos\phi & 0 \\ 0 & 0 & 0 & 0 & 0 & \cos^2\phi - \sin^2\phi \end{bmatrix}. \tag{2.25}$$

The stiffness and compliance constant matrices $[c'']$ and $[s'']$ with respect to cylindrical

axes are

$$[c''] = [M_c][c'][\widetilde{M_c}]; \tag{2.26}$$

$$[s'] = [N_c][s'][\widetilde{N_c}]. \tag{2.27}$$

## Results and Discussion

Thus the stiffness and compliance constants of the aggregates with preferred orientation are averaged in all directions on the plane perpendicular to $z'$ axis as follows

$$\overline{c_{ij}} = \frac{\int_0^{2\pi} c''_{ij} d\varphi}{2\pi} \tag{2.28}$$

$$\overline{s_{ij}} = \frac{\int_0^{2\pi} s''_{ij} d\varphi}{2\pi} \tag{2.29}$$

where $c''_{ij}$ and $s''_{ij}$ are the elements of matrix $[c'']$ and $[s'']$, which are functions of angle $c'_{ij}$ and $\phi$.

The averaged elastic constant matrix (both stiffness and compliance) has five non-zero independent constants, which is similar to that of transversely isotropic materials. In other words, the surface elastic properties of thin solid films with preferred orientation are independent of surface propagation directions and no angular dispersion ($v$ vs. $\phi$) relation exists on the surface.

It is found that the stiffness constants $\overline{c_{ij}}^s$ obtained by inverse of average compliance constant matrix $[\overline{s_{ij}}]$ from equation (2.29) are different from those $\overline{c_{ij}}^c$ calculated from equation (2.28). The differences between the $\overline{c_{ij}}^v$ and $\overline{c_{ij}}^r$ described for the random distribution in the previous section are still applicable here for $\overline{c_{ij}}^c$ and $\overline{c_{ij}}^s$. Thus the stiffness or compliance constants for the aggregates with orientations are chosen as the arithmetic average from the two methods.

| Polycrstalline Hard Materials | $Al_2O_3$ | $SiC$ | $TiC$ | $TiN$ | $HSS$ |
|---|---|---|---|---|---|
| Melting Temperature($^\circ C$) | 2047 | 2760 | 3067 | 2950 | 1400 |
| Vickers' Hardness($kgfmm^{-2}$) | 2100 | 2600 | 2800 | 2100 | 900 |
| Mass Density($gcm^{-3}$) | 3.98 | 3.22 | 4.90 | 5.40 | 7.80 |
| Young's Modulus($GPa$) | 400 | 480 | 460 | 590 | 250 |
| Thermal Expan. Coef.($10^{-6}K^{-1}$) | 6.5 | 5.3 | 8.3 | 9.3 | 14 |
| Thermal Conductivity($Wm^{-1}K^{-1}$) | 25 | 84 | 34 | 30 | 30 |

Table 2.1: Mechanical properties of polycrystalline hard materials.

## 2.3 Elastic Constants of Polycrystalline Hard Films

The term hard films usually refers to transition metal carbides and nitrides such as $TiC$, $TiN$ and $TiAlN$ etc. These films are prepared by both chemical and physical vapor deposition techniques, and are at present widely used as hard protective coating on various tool steels to enhance their life by many hundred per cent. Because of their commercial success in the industrial arena, much attention has been given to exploring new hard film materials. The mechanical properties of such films and $HSS$ as listed in table 2.1 (from ref. [1]).

In this section, the elastic constants of these polycrystalline films and the $HSS$ (high speed steel) substrate are calculated for both randomly and preferred orientation distributed crystallites using the theories discussed in previous sections. The results for $TiN$ films and the $HSS$ substrate will be used in latter chapters to discuss their surface wave propagation behavior.

| Stiffness $c_{ij}$ ($10^9$ $newton/m^2$) and Compliance $s_{ij}$ ($10^{-12}$ $m^2/newton$) Constants | | | | | | | | | | | | |
|---|---|---|---|---|---|---|---|---|---|---|---|---|
| materials | $c_{11}$ | $c_{33}$ | $c_{44}$ | $c_{12}$ | $c_{13}$ | $c_{14}$ | $s_{11}$ | $s_{33}$ | $s_{44}$ | $s_{12}$ | $s_{13}$ | $s_{14}$ |
| $Al_2O_3$ | 494 | 496 | 145 | 158 | 114 | -23 | 2.38 | 2.20 | 7.05 | -0.70 | -0.38 | 0.49 |
| SiC | 352 | | 233 | 140 | | | 3.67 | | 4.29 | -1.04 | | |
| TiC | 513 | | 178 | 106 | | | 2.10 | | 5.61 | -0.359 | | |
| TiN | 498 | | 168 | 106 | | | 2.17 | | 5.95 | -0.380 | | |
| TiN* | 625 | | 163 | 165 | | | 1.79 | | 6.13 | -0.375 | | |
| $\alpha - Fe$ | 237 | | 116 | 141 | | | 7.59 | | 8.62 | -2.82 | | |

Table 2.2: Stiffness and compliance constants of single crystals of hard materials.

### 2.3.1 Elastic Constants of Single Crystals

The stiffness constants of single crystals of these materials are given in table 2.2 (from references [7], [11], [45], [70]). Here, $Al_2O_3$ has the trigonal $\bar{3}m$ symmetry and the remaining belong to the cubic classes. The different elastic constants of $TiN$ single crystal from two experimental methods are indicated as $TiN$ and $TiN^*$. The elastic constants of $TiN^*$ have been measured by Kim et al. [11] using the line focus acoustic microscopy technique. Rickerby [71] first reported the elastic constants of $TiN$ which are calculated from the slope of the acoustic branches of phonon dispersion curves measured by Kress [72] et al. using inelastic neutron scattering. Perry [7] used the latter elastic constants in his study on residual stress in $TiN$ films.

| Stiffenss Constants, elastic moduli($10^{10}$ $newton/m^2$) and Poisson's ratio | | | | | | | | | |
|---|---|---|---|---|---|---|---|---|---|
| material | $\overline{c_{11}}^v$ | $\overline{c_{12}}^v$ | $\overline{c_{44}}^v$ | $\overline{c_{11}}^r$ | $\overline{c_{12}}^r$ | $\overline{c_{44}}^r$ | E(ave.) | G(ave.) | $\sigma$ |
| $Al_2O_3$ | 47.0 | 14.0 | 16.4 | 45.9 | 14.1 | 15.8 | 39.9 | 16.4 | 0.216 |
| SiC | 45.3 | 8.92 | 18.2 | 42.0 | 10.5 | 15.7 | 40.1 | 17.4 | 0.198 |
| TiC | 49.2 | 11.6 | 18.8 | 49.1 | 11.6 | 18.7 | 44.7 | 18.8 | 0.188 |
| TiN | 47.5 | 11.7 | 17.9 | 47.4 | 11.8 | 17.8 | 42.8 | 17.8 | 0.178 |
| TiN* | 57.1 | 19.1 | 18.9 | 56.4 | 19.5 | 18.4 | 46.9 | 18.8 | 0.245 |
| $\alpha - Fe$ | 29.1 | 11.3 | 8.86 | 27.1 | 12.3 | 7.40 | 21.1 | 8.38 | 0.314 |

Table 2.3: The averaged stiffness constants $\overline{c_{ij}}^v$, $\overline{c_{ij}}^r$, elastic moduli E and G and Poisson's ratio $\sigma$ of polycrystalline aggregates with random distributions of crystallites. Here $K = (c_{11} + 2c_{12})/3$, $G = (c_{11} - c_{12})/2$ and $\sigma = \frac{c_{12}}{c_{11}+c_{12}}$.

The compliance constants of these materials are calculated using the formulae

$$s_{11} = \frac{c_{14}^2 c_{33} + c_{13}^2 c_{44} - c_{11} c_{33} c_{44}}{(-2c_{13}^2 + c_{11} c_{33} + c_{12} c_{33})(-2c_{14}^2 + c_{11} c_{44} + c_{12} c_{44})}, \quad s_{33} = \frac{c_{11} + c_{12}}{-2c_{13}^2 + c_{11} c_{33} + c_{12} c_{33}},$$

$$s_{44} = \frac{c_{11} - c_{12}}{-2c_{14}^2 + c_{11} c_{44} - c_{12} c_{44}}, \quad s_{12} = \frac{c_{14}^2 c_{33} - c_{13}^2 c_{44} + c_{11} c_{33} c_{44}}{(-2c_{13}^2 + c_{11} c_{33} + c_{12} c_{33})(-2c_{14}^2 + c_{11} c_{44} + c_{12} c_{44})}, \tag{2.30}$$

$$s_{13} = \frac{c_{13}}{2c_{13}^2 - c_{11} c_{33} - c_{12} c_{33}}, \qquad s_{14} = \frac{c_{14}}{2c_{14}^2 - c_{11} c_{44} - c_{12} c_{44}}$$

for trigonal $Al_2O_3$ and the equation (2.15) (just exchanging the symbolic $c$ and $s$ for $s_{ij}$ in terms of $c_{ij}$) for cubic crystals.

### 2.3.2 Averaged Elastic Constants

The stiffness constants and elastic moduli of the corresponding polycrystalline hard films obtained using both Voigt's and Reuss' assumptions and are shown in table 2.3, where the E is Young modulus, G shear modulus and $\sigma$ Poisson's ratio calculated

| Stiffness Constant $c_{ij}$ $(10^{10}\ N/m^2)$ | | | | | | | | | | |
|---|---|---|---|---|---|---|---|---|---|---|
| material | $\overline{c_{11}}^c$ | $\overline{c_{33}}^c$ | $\overline{c_{44}}^c$ | $\overline{c_{12}}^c$ | $\overline{c_{13}}^c$ | $\overline{c_{11}}^s$ | $\overline{c_{33}}^s$ | $\overline{c_{44}}^s$ | $\overline{c_{12}}^s$ | $\overline{c_{13}}^s$ |
| TiN | 47.3 | 46.9 | 18.2 | 11.6 | 11.9 | 47.2 | 46.8 | 18.1 | 11.7 | 12.0 |
| TiN* | 56.6 | 55.7 | 19.6 | 19.0 | 19.0 | 55.9 | 55.2 | 19.0 | 19.3 | 20.1 |

Table 2.4: The averaged stiffness constants of TiN films with [111] preferred orientation.

from the arithmetic average of Voigt's and Reuss' stiffness constants. It is seen in the table that $\overline{c_{11}}^v > \overline{c_{11}}^r$, $\overline{c_{44}}^v > \overline{c_{44}}^r$ and $\overline{c_{12}}^v < \overline{c_{12}}^r$.

Our samples of $TiN$ films on tool steels were prepared using the magnetron sputtering and hollow cathode discharge plating techniques, and these films have a preferred orientation. As discussed in later section 7.2, the [111] direction is found to be the most strongly preferred orientation of $TiN$ films.

In order to calculate the surface velocities of these films in the latter chapters and compare with those surface velocities calculated using the data (for random distribution) in table 2.3, the stiffness constants of these films are calculated with their preferred orientation being taken into account. The results obtained using the method discussed in section 2.2 are shown in table 2.4.

In the calculation, all crystallites of the films are assumed to have the same orientation. The $\overline{c_{ij}}^c$ denote the stiffness constants defined by formula (2.28), and $\overline{c_{ij}}^s$ are the stiffness constants, i.e. the elements of inverse of matrix $[\overline{s_{ij}}]$ which is calculated from formula (2.29). The five non-zero independent stiffness constants indicate the films have transversely isotropic elastic properties.

# Chapter 3

# Wave Propagation Characteristics and Extracting the Elastic Constants of Anisotropic Solids from Velocity Data

In the study of elastic wave propagation in anisotropic solids, the slowness surface is a most convenient and effective tool. It is the surface representing the inverse of the phase velocity as a function of propagation direction, and depends on the elastic constants of the medium. The computer visualization of slowness surfaces is used to display wave propagation behavior in anisotropic solids, and can in turn be used to seek group velocity (energy flow) directions and special propagation directions such as those of pure modes and conical points. The coded computer programs can

be applied to plot three-dimensional slowness surfaces and two-dimensional slowness curves on any crystal planes. Single crystals of cubic $GaAs$ and $TiN$ are taken to be the examples to illustrate these characteristics as shown in section 3.1.2. The slowness surfaces of polycrystalline $TiN$ with a [111] preferred orientation have also been obtained using the averaged elastic constants (refer to table 2.4). It is shown that the elastic properties of polycrystalline $TiN$ films with a [111] preferred orientation are very close to those of isotropic solids. This conclusion will be used in a later chapter to simplify the calculation model for surface wave propagation in a very thin $TiN$ film on tool steel.

The elastic properties of a material are defined by its elastic constant tensor which is determined through its relation to the phase velocities in different propagation directions. Phase velocities in a given direction are usually measured by various experimental techniques such as pulsed ultrasonics, neutron scattering and Brillouin scattering etc. [62]. The relation between the velocities and the elastic constants of anisotropic solids is governed by the Christoffel equation. The relationship is simple in the directions of crystal axes of high symmetry crystals. In these directions, sound waves may be purely longitudinal or transverse and are called pure modes. A single elastic constant, usually a diagonal term of the matrix of elastic constants, can sometimes be obtained from the velocity measurement in these pure mode directions. It is proved that only for cubic crystals can all elastic constants be obtained from the measurements in such pure mode directions. For general cases, other remaining nondiagonal terms of elastic constant matrix have to be determined from the measurements in a non-pure mode direction.

From the experimental point of view, sometimes it is not easy to have a crystal faceted and aligned in a specific way, especially when crystalline phase transition processes are studied under the variation of temperature [63]. A direction according to experimental convenience is selected to measure the phase velocity whose relation with elastic constants (as many as 21 for triclinic class) can be very complicated. In these directions, numerical calculation is normally needed to solve the Christoffel equation. The inversion of experimental velocity data into elastic constants is usually concerned with an overdetermined system of equations, i.e. the number of measured velocities exceeds the number of the elastic constants to be determined. Several optimization procedures for elastic constants have been proposed, including the use of invariants of the Christoffel tensor [63], the minimum of the secular equation of the Christoffel polynomial with the measured velocities[64], a perturbation series expansion in an intensively rotated axes system [65], and an iterative inversion technique using updated polarization [66]. All these methods can be applied for wave propagation in arbitrary directions for any symmetry classes of crystals.

In this chapter, a set of velocity data with arbitrary propagation directions are synthesized from theoretically calculated values with 1% error to simulate experimental results for the single crystal of cubic $GaAs$. Computer programs have been coded to carry out the numerical computations for each of the optimization methods and a very subtle procedure has been used to approach "better values" of elastic constants to minimize iteration times in the adopted iterative techniques. Even starting with a very rough estimate of initial elastic constants, the final converged results are fairly close to those expected from some of the methods. A comparison of convergencies of

different algorithms reveal that some methods are robust and can be widely used in general cases whereas certain methods have limitations in their use.

## 3.1 Wave Propagation Characteristics Described Using the Slowness Surface

### 3.1.1 Bulk Mode Elastic Wave Propagation

The behavior of elastic waves propagating in an infinite perfectly elastic, homogeneous anisotropic medium is governed by the equation (in the Einstein summation notation)

$$\Gamma_{jk}u_k = \rho v^2 u_j, \tag{3.1}$$

which is called the Christoffel equation, where the matrix $\Gamma_{jk} = l_i l_l c_{ijkl}$ is called the Christoffel matrix whose elements depend on the wave propagation direction described by direction cosines $l_i$ and the stiffness constants $c_{ijkl}$ of the medium. The $u_j$ are the displacement components measured with respect to Cartesian axes $x_i$, and $\rho$ is the density of the material. In order to find the non-trivial solution for the $u_j$, the determinant of the coefficients is set to zero, i.e.

$$|\Gamma_{jk} - \delta_{jk}\rho v^2| = 0, \tag{3.2}$$

where $v$ is the phase velocity of wave propagating in the direction defined by $l_i$ and can be numerically solved to yield three roots for a given stiffness constants and any assumed direction. Equation (3.2) can be factored in some specific directions

(usually the principal directions) and, in this case, algebraic results may be obtained that reveal the relation between phase velocity and elastic constants.

### 3.1.2 Computer Visualization of Three-Dimensional Slowness Surfaces

Equation (3.2) can be reorganized as

$$|s^2\Gamma_{jk} - \delta_{jk}\rho| = 0, \tag{3.3}$$

where $s$, the slowness, is defined as $1/v$, which is a function of wave propagation direction $l_i(\theta, \phi)$ governed by this equation , where $l_1 = \sin\theta\cos\phi$, $l_2 = \sin\theta\sin\phi$ and $l_3 = \cos\theta$ in spherical coordinates. Slowness surfaces of three bulk waves for any crystal classes are obtained by plotting $s$ against $\theta$ and $\phi$ using the coded computer programs.

Figure 3.1 is the eighth ($0 < \theta < 90°$, $0 < \phi < 90°$) of the slowness surface of cubic $GaAs$ of the $\bar{4}3m$ symmetry classes. The three sheets of slowness from the inner to outer respectively correspond to the longitudinal ($L$), fast transverse ($T1$) and slow transverse ($T2$) waves. The units of three axes are $s/m$.

This three-dimensional figure is very useful in the study of the topological features of the slowness surface, which is of great importance for investigations of surface and bulk wave propagation in anisotropic solids. The unit normal (direction of group velocity) to the slowness surface indicate the direction of energy flow of bulk waves. For isotropic materials, slowness surfaces are two spheres (the two transverse waves are degenerate); the group velocity direction is collinear with the propagation direction.

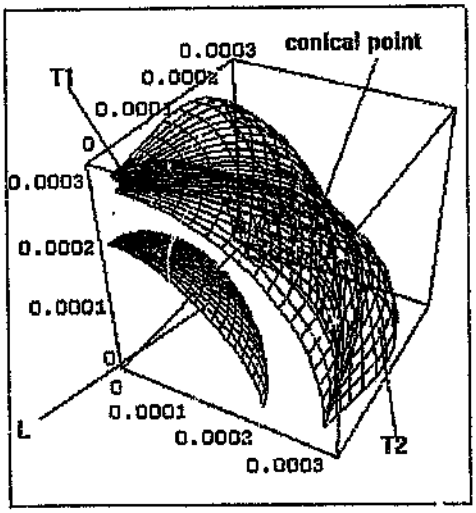


Figure 3.1: Slowness surface of cubic $GaAs$ in first octant of the coordinates measured in units of $s/m$. The stiffness constants used for calculation are $c_{11} = 118.8$ $GPa$, $c_{12} = 53.8\,GPa$ and $c_{44} = 59.4\,GPa$.

A conical point is defined as a singular point of the slowness surface where two or three slowness sheets intersect and are asymptotic to the complementary halves of an elliptical cone.

It is seen in figure (3.1) that there is a conical point in [111] propagation direction for cubic $GaAs$ ,which is described by $\theta = 54.73°$ and $\phi = 45.0°$ in spherical coordinates. The magnitude of three slownesses in this direction are $1.852 \times 10^{-4}(s/m)$, $3.577 \times 10^{-4}(s/m)$, $3.577 \times 10^{-4}(s/m)$; the equivalent two values indicate the position of the conical point. The three slowness surfaces of cubic $TiN$ and polycrystalline $TiN$ films with [111] orientation (its elastic properties are identical to those of transversely isotropic crystals, refer to table 2.2) are also presented here to reveal their topological features.

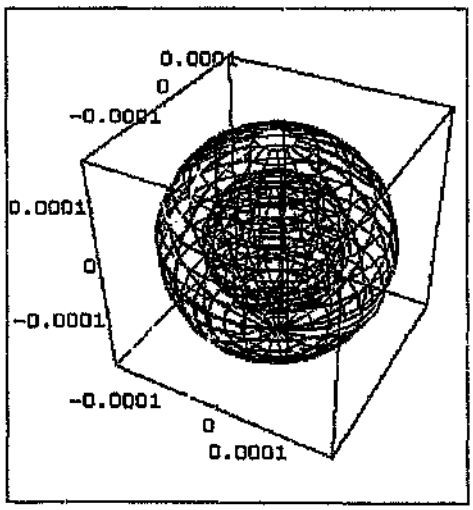


Figure 3.2: Slowness surfaces of a $TiN$ polycrystal with [111] orientation.

In order to calculate the slowness surfaces of polycrystalline $TiN$ with [111] ori-

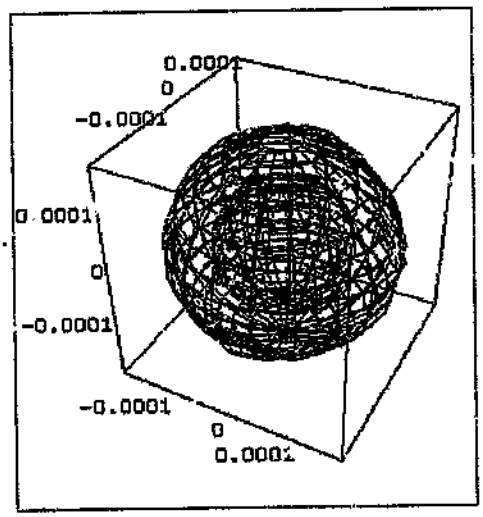


Figure 3.3: Slowness surfaces of cubic $TiN$ with elastic constants $c_{11} = 498\ GPa$, $c_{12} = 106\ GPa$ and $c_{44} = 168\ GPa$.

entation, we use the averaged stiffness constants in table 2.4. The surfaces shown in figure (3.2) are symmetrical about the $z$ axis, which is obviously an important property of a transversely isotropic material. Moreover, the slowness surfaces obtained here are close to being spherical which is the form of slowness sur of isotropic media. This implies that a $TiN$ polycrystal with [111] orientation can be approximately treated as an isotropic medium in the complicated calculation to be presented in chapter 5.

Figure 3.3 indicates that the slowness surfaces of cubic $TiN$ are close to those of isotropic media . In fact, the anisotropy factor of the cubic $TiN$ is

$$\eta = \frac{2c_{44}}{c_{11} - c_{12}} \approx 0.86, \tag{3.4}$$

so the surface waves of this material are not far from Rayleigh waves of an isotropic material. The phase velocities are almost independent of angle. The dispersion relations of cubic *TiN* will be discussed in the next chapter.

### 3.1.3 Slowness Sections on Various Crystal Planes

Slowness sections are used to study the details of wave propagation behavior in any direction on an arbitrary plane in an anisotropic medium. In the study of surface wave propagation, the outer sheet of slowness sections is also used to define the types of first transonic states, which is useful in deciding whether the Rayleigh velocity exists in a half space of an anisotropic medium [61]. Based on the result that energy velocity (identical to group velocity in a lossless medium) directions are always normal to the slowness surface, the pure mode propagation direction is the group velocity direction passing the selected origin of coordinates.

In order to plot the slowness curves on any crystal plane, the elastic constant tensor should be first rotated to the new coordinate system where the $x'$ axis is normal to the chosen plane. Three slowness magnitudes ($s$) can be solved using equation (3.3) with transformed elastic tensors under new coordinate system for any directions defined by a function of $\phi$ on the specific plane. Slowness curves on the plane are obtained by plotting $s$ against $\phi$ in polar coordinates. A computer program has been coded to plot three slowness curves on an arbitrarily selected plane of any symmetry crystal class.

The slowness sections of cubic *TiN* on various crystal planes are presented in

figures (3.4, 3.5, 3.6).

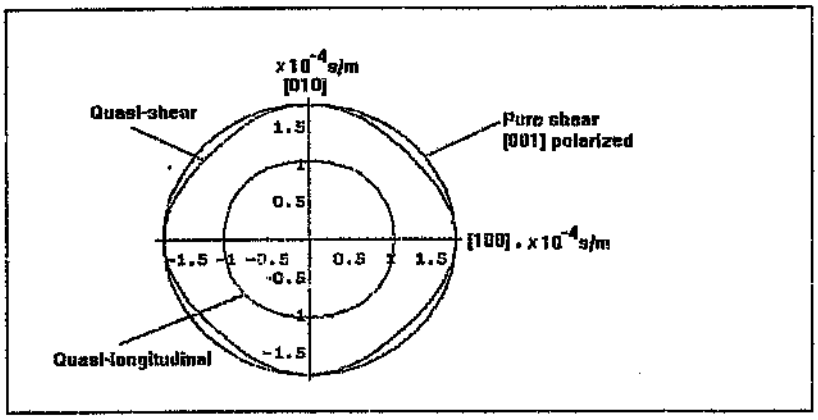


Figure 3.4: Slowness curves on the [001] plane of cubic $TiN$.

Since both [001] and [110] crystal planes are mirror planes in cubic symmetry, there is a pure shear mode polarized normal to the plane of propagation as seen in figures (3.4, 3.5). However, the [111] plane is not a mirror symmetry plane in cubic crystals. There is however 6-fold symmetry for the slowness curve on this plane as seen in figure (3.6).

The slowness section curves of $TiN$ polycrystalline films with preferred orientation [111] are shown in figure (3.7). The five independent stiffness constants (see table 2.4) allow the slowness of $TiN$ films to be treated in the same way as that for a hexagonal system. Both slowness curves on the [001] plane perpendicular to the $z$ axis and on the meridian plane are approximately the same. Two shear waves with displacement polarization parallel and perpendicular to $z$ axes respectively are approximately degenerate on the two planes. This shows that the wave propagation

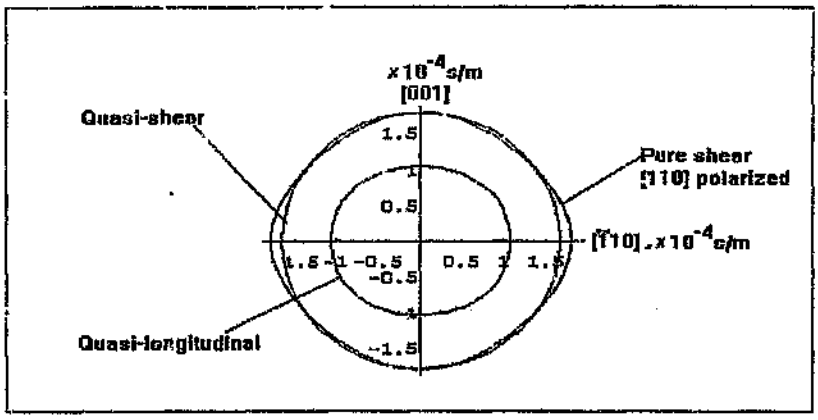


Figure 3.5: Slowness curves on the [110] plane of cubic $TiN$.

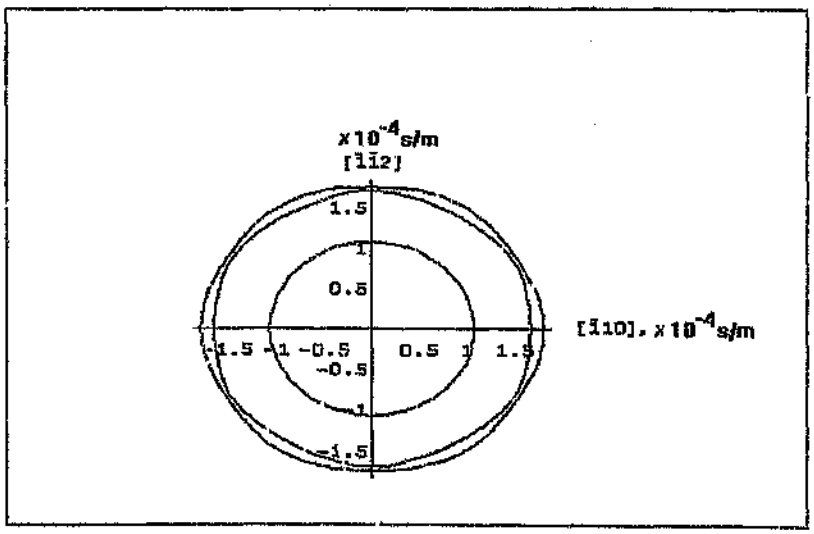


Figure 3.6: Slowness curves on the [111] plane of cubic $TiN$.

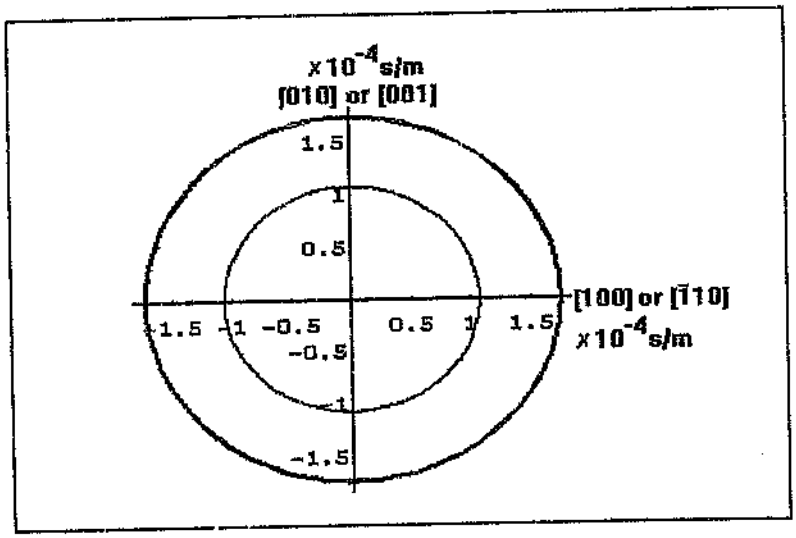


Figure 3.7: Slowness curves on the [001] or meridian plane of TiN films with [111] preferred orientation.

on the surface ([111] plane) of *TiN* films almost has the same properties as those for isotropic media, i.e. the dispersion relation is independent of the propagation directions and the two shear waves are degenerate. Thus it is reasonable to simplify the model to the isotropic case (also see figure 3.2) in next chapter when we calculate the dispersion relation of *TiN/HSS* combinations, i.e. the dependence of surface wave velocity in the films on the product of wave vector component parallel to the surface of films and film thickness.

| No. | $\theta(rad)$ | $\phi(rad)$ | vL(m/s) | vT1(m/s) | vT2(m/s) |
|---|---|---|---|---|---|
| 1 | 7.75695 | 16.7618 | 4784.89 | 3341.9 | 3272.8 |
| 2 | 33.1938 | 32.8542 | 5227.76 | 3161.1 | 2728.55 |
| 3 | 33.1938 | 40.1142 | 5236.68 | 3120.84 | 2759.93 |
| 4 | 50.4026 | 16.7618 | 5281.09 | 3229.67 | 2538.35 |
| 5 | 50.4026 | 32.8542 | 5366.55 | 2992.79 | 2647.71 |
| 6 | 61.1056 | 59.1754 | 5336.15 | 3000.67 | 2700.68 |
| 7 | 61.1056 | 70.908 | 5237.4 | 3169.82 | 2700.26 |
| 8 | 71.2393 | 32.8542 | 5278.18 | 3128.48 | 2669.32 |
| 9 | 81.4965 | 74.1576 | 4958.01 | 3279.62 | 3051.82 |
| 10 | 88.0649 | 7.59719 | 4786.11 | 3342.52 | 3270.85 |

Table 3.1: Synthesized phase velocity data in arbitrary directions.

## 3.2 Synthesized Experimental Velocity Data in Randomly Chosen Directions

The wave propagation direction $l_i$ is described in terms of spherical coordinates $\theta$ and $\phi$ by $l_1 = \sin\theta\cos\phi$, $l_2 = \sin\theta\sin\phi$ and $l_3 = \cos\theta$. Calculated velocity data in an arbitrary direction can be obtained by randomly choosing $\theta$ and $\phi$ and using equation (3.2). In order to simulate measured velocities (in view of the less than 1% uncertainties in Brillouin frequency shift measurements, a $\pm 1\%$ random error must be taken into account to modify the calculated velocities.

A $GaAs$ cubic crystal is chosen as an example and its stiffness constants are

respectively $c_{11} = 118.8\ GPa$, $c_{12} = 53.8\,GPa$ and $c_{44} = 59.4\,GPa$. Its density is $5307 kg/m^3$. The data in table 3.1 is obtained using the coded computer programs which randomly choose the propagation directions. This data will be used as the measured phase velocity from experiment to extract elastic constants of $GaAs$ by four methods to be discussed in section 3.3.

## 3.3 Methods of Recovery of Elastic Constants

### 3.3.1 Least Squares Fit

The first optimization method (refer to Every [63]) is to minimize the expression:

$$\chi^2 = \sum_{i}^{n}\sum_{j}^{3}(v_{ij}^{ex} - v_{ij}^{th})^2, \tag{3.5}$$

where $v^{ex}$ and $v^{th}$ are velocities respectively from experiment (from table 3.1) and theoretical calculations for the same specific propagation direction defined by $(\theta, \phi)$. The subscripts ( $i$, $j$) indicate that summation is made over $n$ (here $n = 10$) arbitrarily measured directions and in every direction over three velocities, i.e. 1 quasi-longitudinal and 2 quasi-transverse. $v_{ij}^{th}$ is obtained numerically using equation (3.2) from the known measured crystallographic directions, (see the first two columns in table 3.1) and estimated elastic constants. It varies with the upgraded elastic constants in each iteration. The computer program is coded to do the optimization procedure. The "better values" of elastic constants are updated from the previous "better values" only if the current $\chi^2$ is less than previous one.

The initial estimation of stiffness of $GaAs$ are $c_{11} = 170\,GPa$, $c_{12} = 20\,GPa$ and

| No. | $c_{11}(GPa)$ | $c_{12}(GPa)$ | $c_{44}(GPa)$ | $\chi^2$ |
|---|---|---|---|---|
| 1 | 161.3 | 26.43 | 69.96 | $2.817\,10^6$ |
| 2 | 149.4 | 35.09 | 53.46 | $7.465\,10^5$ |
| 3 | 128.0 | 52.16 | 58.94 | $7.231\,10^4$ |
| 4 | 120.2 | 55.09 | 57.74 | $7.399\,10^3$ |
| 5 | 117.7 | 53.16 | 59.64 | $7.377\,10^2$ |
| 6 | 119.2 | 54.53 | 59.17 | 349.2 |
| 7 | 119.1 | 53.21 | 59.18 | 307.3 |
| 8 | 118.9 | 53.54 | 59.15 | 195.5 |
| 9 | 118.8 | 53.91 | 59.32 | 24.44 |

Table 3.2: Stiffness constants of $GaAs$ from a least squares fit.

$c_{44} = 70\,GPa$. The $\chi^2$ for every set of updated stiffness constants are presented in table 3.2.

From the table 3.2, the best fits obtained are $c_{11} = 118.8\,GPa$, $c_{12} = 53.9\,GPa$ and $c_{44} = 59.3\,GPa$, which fairly close to the stiffness constants $c_{11} = 118.3\,GPa$, $c_{12} = 53.8\,GPa$ and $c_{44} = 59.4\,GPa$, which are used to produce the synthesized velocity data ($\pm 1\%$ error). The same calculation has been done on the trigonal (32) low symmetry crystal class. It is found that $\chi^2$ decreases rapidly and the $c_{ijkl}$ converge to a set of values very close to what was expected even though a very rough estimation of initial elastic constants is made.

| No. | $c_{11}(GPa)$ | $c_{12}(GPa)$ | $c_{44}(GPa)$ | $\sum(\phi_i)^2(\times 10^{59} kg \cdot m/s^2)$ |
|---|---|---|---|---|
| 1 | 160.9 | 23.03 | 61.18 | $3.622\,10^5$ |
| 2 | 141.0 | 22.99 | 64.66 | $9.848\,10^4$ |
| 3 | 124.2 | 399.62 | 64.03 | $8.503\,10^3$ |
| 4 | 120.1 | 50.61 | 60.12 | $4.777\,10^2$ |
| 5 | 119.2 | 54.86 | 58.76 | $5.832\,10^1$ |
| 6 | 118.6 | 53.42 | 59.70 | 7.760 |
| 7 | 118.7 | 53.39 | 59.61 | 4.232 |

Table 3.3: Stiffness constants of $GaAs$ from minimising $\sum(\phi_i)^2$.

### 3.3.2 Minimum of $\Sigma(\phi_i)^2$

The second method (refer to Castagnede [64]) uses the formulae

$$\chi^2 = \sum_i^{3n} \phi_i^2 = \sum_i^{3n} (|\Gamma_{ij} - \rho(v^{ex})^2 \delta_{ij}|)^2 \tag{3.6}$$

to optimally determine the elastic constants from arbitrary directions, where $v^{ex}$ are the wave speeds of three bulk modes measured experimentally. The elastic constants $c_{ijkl}$ of the above overdetermined equation systems are numerically obtained to minimize $\sum_i^{3n} \phi_i^2$ by using the same calculation algorithm as that used in the first method. $\Gamma_{ij}$ is updated only if "better" $c_{ijkl}$ are found.

Using the same initial estimate of stiffness constants as used above, the final results of elastic constants of $GaAs$ extracted using this method are $c_{11} = 118.8GPa$, $c_{12} = 53.80GPa$, $c_{44} = 59.39GPa$. The results from this method are very close to the results from the first method as shown in table 3.3.

Although anisotropic engineering materials such as synthetic composites have different structures from the anisotropic crystal, the elastic continuum theory can still be used to study their elastic wave behavior. In these cases, recovery of the orientation of the principal acoustical axes with respect to the crystallographic axes are important and a numerical method to do so has also been discussed by Castagnede [64].

### 3.3.3 Group Iteration Method

The third method (refer to Harder [66]) for extracting elastic constants is formed by rearranging the Christoffel equation into a system of equations linear in the independent elastic constants. Thus

$$c_{ijkl}p_i n_j p_k n_l = \rho(v^{ex})^2, \tag{3.7}$$

where $n_i$ is the unit vector describing the direction of propagation, $v$ is the measured phase velocities, and $p_i$ is the unit vector describing the directions of polarization which are mutually orthogonal. The left hand of equation 3.7 is a polynomial including both stiffness constants $c_{ijkl}$ and polarization vector $p_i$ as unknown parameters.

In order to solve this system of equations for stiffness constants, $p_i$ has to be given an initial estimate for each velocity measurement. If $N$ is the number of velocity observations, $M$ is the number of independent elastic constants to be found for a symmetry class, and $N > M$, the unknown elastic constants can be solved simultaneously through the above system of equations in which a group iteration technique

| No. of iteration | $c_{11}(GPa)$ | $c_{44}(GPa)$ | $c_{12}(GPa)$ |
|---|---|---|---|
| 1 | 113.5 | 41.28 | 25.48 |
| 2 | 118.7 | 59.45 | 75.74 |
| 3 | 118.8 | 59.40 | 55.29 |
| 4 | 118.8 | 59.39 | 53.84 |
| 5 | 118.8 | 59.39 | 53.83 |
| 6 | 118.8 | 59.39 | 53.83 |

Table 3.4: Stiffness constants of GaAs from the group iteration method.

is involved. Based on these obtained elastic constants and Christoffel's equation, the eigenvalues (therefore velocity $v^{th}$) can be solved to compare with the values of the measured velocity $v^{ex}$ and eigenvectors can be obtained as a better estimation of the unit polarization vector. These polarization vectors are used to obtain "better" elastic constants and then repeated for velocity and polarization. The iteration continues until the value of $|(v^{th})^2 - (v^{ex})^2|$ become reasonably small.

Table 3.4 shows the results of the stiffness constants after the first six iterations using the initial estimate of polarization and updated polarization as shown in table 3.5.

In the above example, if the initial polarization is assumed to be $p1 = \sin\theta\ \cos\phi$, $p2 = \sin\theta\cos\phi$, $p3 = \cos\theta$ for longitudinal, $p1 = -0.9$, $p2 = 0.5$, $p3 = -0.2$ for transverse 1 and $p1 = -0.8$, $p2 = -0.2$, $p3 = 0.1$ for transverse 2, the converged stiffness constants are $c_{11} = 120.3(GaPa)$, $c_{44} = 58.67(GaPa)$, $c_{12} = -14.91(GaPa)$, which are obviously incorrect. It is shown that the results of the stiffness constants converge

| No. of iteration | $\theta$ | $\phi$ | v(km/s) | p1 | p2 | p3 |
|---|---|---|---|---|---|---|
| 1 L | 7.757 | 16.76 | 4.785 | 0.129 | 0.038 | 0.991 |
| 1T1 | 7.757 | 16.76 | 3.342 | -0.9 | 0.5 | 0.2 |
| 1T2 | 7.757 | 16.76 | 3.273 | -0.8 | 0.5 | 0.7 |
| 2 L | 7.757 | 16.76 | 4.785 | -0.395 | -0.123 | -0.910 |
| 2T1 | 7.757 | 16.76 | 3.342 | 0.242 | -0.969 | 0.026 |
| 2T2 | 7.757 | 16.76 | 3.273 | -0.886 | -0.209 | 0.413 |
| 3 L | 7.757 | 16.76 | 4.785 | -0.267 | -0.081 | -0.960 |
| 3T1 | 7.757 | 16.76 | 3.342 | 0.214 | -0.976 | 0.023 |
| 3T2 | 7.757 | 16.76 | 3.273 | -0.939 | -0.199 | 0.278 |
| 4 L | 7.757 | 16.76 | 4.785 | -0.233 | -0.071 | 0.969 |
| 4T1 | 7.757 | 16.76 | 3.342 | 0.204 | -0.988 | 0.023 |
| 4T2 | 7.757 | 16.76 | 3.273 | -0.950 | -0.192 | 0.243 |
| 5 L | 7.757 | 16.76 | 4.785 | -0.231 | -0.070 | -0.970 |
| 5T1 | 7.757 | 16.76 | 3.342 | 0.203 | -0.979 | 0.023 |
| 5T2 | 7.757 | 16.76 | 3.273 | -0.952 | -0.192 | 0.240 |
| 6 L | 7.757 | 16.76 | 4.785 | -0.231 | -0.070 | -0.970 |
| 6T1 | 7.757 | 16.76 | 3.342 | 0.203 | -0.979 | 0.023 |
| 6T2 | 7.757 | 16.76 | 3.273 | -0.952 | -0.192 | 0.240 |

Table 3.5: Initial estimated polarizations and their updated values for GaAs. The initial polarization for the longitudinal wave is chosen the same as the propagation direction [ 0.129 , 0.038, 0.991].

very quickly if a suitable estimate of initial polarization is selected. In fact, the initial estimate of polarization of transverse waves should be within 45° of the true polarization for a good convergence.

### 3.3.4 Perturbation Series Expansion

The fourth method of determining elastic constants from wave-speed measurements uses a perturbation series expansion (refer to J.R. Neighbours [65]) to obtain the solution to a modified equation of motion, which describes the plane waves propagating in the $x'$ direction. Under the rotated (primed) coordinate system, the perturbation solution of elastic constants to the equation are

$$c'_{11} = \rho v_1^2 - [(\frac{(c'_{15})^2}{c'_{11} - c'_{55}}) + (\frac{(c'_{16})^2}{c'_{11} - c'_{66}}) + \frac{2c'_{15}c'_{16}c'_{56}}{(c'_{11} - c'_{55})(c'_{11} - c'_{66}}] \tag{3.8}$$

$$c'_{66} = \rho v_2^2 - [(\frac{(c'_{16})^2}{c'_{66} - c'_{11}}) + (\frac{(c'_{56})^2}{c'_{66} - c'_{55}}) + \frac{2c'_{15}c'_{16}c'_{56}}{(c'_{66} - c'_{11})(c'_{66} - c'_{55})}], \tag{3.9}$$

$$c'_{55} = \rho v_3^2 - [(\frac{(c'_{15})^2}{c'_{55} - c'_{11}}) + (\frac{(c'_{56})^2}{c'_{55} - c'_{66}}) + \frac{2c'_{15}c'_{16}c'_{56}}{(c'_{55} - c'_{11})(c_{55} - c'_{66})}], \tag{3.10}$$

where $v_1, v_2$ and $v_3$ correspond to the velocities of the one quasi-longitudinal and two (quasi) transverse modes. That only six primed elastic constants appear in the above equations is due to the choice of $x'$ as the propagation direction of sound waves. Through the Bond method [45] for transforming elastic constants under two sets of coordinate systems in abbreviated subscript notation, the $c'_{ij}$ are related to $c_{ij}$ by a linear function of $c_{ij}$.

If $m$ unknown elastic constants are to be found, the $m$ linear equations must be formed from a maximum integer of $m/3$ propagation directions of waves with three

measured velocities in each observation direction. In the most general triclinic case (21 unknowns), at least 7 directions are needed for the velocity measurements.

For the first approximation, neglecting the small terms appearing in the square brackets, $m$ unknown $c_{ij}$ can be solved. These values are then used to calculate the square-bracketed terms which are then used as a correction to the previously obtained values. In the program, an iterative technique has been used to solve the system of equations consisting of linear functions of the desired elastic constants $c_{ij}$.

For calculational convenience, the $x'$ axis is chosen in the arbitrary observation direction of velocity measurements, $y'$ is chosen to lie in the x-y plane, with $z'$ then being determined so as to preserve a right handed coordinate system. In this case, the Bond matrices for the elastic constants can be written out easily for all crystal classes. The elastic constants used in the Bond method are in abbreviated subscripts and can be easily carried out for transformation into another set of coordinates $(x', y', z')$. Extensive numerical calculations have been carried out for various velocity observation directions ($x'$ direction) and the results are presented as table 3.6.

It is shown from table 3.6 that the convergence of elastic constants depends on the propagation direction of the sound-waves. This approach may be used successfully for experimental data in some measurement directions, but serious errors occur in other directions. For instance, a singularity occurs in the direction defined by $\vartheta = 60.10(rad)$ and $\phi = 59.18(rad)$.

| No. | $\theta(rad)$ | $\phi(rad)$ | $c_{11}(GPa)$ | $c_{44}(GPa)$ | $c_{12}(GPa)$ |
|---|---|---|---|---|---|
| 1 | 7.75695 | 16.7618 | 119.0 | 59.29 | 22.90 |
| 2 | 33.1938 | 32.8542 | 120.4 | 58.61 | 51.93 |
| 3 | 3[illegible]8 | 40.1142 | 120.2 | 58.72 | 51.90 |
| 4 | 50.4026 | 16.7618 | 119.1 | 59.21 | 53.67 |
| 5 | 50.4026 | 32.8542 | 127.7 | 54.92 | 57.09 |
| 6 | 61.1056 | 59.1754 | $32.23\,10^3$ | $-161.0\,10^3$ | $93.10\,10^3$ |
| 7 | 61.1056 | 70.908 | 132.6 | 52.51 | 47.99 |
| 8 | 71.2303 | 32.8542 | 177.7 | 29.93 | 57.10 |
| 9 | 81.4565 | [illegible]1576 | 148.6 | 44.48 | -81.06 |
| 10 | 88.5843 | [illegible] | 124.6 | 56.53 | -116.7 |

Table 3.6: Stiffness constants of $GaAs$ extracted from the series expansion method.

## 3.4 Discussion and Conclusions

Numerical calculations have also been carried ou to extract elastic consts nts of $GaAs$ in or near the [111] direction of the conical point, and it is found that Neighbours' method gives the results of stiffness as $c_{11} = 154.7(GaPa)$, $c_{44} = 41.47(GaPa)$, $c_{12} = 71.73(GaPa)$ in this direction, which are certainly wrong. It indicates that Neighbours' method cannot be applied to wave propagation in a direction where a conical point exists. For Harder's method, the correct converged results can be obtained only if the suitable initial polarization is estimated. It is also proved that the first two methods can still be applied to the wave propagating in the direction of a conical point.

In summary, four different methods for inversion of the measured phase velocities of bulk sound waves to obtain elastic constants have been discussed and compared. These methods apply to wave propagation in arbitrary directions for any crystal class. Suitable iterative techniques have been successfully used to code computer programs to optimally recover the elastic constants for the over determined systems of equations. We conclude that the first two methods discussed here are more robust and can be widely used in any general cases. The third method has the limitation of the initial estimate of polarization having to be reasonably close to the true polarization, while the fourth method must be used with great care, as its convergence is a function of the propagation direction of the measured velocities.

From a practical point of view, the best method of extracting elastic constants should be a hybrid one. If possible, the measurements should first be chosen along the

highly symmetry directions such as crystal axes, in which some of the elastic constants can be obtained. The numerical computation for the rest of elastic constants by measuring the phase velocities of waves propagating in any arbitrary directions can be much simplified with these elastic constants being known.

# Chapter 4

# Surface Waves in Hard Films on a Substrate

Rayleigh surface waves on plane bounded solids usually refer to the waves whose displacement amplitudes decay exponentially with the increasing distance from the surface and the related elastic energy flow density is confined to a small region beneath the surface. Earlier work on the theories of surface waves based on both the elastic continuum and discrete particle modes were discussed for cubic crystals by Gazis et al. [73]. The latter model considers the propagation medium as a lattice of interacting discrete atoms rather than a continuum. In addition, Barnett et al. [74] have developed a theory to study surface waves in anisotropic crystals. In this theory, the Rayleigh velocity is obtained by making the smaller eigenvalues of a certain $2 \times 2$ real symmetric matrix vanish. In this chapter, the surface waves discussed are restricted to non-piezoelectric solid materials and the numerical calculations concerned based on the elastic continuum theory as treated in reference [46].

The purpose of this chapter is to use an easily understood classical method to study theoretically the surface acoustic wave in both a single crystal and thin solid films. This is necessary for one to gain the basic knowledge for the propagation properties of surface acoustic modes in a medium. As a preliminary to studying surface waves propagating in thin solid films, the surface wave for a infinite half space case is treated in section 1. The s... ($v$) of $TiN$ films with large thickness ($> 500nm$) are calculated using ... th isotropic and preferred orientation cases. The angular dispersion relations ... $\phi$ on different crystal planes of single cubic $TiN$ are also obtained for comparison purposes, where $\phi$ describes the propagation directions on a crystal plane. A computer program is coded to carry out the numerical computation procedure to seek the Rayleigh phase velocities in any propagation directions for any of the crystal classes.

In section 2, surface waves in thin solid films are discussed with more complicated boundary conditions being taken into account. The averaged polycrystalline elastic constants are used to simplify the model to an isotropic case. Extensive numerical calculations are carried out for the $TiN/HSS$ combination with $k_{\|}h$ ranging from 0 to 19, where $k_{\|}$ is the wave vector component parallel to the film surface and $h$ is the film thickness. It is found that the surface wave velocities converge to a definite value for large values of $k_{\|}h$, and, in fact, this value is the Rayleigh velocity of the film materials calculated in infinite half space situation. This implies that the acoustic behavior of a supported film is independent of that of the substrate on which it locates if the film thickness in the order of micrometer magnitudes. On the other hand, if the film thickness is less than a few hundred nanometers, the surface velocities in the films are

found to be a function of the film thickness and the dispersion relations ($v$ $vs.$ $k_{\|}h$) can be obtained. As the $k_{\|}h$ increases, the Rayleigh velocity of the substrate increases its value and become a highly damped p-SAW for a particular rang.. :f $k_{\|}h$, and finally converges to the Rayleigh velocity of the film material for a even larger $k_{\|}h$. We have coded a computer program to do the numerical computations for the dispersion relations of $TiN/HSS$.

## 4.1 Surface Waves in a Half Infinite Space

The following treatment of surface waves in a semi-infinite space is based on that of Farnell's [46] to illustrate the procedures adopted in our numerical calculations although some other approaches are also developed [61]. The solutions for the Rayleigh wave are obtained by applying suitable boundary conditions to equation (4.1) to follow, i.e. the traction stress components perpendicular to surface varnish at the free surface and the particle displacement amplitudes decay to zero when the distance from surface is infinite.

### 4.1.1 Theoretical Model

In the absence of the piezoelectric effect and external forces, the wave equation for the displacement in a perfect elastic and homogeneous medium is

$$\rho \frac{\partial^2 u_j}{\partial t^2} = c_{ijkl} \frac{\partial^2 u_k}{\partial x_i \partial x_l}, \tag{4.1}$$

where $u_j$ and $c_{ijkl}$ are respectively the displacement components and stiffness tensor, and $\rho$ is the mass density of the medium. The usual convention regarding summation

over repeated subscripts is used here.

If the coordinate system is chosen with $x_3$ as the outward normal to the free surface and with the origin at the surface, the boundary conditions can be expressed as

$$T_{3j} = c_{3jkl}\frac{\partial u_k}{\partial x_l} = 0, \qquad \text{at} \quad x_3 = 0 \tag{4.2}$$

and

$$u_j = 0, \qquad \text{at} \quad x_3 \to -\infty, \tag{4.3}$$

where $T_{3j}$ are the stress components parallel to the surface normal.

The possible compound displacements are assumed as

$$u_j = \sum_{n=1}^{3} c_n \alpha_j^{(n)} \exp[ik(l_i^{(n)} x_i - vt)], \tag{4.4}$$

which is the linear combinations of three partial waves, where $l_1^{(n)}$, $l_2^{(n)}$ are the direction cosines of surface wave propagation known, $l_3^{(n)}$ are the three complex roots of equation (3.2) with the negative imaginary parts in terms of surface wave velocity ($v$), $\alpha_j^{(n)}$ are the components of the eigenvector of equation (3.1) corresponding to the $l_3^{(n)}$ and $c_n$ are the three weighting factors. Substituting $u_j$ into the boundary condition (4.2), these factors can be determined by enabling the determinant of the 3 by 3 matrix of the coefficients to be zero in order to find non-trivial solutions, i.e.

$$\det |d_{mn}| = 0, \qquad \text{with} \qquad m,\ n = 1, 2, 3., \tag{4.5}$$

where

$$d_{mn} = c_{m3kl}\alpha_k^{(n)} l_l^{(n)}, \qquad \text{with} \quad l_1^{(n)} \equiv l_1, \quad l_2^{(n)} \equiv l_2. \tag{4.6}$$

The computer programs have been coded to seek the numerical solutions of the phase velocities existing in a particular propagation direction on any crystal plane of any symmetry classes using the theory discussed above. The details of the procedure are as follows.

### 4.1.2 Computation Procedure

For a crystal plane with its normal direction as $[b_1, b_2, b_3]$ with respect to crystal axes, the reference coordinate system is chosen with the $z$ axis parallel to this normal. Using the Bond method, the elastic constants are rotated to the reference axes. Equation (3.2) is the sextic equation in $l_3$ with $v$ as a parameter. The propagation direction on the plane perpendicular to $z$ axis is described by $l_1(\phi)$ and $l_2(\phi)$.

For a pre-assumed value of $v$ , three pairs of complex-conjugate roots to this equation can be obtained with a known propagation direction. Only the three roots $l_3^{(n)}$ $(n = 1, 2, 3.)$ with negative imaginary parts are useful for a surface problem due to the boundary condition (4.3). There are three Christoffel matrices $\Gamma_{jk}^{(n)} = l_i^{(n)} l_l^{(n)} c_{ijkl}$ corresponding to these three $l_3^{(n)}$. Using the equation (3.2), three eigenvalues and three eigenvectors can be obtained for each $\Gamma_{jk}^{(n)}$. There are altogether nine eigenvectors of three $\Gamma_{jk}^{(n)}$ available, but only three of them can be used in equation (4.6). Three useful eigenvectors $\alpha_k^{(n)}$ are those whose corresponding eigenvalues from three $\Gamma_{jk}^{(n)}$ have the same value (phase velocity). By substituting the rotated elastic stiffness $c_{m3kl}$, eigenvectors $\alpha_k^{(n)}$ and the direction cosines $l_l^{(n)}$ into equation (4.6) for the $d_{mn}$, it is determined whether $\det |d_{mn}|$ is zero. If yes, the assumed value of velocity is the

needed phase velocity in the known propagation direction, otherwise, various values of velocities have to be tried until det $|d_{mn}|$ becomes zero.

It should be noted here that "zero" actually does not exist due to the limited accuracy of numerical calculations by computers and as long as the value of det $|d_{mn}|$ becomes small enough, the corresponding assumed value of velocity can be regard as the surface wave velocity.

### 4.1.3 Iterative Method in Searching for the Rayleigh Velocity

Using the procedure described above, it is almost impossible to find the surface velocity with a randomly assumed velocity. A suitable method of selecting the velocities are needed to minimize recursion times and find a real surface wave instead of a pseudo-surface wave. Because the Rayleigh surface wave velocity is less than the bulk transverse velocity (the lower one) in the same propagation direction, this bulk velocity is chosen as the upper limit ($v$max) for the assumed value of Rayleigh velocities. The lower limit ($v$min) for the Rayleigh velocity is empirical and, for most solid materials, half the value chosen for the upper limit can be used as the said lower limit to narrow the velocity range. In case the velocity found is close to the lower limit, this limit should be reset to a even smaller one. It should be noted that $v$max and $v$min are updated for each different propagation direction.

The seeking procedure throughout our computer programs is illustrated in figure (4.1).

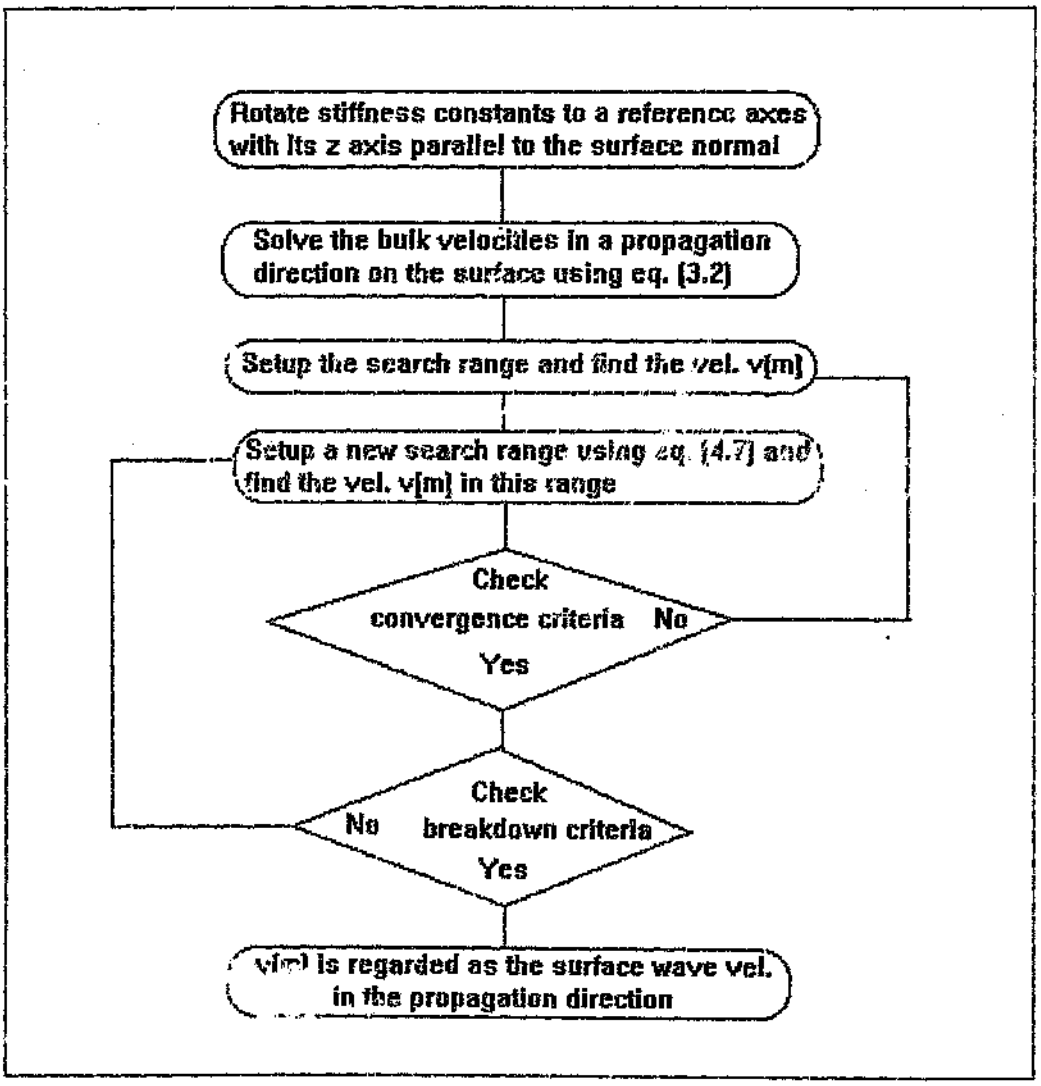


Figure 4.1: Flowchart of search procedure for the SAW velocity in a half infinite medium.

The velocity range ($v\max - v\min$) is first divided by a step ($di$) to make $\frac{(v\max - v\min)}{di}$ +1 individual velocities for a specific propagation direction. These velocities are used to calculate their corresponding $3 \times 3$ determinants in formula (4.5). Among them, the velocity $v_m$ whose corresponding determinant is the least is found and then used as the middle point of a new velocity range for the second recursion. The new range is defined as

$$(v_m + \frac{9 \times di}{10} - (v_m - \frac{9 \times di}{10})) \tag{4.7}$$

with a new step as $di = \frac{di}{5}$. This range is updated every time by repeating the above procedure for the updated $v_m$ and $di$. The absolute value of the determinant should decrease after each recursion and this serves to check the convergence of $v_m$. If not, the initial velocity search range must be reset The break-down criteria for the recursion is chosen as the difference $\Delta v$ between the $v_m$ in the previous recursion and the current $v_m$. When the pre-set accuracy for $v_m$ is achieved, (for instance, the absolute value of $\Delta v \leq 10^{-6}$), the recursion will stop and the current $v_m$ can be regarded as the required surface velocity.

The absolute value of the determinant can also be used as a breakdown criterion. In this case, the difference of the determinants between the previous and current recursion is preset to stop the search.

### 4.1.4 Application to Rayleigh Velocities of $TiN$ and $HSS$

As an example of the above numerical seeking procedure, Rayleigh velocities of $TiN$ are calculated both in the polycrystalline aggregate and single crystal forms.

| Polycrystal | vL(m/s) | vT1(m/s) | vT2(m/s) | RWV(m/s) |
|---|---|---|---|---|
| TiN | 9378.86 | 5749.40 | 5749.40 | 5236.68 |
| TiN* | 10254.8 | 5887.04 | 5887.04 | 5416.62 |
| HSS | 5872.58 | 3141.94 | 3141.94 | 2913.68 |

Table 4.1: Bulk and Rayleigh velocities of TiN and HSS with a random distribution of crystallites.

For the polycrystalline aggregates with randomly distributed crystallites, the calculated mean values of Voigt's and Reuss' averaged stiffness constants of $TiN$ are $c_{11} = 475$, $c_{12} = 118$ and $c_{44} = 179GPa$ (see table 2.3). The stiffness constants of $HSS$ based on its Young's modulus and Poisson's ratio [75] are $c_{11} = 269$, $c_{12} = 115$ and $c_{44} = 76.9\ GPa$. The densities (in $g/cm^3$) used in the calculations are 5.40 for $TiN$ and 7.80 for $HSS$.

In this case, in fact, the Rayleigh velocity ($v$), can be easily obtained using the equation for isotropic materials as (see reference [46])

$$\left[2 - (v/v_t)^2\right]^2 = 4\left[1 - (v/v_l)^2\right]^{1/2}\left[1 - (v/v_t)^2\right]^{1/2}, \tag{4.8}$$

where $v_l$ and $v_t$ are the bulk longitudinal and transverse velocity of the medium.

Numerical solutions of Rayleigh velocities using equation (4.8) and bulk velocities of $TiN$ and $HSS$ are listed in table 4.1. For a description of the $TiN$ and $TiN^*$, see section 2.3.1.

For polycrystalline $TiN$ and $TiN^*$ with the preferred orientation [111] being taken into account, the arithmetic average of stiffness constants in table 2.4 are adopted to calculate their Rayleigh velocities. The numerical computation procedure described

| Polycrystal (111 orientation) | vL(m/s) | vT1(m/s) | vT2(m/s) | SWV(m/s) |
|---|---|---|---|---|
| TiN | 9356.22 | 5798.05 | 5742.56 | 5261.28 |
| TiN* | 10212.1 | 5988.32 | 5861.95 | 5430.97 |

Table 4.2: Bulk and Rayleigh velocities of TiN with a [111] preferred distribution of crystallites.

in section 4.1 is used to find the velocity for a "zero" determinant. No angular dispersion relation exists due to the transversely isotropic surface elastic properties of these polycrystalline aggregates. The surface wave velocities of any propagation direction are the same on the film surface. It should be noted that the two bulk transverse velocities are not exactly degenerate in this case. The results are listed in table 4.2.

### 4.1.5 Angular Dispersion Relations of Cubic *TiN*

For a single crystal, the surface wave velocity is usually a function of propagation directions on the crystal plane. For comparison purposes, the dispersion relations ($v$ vs. $\phi$) of cubic *TiN* crystal on various crystal planes are calculated. The results together with velocities of bulk modes are plotted as shown in figures (4.2, 4.3, 4.4).

In the figures, the curves marked T1 and T2 are the phase velocities of the two transverse bulk waves with their displacements perpendicular and parallel to the wave propagation plane respectively and the SAW represents the Rayleigh-type surface wave propagating on the plane. The propagation direction is indicated by the abscissa of each figures, giving the angular variations from a chosen crystallographic direction

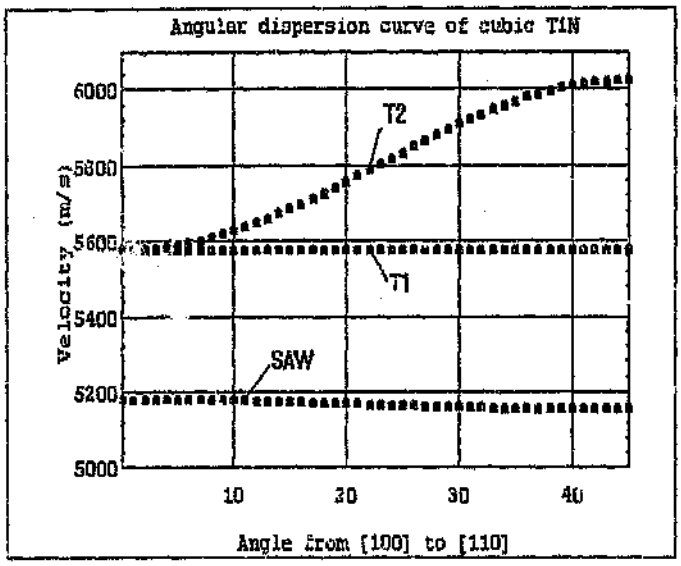


Figure 4.2: Transverse and surface wave velocities for propagation on the [001] plane of cubic *TiN*.

towards a second direction.

In the figure (4.2), the bulk wave T1 has its phase velocity independent of the propagation direction on [001] plane and the SAW also tends to be quite independent of angle. Bulk waves T1 and T2 have the same velocity (are degenerate) in the crystal axis [001] pure mode direction. The surface wave does not degenerate into a transverse bulk wave at any angle on this plane and its phase velocity is always less than that of bulk waves. The velocity curves on this plane has mirror symmetry about the 45° direction; therefore the curves are plotted only in the range of $0 - 45°$.

Elastic waves propagating on [110] crystal plane are shown in figure (4.3). The phase velocities of the T1 and T2 bulk waves become degenerate in the $[\bar{1}10]$ direction

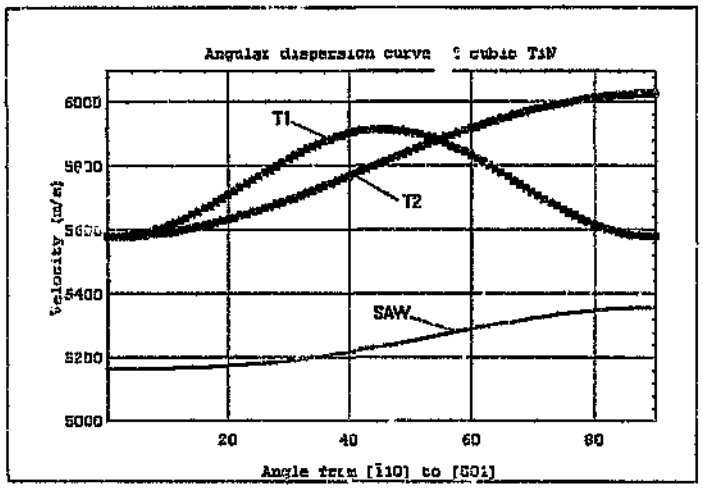


Figure 4.3: Transverse and surface wave velocities for propagation on the [110] plane of cubic *TiN*.

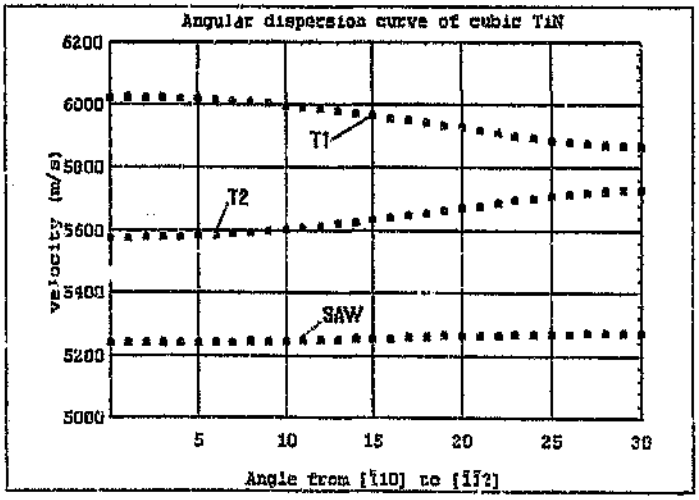


Figure 4.4: Transverse and surface wave velocities for propagation on the [111] plane of cubic *TiN*.

and also around 55° from this direction on the plane. The phase velocity of the surface wave is stable from 0 to 30° and then increases steadily to 90°. T1 starts decreasing after 30° from the [$\bar{1}$10] direction. T2 has the similar trend to that of the surface wave.

For propagation on the [111] non-mirror plane of crystal symmetry as shown in figure (4.4), T1 always has a higher phase velocity than T2. The phase velocity of the surface wave is relatively constant which is close to that of an isotropic medium. All the curves have hexagonal symmetry on the plane and mirror symmetry about the angle 30°; they are plotted in the range from 0 ([$\bar{1}$10] direction) to this angle.

The angular dispersion relations of the surface mode of the cubic $TiN$ are close to those of an isotropic medium since its anisotropy factor is 0.89 as given by equation (3.4), which is close to the isotropic value 1.

## 4.2 Surface Wave Velocity in Solid Films

Solid films are usually deposited using various vapour deposition techniques and normally exist in the form of polycrystalline aggregates. The surface wave velocities in the films can be obtained using the same algorithm as in section 4.1 with more complicated boundary conditions being applied. The surface waves in polycrystalline films, in fact, can be simplified to an isotropic problem if the averaged elastic constants are used in calculations. The following discussion is restricted to non-piezoelectric media. Emphasis is given to isotropic cases to simplify the theoretical calculations; this approach provides a good approximation for preferentially orientated $TiN$ films.

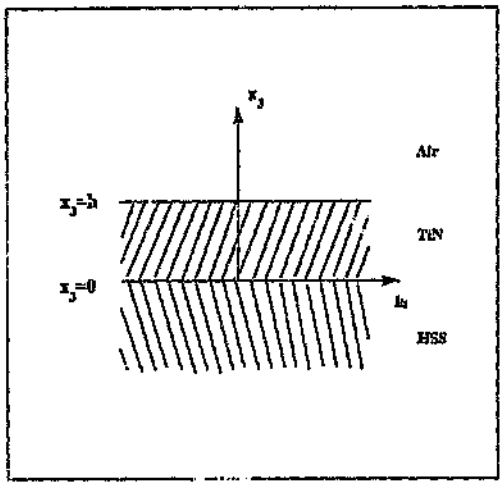


Figure 4.5: Cocrdinate system for surface acoustic waves in a solid film.

### 4.2.1 Bound. ry Conditions

The coordinate system is chosen the same way as described in section 4.1 except that the origin is at the interface between film and substrate as shown in figure (4.5).

If the thickness of the film is $h$, the free surface of the film is at $x_3 = h$. Like those discussed in section 4.1, the particle displacements decay to zero with infinite depth below the interface and the three traction components must vanish on the upper film surface. If we assume the films have intimate mechanical contact with the substrates, at the interface ($x_3 = 0$), the particle displacements and the traction stress components from both media must be equal, i.e.

$$u_j = 0, \qquad \text{at } x_3 \to -\infty, \tag{4.9}$$

$$T^f_{3j} = 0, \qquad \text{at } x_3 = h, \tag{4.10}$$

$$u^s_j = u^f_j, \qquad \text{at } x_3 = 0, \tag{4.11}$$

and

$$T^s_{3j} = T^f_{3j}, \qquad \text{at } x_3 = 0, \tag{4.12}$$

where $j = 1, 2, 3$, the superscript $f$ indicate the parameters for films and superscript $s$ for substrate.

### 4.2.2 $9 \times 9$ Coefficient Determinant

Since the boundary condition (4.9) must be complied with, the $u^s_j$ are the same as those in equation (4.4) which consist of three partial waves corresponding to the three complex roots of $l^{(n)}_3$ $(n = 1, 2, 3)$ from equation (3.2) with negative imaginary parts. It should be noted here that the $u^f_j$, however, are totally different. Due to the finite thickness $(h)$ of film, the wave in this film does not have to be exponentially decaying and the six roots of $l^{(n)}_3$ $(n = 1, 2, ..6.)$ from equation (3.2) can all be accepted. In other words, the particle displacement amplitudes can grow, decay and remain constant in the film. Thus the $u^f_j$ are, in fact,a linear combination of six partial waves in the films with applicable weighting factors in order to satisfy the above boundary conditions. The expression for $u^f_j$ is the same as in equation (4.4) except here $n = 1, 2...6$.

Substituting the $u^s_j$ and $u^f_j$ into boundary conditions $(4.10 - 4.12)$, we have a set of nine equations with the weighting factors $c^s_n$ $(n = 1, 2, 3)$ and $c^f_n$ $(n = 1, 2...6)$ as the unknown parameters. In order to find the non-trivial solutions for this set of equations, a "suitable" velocity must enable the determinant of the $9 \times 9$ matrix of

coefficients the set of equations equal to "zero". This suitable velocity is the required surface velocity in solid films and can be obtained by the same search strategy as in section 4.1.3.

### 4.2.3 Surface Wave Velocity in Isotropic Films

For an isotropic case, since both the wave equation and boundary conditions are separated into two uncoupled sets, two different independent types of waves are found. Those waves with transverse displacements ($u_2^s$ and $u_2^f$) perpendicular to the sagittal-plane are called "Love waves". They are not observed in Brillouin scattering through the ripple scattering mechanism. Only the waves with sagittal-plane displacements are discussed here. The sagittal plane is a plane including the propagation vector and a perpendicular to the film surface. In the isotropic case, the above mentioned $9 \times 9$ matrix of coefficients simplified to a $6 \times 6$ matrix for sagittal-plane solutions.

For isotropic media, the propagation direction can be chosen along the $x_1$ axis ($l_1 = 1,\ l_2 = 0, l_3 = l$) without losing generality. Thus the Christoffel's matrix $\Gamma_{jk} = l_i l_l c_{ijkl}$ for isotropic media is

$$\begin{pmatrix} c_{11} + c_{44}l^2 & 0 & (c_{11} - c_{44})l \\ 0 & c_{44}(1 + l^2) & 0 \\ (c_{11} - c_{44})l & 0 & c_{44} + c_{11}l^2 \end{pmatrix}.$$

Using the equation (3.2), the $l$ are solved and are expressed in term of surface wave phase velocity $v$.

For the particle displacements in the sagittal plane in the substrate, only two roots

are found to be useful

$$l^{s(1)} = -i[1 - (v/v_{st})^2]^{1/2} \tag{4.13}$$

$$l^{s(2)} = -i[1 - (v/v_{sl})^2]^{1/2}. \tag{4.14}$$

where $v_{st}$ and $v_{sl}$ are the shear and longitudinal velocities of bulk waves in the substrate.

For the particle displacements in the sagittal plane in the film, four roots are used

$$l^{f(1)} = +i[1 - (v/v_{ft})^2]^{1/2} \tag{4.15}$$

$$l^{f(2)} = +i[1 - (v/v_{fl})^2]^{1/2} \tag{4.16}$$

$$l^{f(3)} = -i[1 - (v/v_{ft})^2]^{1/2} \tag{4.17}$$

$$l^{f(4)} = -i[1 - (v/v_{fl})^2]^{1/2} \tag{4.18}$$

where $v_{ft}$ and $v_{fl}$ are the transverse and longitudinal velocities of bulk waves in the films.

Using the above roots and corresponding eigenvectors of equation ( 3.1) to obtain the particle displacements $u_j^s$ and $u_j^f$, then substituting these results into boundary conditions (4.10 to 4.12), we have the $6 \times 6$ determinant given by the left side of equation (4.19). Setting this determinant equal to zero, we can find the non-trivial

solutions of the weighting factors in the particle displacements.

$$\begin{vmatrix} l^{f(1)} & -1 & -l^{f(1)} & -1 & -l^{s(1)} & 1 \\ -1 & -l^{f(2)} & -1 & l^{f(2)} & 1 & l^{s(2)} \\ \Lambda & 2l^{f(2)} & \Lambda & -2l^{f(2)} & -r(1-(l^{s(1)})^2) & -2rl^{s(2)} \\ 2l^{f(1)} & -\Lambda & -2l^{f(1)} & -\Lambda & -2rl^{s(1)} & r(1-(l^{s(1)})^2) \\ \Lambda e^{a} & 2l^{f(2)}e^{b} & \Lambda e^{-a} & -2l^{f(2)}e^{-b} & 0 & 0 \\ 2l^{f(1)}e^{a} & -\Lambda e^{b} & -2l^{f(1)}e^{-a} & -\Lambda e^{-b} & 0 & 0 \end{vmatrix} = 0 \tag{4.19}$$

where $\Lambda = 1-(l^{f(1)})^2$, $a = ik_{\|}l^{f(1)}h$, $b = ik_{\|}l^{f(2)}h$ and $r = c^s_{44}/c^f_{44}$, i.e. the ratio of stiffness constants of the substrate ($c^s_{44}$) and of the solid film ($c^f_{44}$).

The phase velocity of the acoustic wave is implicit in equation (4.19) and is dependant on the product of $k_{\|}h$. The dispersion relation, i. e. $v$ as a function $k_{\|}h$ can be obtained through numerical calculations by solving the above equation. For a particular value of $k_{\|}h$, the seeking procedure for a required phase velocity is the same as that described in section 4.1.3.

### 4.2.4 Calculated Dispersion Curves ($v$ vs. $k_{\|}h$) of Polycrystalline $TiN$ Films

Using the averaged elastic constants of polycrystalline $TiN$ films, as an example, we calculate the dispersion curve for the $TiN/HSS$ combination. The elastic constants and densities of $TiN$ and $HSS$ used in the calculations are the same as those in section 4.1.4. The results are plotted using the coded computer program in figure (4.6) and the typical boundary determinant minima for the various modes are given

in figure (4.7).

For $k_{\|}h$ from 0 to 0.8, the phase velocity increases from the Rayleigh velocity ($v_{sr}$) to the bulk transverse velocity ($v_{st}$) of $HSS$ and the mode is a true SAW in which the corresponding boundary determinant minimum is zero and very sharp as shown in (a) of figure (4.7).

As $k_{\|}h$ increases from 0.8 to 1.1, the propagation velocities stay at the bulk transverse velocity ($v_{st}$) of $HSS$, the boundary determinant minimum and thus surface waves do not exist in this region and the mode is a bulk wave.

For $k_{\|}h$ from 1.2 to 4.7, the boundary determinant minimum does not reach zero and is very broad as shown by (b) of figure (4.7). In this section, the mode is a highly damped pseudo-SAW in which the wave propagation energy is not conserved at the surface region but instead there is radiation into the bulk.

For $k_{\|}h$ from 4.8 to 5.3, no determinant minimum is found. In the next chapter, the use of a Green's function method shows that there is a "pre-Rayleigh" mode existing in this range of $k_{\|}h$.

For $k_{\|}h$ from 5.4 to 8, the phase velocities decrease from a higher value to the Rayleigh velocity ($v_{fr}$) of bulk $TiN$. In this region, the boundary determinant displays a broad non-zero minimum as shown in (c) of figure (4.7). The acoustic mode in this region is the pre-Rayleigh which is still a type of p-SAW.

As $k_{\|}h$ further increases from 8, the propagation velocities are stable at the Rayleigh velocity of bulk $TiN$. The determinant minimum value is very large but its variation is very sharp like (d) of figure (4.7). The mode in this section is close to a true Rayleigh wave for $TiN$ as if there were no $HSS$ beneath the $TiN$ film. This

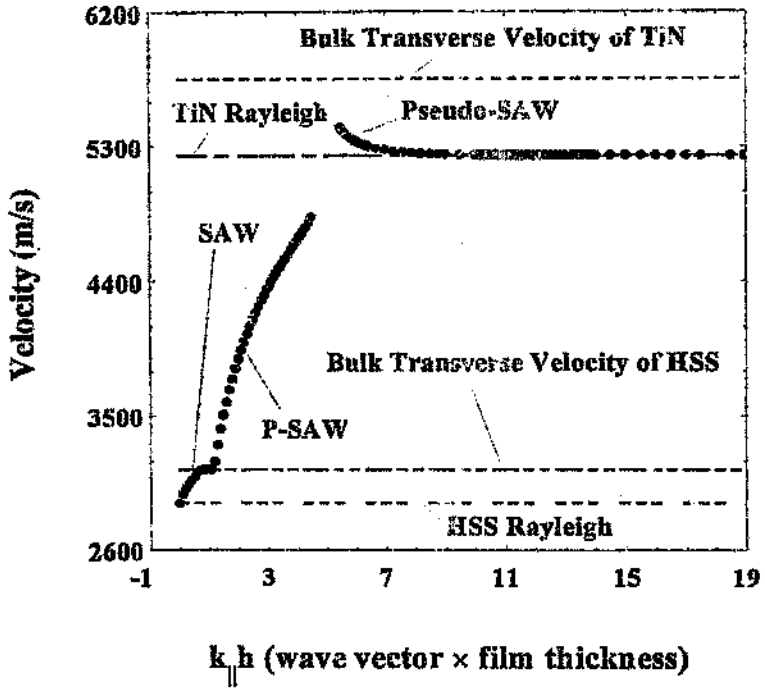


Figure 4.6: Dispersion relation, namely, phase velocity $v$ vs. $k_{\|}h$ for a polycrystalline *TiN* film on high speed steel.

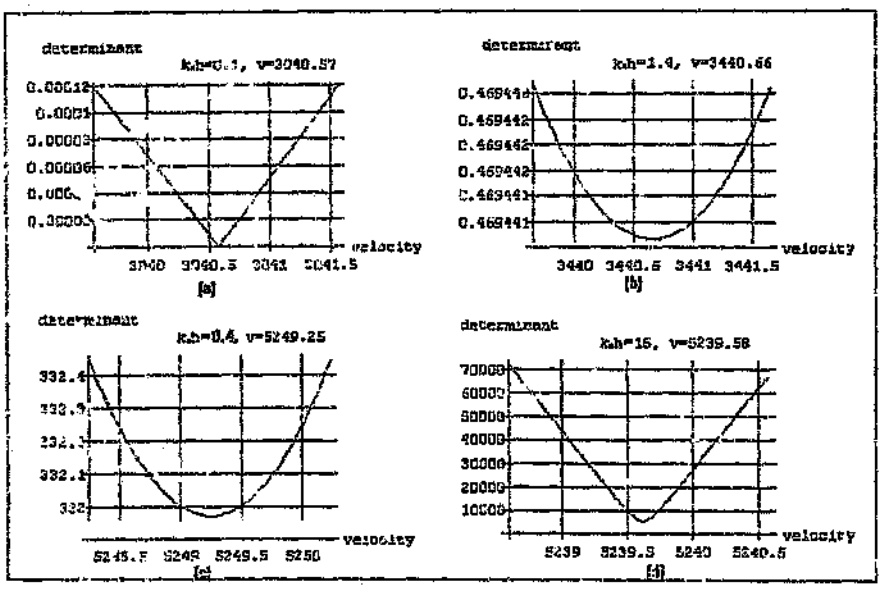


Figure 4.7: Boundary determinant minimum with some typical values of $k_{||}h$ for the *TiN/HSS* combination.

mode is defined as a quasi-Rayleigh wave in the next chapter.

## 4.3 Further Discussion

It should be noted that the characteristics of the dispersion relation discussed above only apply to the "stiffening" situation, in which the bulk transverse velocity of the film ($v_{lt}$) is greater than $\sqrt{2}$ times the bulk transverse velocity ($v_{st}$) of the substrate. For the $TiN/HSS$ combination, $v_{lt}/v_{st}$ is 1.83. In this case, the existence of the film increases the surface wave velocity from the Rayleigh velocity of a pure substrate to the Rayleigh velocity of a pure film with pseudo-surface waves present in a particular range of $k_{\|}h$ values.

On the other hand, if the bulk transverse velocity of the film ($v_{lt}$) is less than $1/\sqrt{2}$ times the bulk transverse velocity($v_{st}$) of substrate, the film is said to "load" the substrate. In this case, there exists an infinite number of Sezawa waves. lowest surface wave velocity decreases from the Rayleigh velocity of the substrate to the Rayleigh velocity of the film.

For a combination of materials with elastic parameters in which $v_{ft} \approx v_{st}$, a Stoneley wave may exist The Stoneley wave is a type of interface wave with only sagittal plane displacements which decay with increasing depth in both directions from the interface. The detailed discussion of the latter two cases is omitted here since no experimental measurements were done for those kinds of combinations.

At the initiation of the project, in all the references uncovered in the literature, the discussion of the dispersion relation in a stiffening case was limited to the range of $k_{\|}h$

from 0 to 1. The pseudo-surface wave is determined through numerical calculation using rather elaborate seeking methods for the phase velocity for large values of $k_{\|}h$. An unsuitable seeking minimum method may lead to a failure to obtain this pseudo-surface wave but always finds the bulk transverse velocities of films for $1 < k_{\|}h < 15$, which obviously are not correct for the surface wave problem.

In this chapter, a classical theoretical model for calculating surface acoustic waves for both single crystal and solid films has been described. The numerical calculations have been carried out for the $TiN/HSS$ combination using suitable boundary conditions and the dispersion relations ($v$ vs. $k_{\|}h$) are obtained consisting of the SAW, p-SAW and quasi-Rayleigh. Details of pre-Rayleigh and the higher order modes of p-SAW cannot be obtained by this model, which will be discussed using a Green's function method in the next chapter. The effect of the elastic moduli of $TiN$ on the dispersion relations will also be discussed there.

# Chapter 5

# Theory of Brillouin Scattering from a Supported Hard Film

In contrast to a soft film on a hard substrate, few studies have been done in the past on the theoretical calculations of Brillouin scattering spectra from the free surface of a hard film on a relatively soft substrate. In this chapter, Brillouin scattering spectra of various acoustic excitations localized near the surface are calculated using a Green's function method and based on the assumption of ripple scattering at the free surface. These include a SAW, a highly damped p-SAW, pre-Rayleigh, and quasi-Rayleigh waves and their higher order modes. It is found that the elastic constants of the film have a profound effects on the acoustic behavior of the combination. For a strongly stiffened system, there is a pre-Rayleigh mode appearing at large $k_{\parallel}h$ and there is a discontinuity in the dispersion curve. For a relatively weak stiffening system, no pre-Rayleigh mode is found and the p-SAW transfers into quasi-Rayleigh mode directly. However, the acoustic modes in both systems evolve into a quasi-Rayleigh wave of

the system at even larger $k_{\parallel}h$, which are very close to the Rayleigh wave of $TiN$.

In this chapter, we start with the basic concepts and scattering mechanism of Brillouin scattering in section 1. A general theory concerning all the possible scattering mechanisms is qualitatively summarized, with an emphasis on the ripple scattering mechanism which dominates elastooptic scattering in most of hard ceramic films. The calculation of the Brillouin scattering intensity or scattering cross section for a supported film is described in section 2. A Green's function method developed for the calculation of Brillouin scattering from acoustic excitations on the basis of ripple scattering is presented in detail. In section 3, numerical results for $TiN/HSS$ - a strongly stiffened system and reduced elastic moduli of $TiN$ films on $HSS$ -a relatively weak stiffening system are presented. Brillouin scattering spectra have been calculated for some typical film thicknesses, and display the effects of various acoustic modes. The effects of the elastic moduli and densities of $TiN$ films and $HSS$ on the dispersion relations are discussed.

## 5.1 Brillouin Scattering Mechanism

Acoustic waves can scatter light by two distinct mechanisms. Brillouin scattering from acoustic excitations is regarded as the transfer of momentum and energy between photons of incident light and the phonon field through the dynamical corrugation of the surface (ripple mechanism) and the modulation of the dielectric tensor of the medium (elasto-optical mechanism).

In the surface ripple scattering mechanism, the incident light is reflected from

the dynamic acoustic deformation of the sample surface, and the scattered light conserves only the wavevector component parallel to the surface. In the elasto-optical mechanism, the coupling of incident and scattered light occurs by way of the acoustic modulation of the material dielectric constant, and in case of transparent solids all wavevector components are conserved with real optical wavevectors.

The relative importance of the two mechanisms depends on the optical transparency of a solid. For a very transparent materials, where the incident light penetrates inside the medium, the bulk elasto-optic mechanism is dominant. The conservation of both the frequency and wavevector produces sharp scattering peaks of bulk acoustic modes in the spectrum. In the case of a less transparent solid such as a semiconductor, the two mechanisms may make comparable contributions. Both the surface and bulk acoustic modes can be investigated, but the interpretation is somewhat complicated by the breakdown of wavevector conservation in the direction perpendicular to the surface. For a highly opaque solid, where little light penetrates into the medium, the ripple mechanism is dominant [39]. Only the wavevector component parallel to the surface remains, and the spectra consists of a sharp Rayleigh wave peak wave together with a broad feature associated with the bulk wave continuum.

The surface ripple mechanism for the inelastic scattering of light can be understood as follows: For waves propagating on the surface, the vertical component of particle displacement results in dynamic corrugation of the surface. As a result, the surface acts as a moving diffraction grating. A light beam incident on the surface is diffracted and its frequency is modified (frequency shift) through the Doppler effect because of the movement of the corrugations.

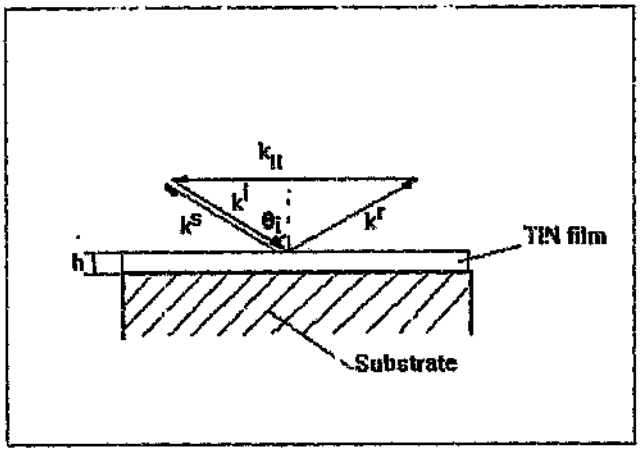


Figure 5.1: Wavevector diagram of the back-scattering geometry used in the experiment. $k^i$, $k^r$ and $k^s$ are wavevectors of incident, reflected and scattered light respectively.

For incident light polarized in the plane of the surface and in a back-scattering geometry ($\theta_i = \theta s$) as shown in figure (5.1), scattering by the ripple mechanism is proportional to the reflectivity of the material. For polarization in the sagittal plane, stronger scattering also exists for higher reflectivity materials although it is no longer proportional to the reflectivity. Opaque materials such as metals have stronger scattering contributed by means of the surface ripple mechanism than do transparent materials owing to their higher reflectivity.

For scattering from supported films, surface ripple scattering from both the surface and interface and elasto-optic coupling from the film and substrate may all make contributions. Bortolani et al. [43] have discussed the theory of Brillouin scattering for supported thin solid films on a semi-infinite substrate by taking all the possible

scattering mechanisms into account and also their interference. In their calculations, the cross section formulae for a general scattering geometry is obtained by solving Maxwell's equations with the appropriate boundary conditions using first order perturbation theory. It is found that scattering cross sections depend on the film thickness, and the intensity of the spectral lines oscillate with changing thickness.

### 5.1.1 Brillouin Scattering Cross Section - a General Case

With the coordinate system as shown in figure (4.5), the numerical results for the scattering intensity have the following form for the polarization of the incident and scattered light in a sagittal plane defined by $\mathbf{k}_{\|}$ and surface normal [38]:

$$\left[\frac{d^2\sigma}{d\Omega_s d\varpi}\right]_{p\to p} \propto \sum_{\lambda} a^{\lambda}[A_{\lambda,x}e_x^{(f)} + A_{\lambda,z}e_z^{(f)}] + A^{(f)}w_z(Q,\Omega,h) + \sum_{\mu} a^{\mu}[A_{\mu,x}e_x^{(s)} + A_{\mu,z}e_z^{(s)}] + A^{(s)}w_z(Q,\Omega,0) \qquad (5.1)$$

The first and the third terms in the square brackets refer to the elasto-optic coupling in the film and in the substrate respectively, which depend on particle displacement components of the film ($e_x^{(f)}$ and $e_z^{(f)}$) and the substrate ($e_x^{(s)}$ and $e_z^{(s)}$). The quantities $a^{\lambda}, e^{(f)}, a^{\mu}, e^{(s)}$ can be obtained by using the partial wave method to solve the Christoffel equations and applying the boundary conditions, i.e. the continuity of displacements and stress at the interface and vanishing of traction stresses at the film surface. The weighting factors $A_{\alpha,j}$ are linear combination of elasto-optic constants and are determined by electromagnetic boundary conditions. The terms $A^{(f)}w_z(Q,\Omega,h)$ and $A^{(s)}w_z(Q,\Omega,0)$ represent ripple scattering from the film surface ($z = h$) and from the interface ($z = 0$), which are proportional to the vertical com-

ponent of particle displacements at the film surface and at the interface.

It is shown in formulae (5.1) that the scattering cross section is modulated through the interference of the four contributions from ripple scattering and the elasto-optic mechanism. For an highly opaque thin film on a substrate, the main scattering mechanism is from the surface ripple, i.e. the second term in the formula. For more transparent films, all four contributions have to be taken into account. As pointed out by Bortolani et al.:" Although in general the ripple scattering mechanism is the dominant one it is found that the elasto-optic coupling in some films is not negligible and sometimes even prevailing".

### 5.1.2 Brillouin Scattering Intensity from Surface Ripple Scattering

For the $TiN/HSS$ combination, however, the ripple mechanism is the main scattering source due to the metal-like properties of $TiN$ and no pronounced oscillation in the scattering intensity is expected.

If only surface ripple scattering is considered, then at room temperature and above, the Brillouin scattering efficiency or intensity for scattering from a surface is given by Subbaswamy and Maradudin [76] as

$$I(\omega) \propto D\frac{T}{\omega} Im\left\{\tilde{G}_{33}(\mathbf{k}_{\parallel}, \omega + i0)\right\}, \tag{5.2}$$

where $\omega$ is angular frequency shift, $T$ is the absolute temperature, $\mathbf{k}_{\parallel}$ is the projection on the surface of the phonon wave vector, and $\tilde{G}_{33}(\mathbf{k}_{\parallel}, \omega + i0)$ is the component

of the Fourier (frequency and wavevector) domain elastodynamic Green's function pertaining to force and response normal to the surface. The factor $D$ depends on the medium (density $\rho$ and permittivity $\varepsilon$), scattering geometry, polarization and incident photon frequency $\omega_0$.

## 5.2 A Green's Function Method for the Calculation of Brillouin Scattering from a Supported Solid Film

From equation (5.2), it can be seen that calculating the Brillouin spectrum essentially reduces to a determination of $\tilde{G}_{33}(\mathbf{k}_{\|}, \omega + i0)$. In the following theoretical analysis, we outline how this is done.

Our theory is developed for the most general case of an elastically anisotropic film on an anisotropic substrate, although for the particular combination $TiN/HSS$, both are shown to be effectively isotropic.

We choose the coordinate system with $-x_3$ as the outward normal to the solid surface and with the origin at the interface. The substrate occupies the half-space $x_3 > 0$ and the film, which is of thickness $h$, occupies the region $-h < x_3 < 0$. Intimate mechanical contact is assumed between the film and substrate. $\tilde{G}_{33}(\mathbf{k}_{\|}, \omega)$ is the Fourier transform with respect to time and the spatial coordinates $\mathbf{x}_{\|} = (x_1, x_2)$ of the 33 components of the Green's function tensor $G_{ij}(\mathbf{x}, t)$, evaluated for force and displacement at the otherwise free surface of the film. The boundary conditions are

continuity of the stress components (traction forces) $\sigma_{\ell 3}(\mathbf{k}_{\|}, x_3 = 0, \omega)$ and displacement field u at the interface, and

$$\sigma^{-}_{\ell 3}(\mathbf{k}_{\|}, x_3 = -h, \omega) = -\delta_{\ell 3} \tag{5.3}$$

at the surface. The negative sign in equation (5.3) has to do with the fact that the surface tractions are in reaction to the applied force, which is periodic in time and position.

In both the substrate and the film, the displacement field is required to satisfy the equations of motion for a homogeneous elastic continuum

$$\rho \frac{\partial^2 u_i}{\partial t^2} = C_{ijk\ell} \frac{\partial^2 u_\ell}{\partial x_j \partial x_k} \tag{5.4}$$

where $u_i$ are the displacement components and $C_{ijk\ell}$ and $\rho$ are respectively the stiffness tensor and mass density of the individual media. The usual convention regarding summation over repeated subscripts is implied here.

For each value of $\mathbf{k}_{\|}$ and $\omega$, equation (5.4) admits six plane wave solutions for which the third component $k_3^{(n)}$, $n = 1, 2, ..., 6$, of k is obtained as a real or complex root of the characteristic sextic equation (see section 3.1.1)

$$\left| C_{ijk\ell} k_j k_k - \rho \omega^2 \delta_{i\ell} \right| = 0. \tag{5.5}$$

For the film, we retain all six solutions $k_3^{(n)}$, $n = 1, 2, ..., 6$, while for the substrate we retain only the 3 outgoing waves, which we enumerate $k_3^{(n)}$, $n = 7, 8, 9$, and discard the 3 incoming waves [46]. The outgoing waves are either homogeneous, i.e. $k_3^{(n)}$ real, with ray vector $\nabla_{\mathbf{k}} \omega(\mathbf{k})$ directed into the interior of the substrate, or evanescent with $Im(k_3^{(n)}) > 0$, so that they decay into the interior.

The required solution that satisfies the boundary conditions takes the form of a superposition of the 6 plane waves ($n = 1, 2, ..., 6$) in the film occupying the region $-h < x_3 < 0$

$$u_i^-(\mathbf{k}_{\|}, x_3, \omega) = \sum_{n=1}^{6} A_3^{(n)} U_i^{(n)} e^{ik_3^{(n)} x_3} \tag{5.6}$$

and of the 3 outgoing plane waves ($n = 7, 8, 9$) in the substrate occupying upper half space ($+, x_3 > 0$)

$$u_i^+(\mathbf{k}_{\|}, x_3, \omega) = \sum_{n=7}^{9} A_3^{(n)} U_i^{(n)} e^{ik_3^{(n)} x_3}. \tag{5.7}$$

From the stress-strain relationship, $\sigma_{lm} = C_{lmpq} \partial u_p / \partial x_q$ for the film and equation (5.6) it follows that the surface tractions are given by

$$\sigma_{\ell 3}^-(\mathbf{k}_{\|}, x_3 = -h, \omega) = i\omega \sum_{n=1}^{6} A_3^{(n)} B_\ell^{(n)}, \tag{5.8}$$

where

$$B_\ell^{(n)} = \sum_{pq} C_{3\ell pq}^- U_p^{(n)} k_q^{(n)} \exp^{-ik_3^{(n)} h} / \omega, \qquad n = 1, 2, ..., 6, \quad \ell = 1, 2, 3, \tag{5.9}$$

with

$$B_\ell^{(n)} = 0, \qquad n = 7, 8, 9, \quad \ell = 1, 2, 3. \tag{5.10}$$

Comparing Eqs. (5.3) and (5.8), we obtain a set of 3 linear equations for the partial wave amplitudes $A_3^{(n)}$

$$\sum_{n=1}^{9} B_\ell^{(n)} A_3^{(n)} = i\delta_{\ell 3} / \omega, \qquad \ell = 1, 2, 3. \tag{5.11}$$

Another three equations for the amplitudes are obtained from the boundary conditions of continuity of stress at the interface

$$\sigma_{j3}^{+}(\mathbf{k}_{\parallel}, x_3 = 0_+, \omega) - \sigma_{j3}^{-}(\mathbf{k}_{\parallel}, x_3 = 0_-, \omega) = 0, \tag{5.12}$$

which yield

$$\sum_{n=1}^{9} B_{\ell}^{(n)} A_3^{(n)} = 0, \qquad \ell = 4,5,6, \tag{5.13}$$

where

$$B_{\ell}^{(n)} = \sum_{pq} C_{3\ell-3pq}^{+} U_p^{(n)} k_q^{(n)}/\omega, \qquad n = 7,8,9, \quad \ell = 4,5,6, \tag{5.14}$$

and

$$B_{\ell}^{(n)} = -\sum_{pq} C_{3\ell-3pq}^{-} U_p^{(n)} k_q^{(n)}/\omega, \qquad n = 1,2,...,6, \quad \ell = 4,5,6. \tag{5.15}$$

Finally there are three equations for the partial wave amplitudes arising from continuity of the displacement field at the interface, i.e.

$$u_i^{+}(\mathbf{k}_{\parallel}, x_3 = 0_+, \omega) - u_i^{-}(\mathbf{k}_{\parallel}, x_3 = 0_-, \omega) = 0, \tag{5.16}$$

which yield

$$\sum_{n=1}^{9} B_{\ell}^{(n)} A_3^{(n)} = 0, \qquad \ell = 7,8,9, \tag{5.17}$$

where

$$B_{\ell}^{(n)} = U_{\ell-6}^{(n)}, \qquad n = 7,8,9, \ \ell = 7,8,9, \tag{5.18}$$

and

$$B_{\ell}^{(n)} = -U_{\ell-6}^{(n)}, \qquad n = 1,2,...,6, \ \ell = 7,8,9. \tag{5.19}$$

The solution of the nine equations comprising Eqs. (5.11), (5.13) and (5.17) takes the form

$$A_3^{(n)} = \frac{i}{\omega}(\mathbf{B}^{-1})_3^{(n)} \tag{5.20}$$

By substituting these results for $A_3^{(n)}$ into equation (5.6), we obtain the displacement Green's function $G_{33}(\mathbf{k}_\parallel,\omega) = u_i^-(\mathbf{k}_\parallel, x_3 = -h, \omega)$ at the surface

$$G_{33}(\mathbf{k}_\parallel,\omega) = \sum_{n=1}^{6} \frac{i}{\omega}(\mathbf{B}^{-1})_3^{(n)} U_3^{(n)} \exp^{-ik_3^{(n)}h}. \tag{5.21}$$

For given $\mathbf{k}_\parallel$, $\mathrm{Im}\{G_{33}(\mathbf{k}_\parallel, \omega+i0)\}$ and hence the Brillouin spectrum $I(\omega)$ consists of a continuum extending from a threshold frequency $\omega_0$, corresponding to the transonic state, to higher frequencies. This is known as the Lamb shoulder and represents the contribution of bulk waves to the light scattering. In addition, there may be one or more sharp lines at frequencies below $\omega_0$ which correspond to the excitation of surface waves. These occur where $\mathbf{B}^{-1}$ becomes singular, which is determined by the vanishing of $|\mathbf{B}|$. A Rayleigh wave is usually to be found on a free surface, and a soft film can have the effect of drawing out additional surface waves from the Lamb shoulder, i.e. Sezawa waves which are derived from Lamb waves in the film and Love waves which are derived from the shear horizontal (SH) waves in the film.

A hard film has the opposite effect of driving the Rayleigh wave into the Lamb shoulder. In the Lamb shoulder, there may be pronounced resonances which are generally associated with $|\mathbf{B}|$ being small but non-zero, and which can be identified as pseudo-SAW or pseudo-Love waves. However, the factors $U_3^{(n)}$ in equation (5.21) can have a significant modifying effect, and result in marked features in the scattering even where $|\mathbf{B}|$ is not a minimum. For large film thicknesses the Green's function for the film surface resembles the Green's function for a half-space of film material, except that the Lamb shoulder is fragmented into a large number of closely spaced resonances.

## 5.3 Numerical Results for a Hard Film

Because of its relatively high elastic moduli, a hard film has a stiffening effect on the surface wave velocity of the substrate. A stiffening system usually refers to the case where the shear bulk velocity of the film is higher than that of the substrate. In order to investigate in detail what acoustic modes there are and how the acoustic modes transform from one kind to another in this type of system, we present here the calculated Brillouin scattering spectra for some typical film thicknesses and the dispersion curves over a large range of $k_{\|}h$ for $TiN/HSS$. The effects of the TiN elastic moduli on the dispersion curves are also discussed.

### 5.3.1 Acoustic Behavior for a Strong Stiffening System

#### Guided Acoustic Modes for $TiN/HSS$

The elastic constants we start with in our calculations on $TiN/HSS$ are the same as those used in section 4.1.4. The calculated spectra, with light incident at an angle of 70° to the sample surface normal, for some typical thicknesses of films are shown in figure (5.2). Starting with film thickness $10nm$, there is a sharp peak at 10.9 GHz, corresponding to a true surface wave, together with the bulk continuum (Lamb shoulder) extending from the substrate transverse wave threshold (at 11.4 GHz) and through the longitudinal wave threshold (at 21.3 $GHz$) to higher frequencies. By $40nm$ the surface wave has merged into the Lamb shoulder. A highly damped p-SAW in the form of a broad band is evident at $60nm$, and for 150, 200 and $240nm$, we see the emergence and rise to prominence of the "pre-Rayleigh" mode, and then

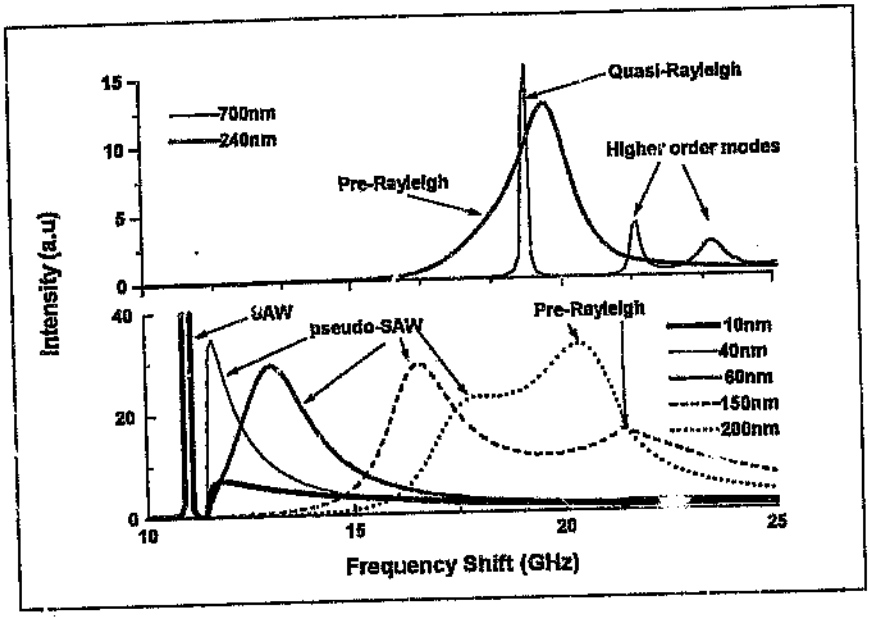


Figure 5.2: Calculated Brillouin spectra of $TiN/HSS$ for a selection of film thicknesses $h$, displaying a true SAW , a highly damped p-SAW, "pre-Rayleigh", quasi-Rayleigh and its higher order modes. In the calculations, $k_{||}$ is fixed by the back scattering geometry with the incident angle $\theta_i = 70°$ . The scattering intensity is given in arbitrary units.

its evolution into the "quasi-Rayleigh" wave by $700nm$. For $700nm$, in addition to the quasi-Rayleigh mode, its higher order modes are also in evidence. The higher order modes have larger frequency shifts and display relatively lower scattering intensity than the p-SAW. For even larger film thicknesses, the higher order modes become closely spaced resonances that cannot be resolved by Brillouin scattering.

**Dispersion Relations of $TiN/HSS$**

An overall view of the acoustic behavior of $TiN/HSS$ is provided by the calculated dispersion relation in Figure (5.3), representing the wave velocity $v$ vs. $k_{\|}h$, where $k_{\|}$ is the magnitude of $\mathbf{k}_{\|}$. As can be seen for this stiffening system, with increasing film thickness or $k_{\|}h$, the SAW velocity of $TiN/HSS$ increases from the Rayleigh wave velocity of the substrate $HSS$ eventually to the quasi-Rayleigh wave velocity of the $TiN/HSS$.

In figure (5.3), initially, in the region $0 < k_{\|}h < 0.8$, there is a steady increase in $v$, which levels off to the substrate bulk shear velocity ($v_{st}$) at $k_{\|}h = 0.8$ . In this region the surface mode is a true SAW, with the partial waves in the substrate falling off exponentially away from the surface, and $|\mathbf{B}|$ vanishing exactly. For $k_{\|}h$ between one and about eight, one of the partial waves in the substrate is a bulk wave which carries the energy of the surface mode away from the surface, and $|\mathbf{B}|$ does not vanish but instead displays a rather shallow minimum. This mode can be regarded as a highly damped p-SAW. For $k_{\|}h$ greater than about eight, the surface mode is still a p-SAW, but evolves into the Rayleigh wave for $TiN$ at larger $k_{\|}h$, and with $|\mathbf{B}|$ having a sharp but non-zero minimum. The higher order p-SAW modes are discussed later.

It can be seen that the above dispersion curves are very similar to that discussed in section 4.2.4 by a "classical" method. However, this method can provide more information for the region of the discontinuity and higher order acoustic modes. This is because this method which is based on the ripple scattering mechanism, takes into

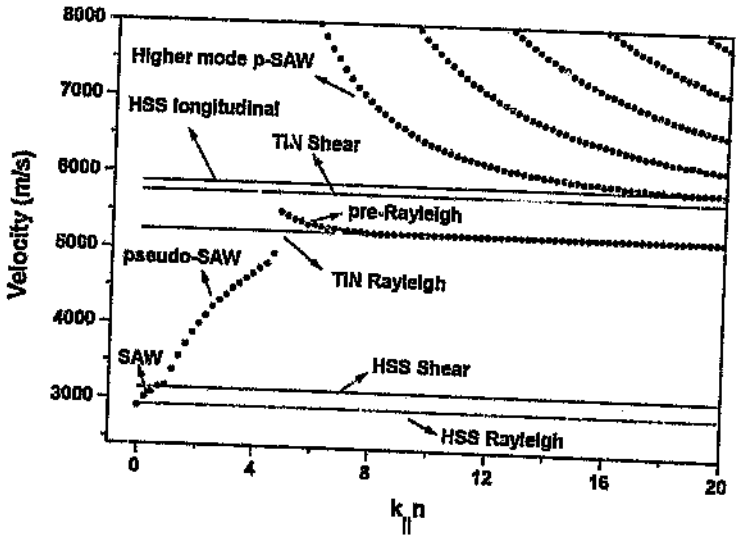


Figure 5.3: Dispersion curves of $TiN/HSS$ for various guided acoustic modes calculated using the elastic moduli of bulk $TiN$. The "pre-Rayleigh" mode emerges at the discontinuity. The shear velocity of $TiN$ is 1.83 times that of $HSS$, so that $TiN/HSS$ represents a strong stiffening system. $k_{\|}h$ is the product of surface phonon wavevector and film thickness.

account the contributions from all the possible acoustic excitations localized at the free surface.

The existence the p-SAW and its higher modes included in the figure (5.3) is confirmed by our measurements in next chapter. We calculate here the Brillouin spectrum with only ripple scattering at the free surface being taken into account. For $TiN$ films, we consider that it is a reasonable approximation to ignore the elasto-optic scattering because the scattering volume concerned is small.

The dispersion relation described above applies to the strongly stiffened situation. The fact is that the elastic constants of $TiN$ used in the calculations have a profound affect on the dispersion relation. The discontinuity in the dispersion curve near $k_{\|}h \approx 4.6$ disappears if reduced values of the elastic constants of $TiN$ are used. This is shown in the following section, where no "pre-Rayleigh" mode appears, and the highly damped p-SAW transforms directly into the quasi-Rayleigh wave of the $TiN$ film at large $k_{\|}h$.

### 5.3.2 Acoustic Behavior for a Weakly Stiffened System

We use the reduced elastic moduli of $TiN$ that are about 25% smaller than its bulk values to describe the weak stiffening system. The reduced elastic moduli decreases the shear bulk velocity of the film, but it is still higher than that of the substrate. The calculated Brillouin scattering spectra, also with the laser light incident angle to sample surface normal being 70°, for this system is shown in figure (5.4). Comparison between figure (5.2) and figure (5.4) shows that no pre-Rayleigh mode appears for the

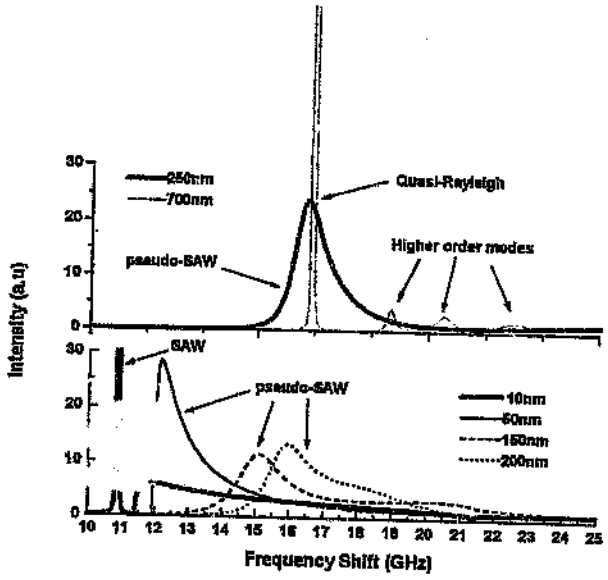


Figure 5.4: Calculated Brillouin spectra of a weakly stiffened system for some typical film thicknesses using the reduced values of the elastic moduli which are 25% smaller than those of bulk $TiN$, where no pre-Rayleigh mode is found. In the calculations, $k_{\|}$ is fixed by the back scattering geometry with the incident angle $\theta_i = 70°$ . The scattering intensity is given in arbitrary units.

system. Instead, the p-SAW increases in phase velocity (frequency shift) to approach the quasi-Rayleigh wave as the film thickness increases.

The dispersion relation for the weakly stiffened system is shown in figure (5.5). As $k_{\|}h$ increases, the phase velocity of the p-SAW continuously increases and evolves into the quasi-Rayleigh velocity of the film at large values of $k_{\|}h$. There does not exist a pre-Rayleigh mode before the p-SAW transfers into quasi-Rayleigh mode.

As the elastic moduli of the film decrease further but remain higher than those of the substrate, the dispersion relation is similar to the figure (5.5). In this further reduced stiffening system, the dispersion curves of p-SAW and quasi-Rayleigh move downwards to lower velocity and there are more higher order modes appearing for a particular $k_{\|}h$. For the system, where the elastic moduli of the film is less than those of the substrate, there exist Sezawa and pseudo-Sezawa waves which is beyond the scope of this thesis.

### 5.3.3 Effects of Material Constants on the Acoustic Behaviour in a Stiffening System

In contrast to varying the elastic constants of the film, the variations of the elastic moduli of the substrate have the opposite effect on the dispersion relation of a stiffening system. As the elastic moduli of the substrate increases, the discontinuity of p-SAW and hence pre-Rayleigh mode will disappear, while the quasi-Rayleigh velocity of the film remains constant over the range of large $k_{\|}h$. Because the bulk shear velocity depends on both the elastic constants and mass density of materials, the variations of the densities of the film and substrate have also an effect on the dispersion relations of a supported film. Increasing of the film density has the same effect as reduction of the elastic moduli of the film, for example.

In this chapter, we have outlined a general theory of surface Brillouin scattering and the scattering mechanisms. Emphasis has been given to Brillouin scattering from a supported hard film. Surface Brillouin scattering spectra and dispersion relations

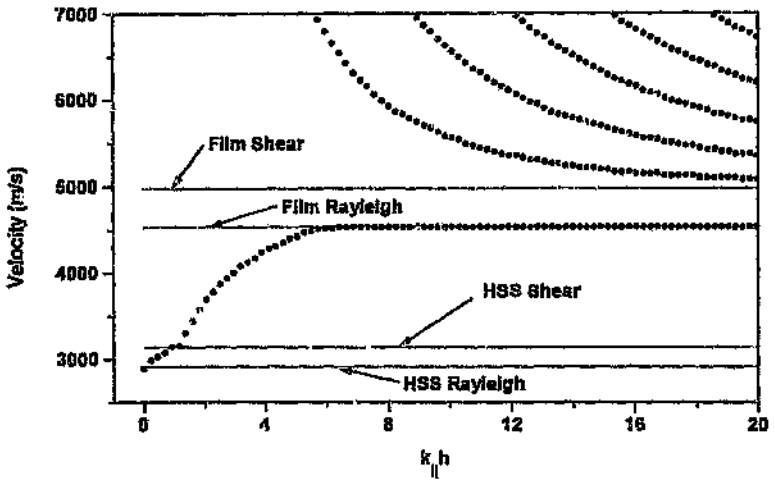


Figure 5.5: Calculated dispersion curves of a weak stiffening system, where no discontinuity of p-SAW is found. The "film" in the calculations is an assumed film of which elastic constants equal to 75% of $TiN$ bulk values. The shear velocity of the "film" is 1.58 times that of $HSS$, so that this system represents a relatively weak stiffening system.

have been calculated for a strong and a weak stiffening system using a Green's function method based on a ripple scattering mechanism, and a pre-Rayleigh mode has been identified. The algorithm of the calculations using this method has been described in detail. We have also investigated how the elastic moduli and density of the film and the substrate affect the dispersion relation.

# Chapter 6

# Experimental Techniques in Brillouin Scattering

In the past decade, considerable progress has been made in the development of surface Brillouin scattering (BS) as a technique for the non-destructive characterization of materials. With the advent of high resolution and high contrast multi-pass tandem Fabry-Perot interferometry, BS has been applied to the measurement of the near-surface elastic properties affected by radiation damage, ion-implantation and ion exchange, mechanical polishing and other surface modifications, thin supported films and interfaces at both ambient and high temperatures, making use of various guided and localized acoustic modes including Rayleigh waves, pseudo-surface acoustic waves (p-SAW), Sezawa waves and Stoneley waves. The use of conventional ultrasonic techniques in these situations is difficult because of the large wave length in relation to the layer thickness. Brillouin scattering is also a valuable technique for the characterization of materials at high temperatures and pressures.

In this chapter, the kinematics of Brillouin scattering from surface phonons are introduced in section 1. In section 2, the tandem Fabry-Perot interferometry, surface Brillouin scattering setup, measuring method and calibration and analysis of the experimental data are described. The back-scattering geometry adopted in our measurements and some crucial factors for successful measurements on $TiN/HSS$ are discussed.

## 6.1 Kinematics of Brillouin Scattering in Solids

The interaction between light and acoustic excitations in solids was investigated first by Brillouin (1922) and Mandelshtam (... 26) early in the century. Brillouin spectroscopy studies inelastic scattering of light by thermally excited acoustic phonons (long-wavelength thermal acoustic modes) in a solid. The dynamics of these excitations are reflected in the spectrum and polarization of the scattered light. Since the dynamics are determined by the elastic properties of the scattering materials, the phase velocity of acoustic modes and thereby elastic constants can be obtained from the spectrum. Brillouin scattering is thus a non-contact and a non-destructive method for measuring the elastic properties of solids. The incident light, usually focused laser beam, and the scattered light leave the sample essentially in thermodynamic equilibrium. Unlike ultrasonic techniques, no external forces are applied.

From quantum mechanics, for energy and momentum conservation, first order light scattering is described in terms of the creation and annihilation of phonons of wavevector $k$ and angular frequency $\Omega$. Scattered light of wave vector $k^s$ and angular

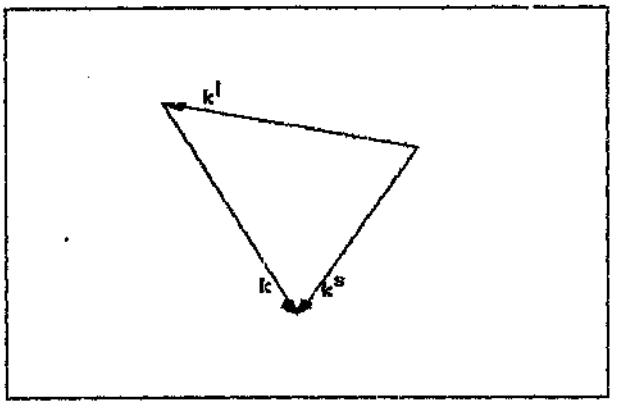


Figure 6.1: Wavevector conservation of the incident and scattered light: $k^s - k^i = k$.

frequency $\omega_s$ is linked to the incident light (with wave vector $k^i$ and frequency $\omega_i$) as follows:

$$\mathbf{k}^s - \mathbf{k}^i = \pm\mathbf{k} \tag{6.1}$$

$$\omega_s - \omega_i = \pm\Omega \tag{6.2}$$

where + sign refers to absorption of phonons (anti-Stokes event) and the - sign to the emission of phonons (Stokes event). The phonon angular frequencies probed in condensed matter by Brillouin scattering are in the hypersonic regime :

$$10^7 s^{-1} < |\Omega| < 10^{12} s^{-1} \tag{6.3}$$

which happens to lie between the angular frequencies measured by ultrasonics and by neutron scattering. Because of the low values of $\Omega$ and the sound velocity compared to those of the incident light, the frequencies of the incident and scattered light are approximately equal and so are the magnitudes of their wave vectors (i.e. $k^s \approx k^i$).

With the above approximation, wave vector superposition triangle in figure (6.1) shows that the magnitude of the phonon wave vector is given by

$$k = 2k^i \sin(\theta/2) \tag{6.4}$$

where $\theta$ is the scattering angle, i.e. the angle between $\mathbf{k}^s$ and $\mathbf{k}^i$. In solids the corresponding wavelength $(2\pi/k)$ is many times longer than the distance between adjacent atoms. In this long wavelength limit, the magnitude of phase velocity ($v = \Omega/k$) is within the hypersonic sound velocity region.

The angular frequency shifts $(\omega_s - \omega_i)$ are measured in the Brillouin scattering spectrum and are related to the scattering vector by

$$\omega_s - \omega_i = 2k^i \sin(\theta/2)v. \tag{6.5}$$

Since the $k^i$ and $\theta$ in these formulae are determined by the experimental arrangement for a specific scattering geometry, the phase velocity can be obtained using the measured angular frequency shifts $(\omega_s - \omega_i)$. The phase velocity depends on the density and elastic constants of the solid. Thus, the elastic constants of materials may be determined using Brillouin scattering.

## 6.2 Experimental Techniques

Brillouin scattering is the very weak inelastic scattering from thermally excited phonons superposed on much stronger elastic scattering. A typical Brillouin scattering experiment measures phonons with frequencies in the range up to about 150 $GHz$. For an opaque material, where the scattering from acoustic excitations at or near the

surface, the measured frequencies are usually in the range of $20 - 40\ GHz$, and the elastic component from surface roughness and irregularities exceeds the intensity of the inelastic component by more than a factor of $10^4 - 10^5$ in the scattered light. Thus the Brillouin peak is impossible to pick up by normal scanning Fabry-Perot interferometry with a contrast

$$c = 1 + \frac{4F^2}{\pi^2} \leq 10^4,$$

where the contrast $c$ is the ratio of maximum to minimum transmission and $F$ ($\leq 100$) is the finesse depending on the mirror reflectivity, mirror flatness and instrument aperture.

In order to detect the scattering from surface acoustic modes of the hard films on a tool steel substrate, much higher contrast and higher resolution is required. The tandem multi-pass interferometer meets this requirement.

### 6.2.1 Tandem Fabry-Perot Interferometry in Brillouin Scattering

The Fabry-Perot (FP) Interferometer consists of two plane mirrors mounted accurately parallel to each another. For a given optical spacing $L_1$ between the two mirrors, only wavelengths satisfying

$$\lambda = \frac{2L_1}{m} \tag{6.6}$$

will be transmitted, where $m$ is integral values. In other words the FP interferometer acts as a tunable filter whose peak transmission is close to unity over a narrow spectral

interval, falling to a very low value outside this interval. The FP interferometer is used in Brillouin scattering spectroscopy by varying $L_1$ so as to scan the scattered light intensity at different wavelengths. However the measured intensity for a given spacing is the sum of the signals at all wavelengths satisfying equation (6.6). In order to ensure the measured peaks to be collected from the light scattered by acoustic excitations with a specific wavelength, the spectrum of the scattered light must lie entirely within a wavelength spread $\Delta\lambda$, where $\Delta\lambda$ is the spacing between successive transmitted wavelengths which is known as the free spectral range (FSR).

The use of two or more FP interferometers of unequal mirror spacing in series (tandem interferometer) can increase the $\Delta\lambda$ at a fixed resolution. If the spacing of the second interferometer $L_2$ is close to $L_1$ (for instance, in our measurements $L_2/L_1 = 0.95$), the FSR of this tandem system will increase by a factor of 20 over that of a single interferometer. This is because that only when $\lambda_1 = \lambda_2$, i. e.

$$\frac{2L_1}{m_1} = \frac{2L_2}{m_2} \qquad \text{or} \qquad m_2 = 0.95m_1 \tag{6.7}$$

will the scattered light transmit through both of the FP interferometers. From equation (6.7), the smallest integral value of $m_1$ is 20. This implies that light is transmitted through both of the interferometers only after 20 times the FSR of the first interferometer, eliminating the problem of the overlapping of interference orders from a spectrum of scattered light. Since the transmission of either interferometer never falls exactly to zero, small ghosts of the intervening transmission peaks remain as much suppressed orders, as shown in figure (6.2).

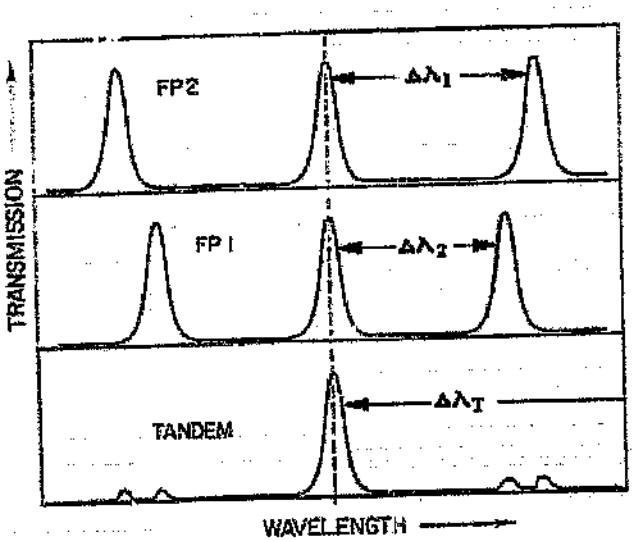


Figure 6.2: Free spectral range for tandem interferometer, $\Delta\lambda_1$ and $\Delta\lambda_2$ are the FSRs of mirror pairs 1 and 2. $\Delta\lambda_T$ is the 20 times increased FSR of the tandem interferometer based on $L_2 = 0.95L_1$.

In practice, the use of tandem interferometry has been limited due to the difficulty in the synchronization of the two interferometer scans. During the scan with a few Å accuracy, the relation

$$\frac{\delta L_1}{L_1} = \frac{\delta L_2}{L_2} \tag{6.8}$$

must be satisfied, where $\delta L_1$ and $\delta L_2$ are the increments in the mirror spacing $L_1$ and $L_2$. In our experiment, a synchronously scanning tandem interferometer is achieved by mounting the scanning mirrors of the two interferometers on a single scanning stage [77], one with the mirror axis parallel to the scan direction, and the other with its axis making an angle $\alpha$ to the direction of scanning as illustrated in figure (6.3). In this case,

$$L_2 = L_1 \cos\alpha \tag{6.9}$$

can be maintained and equation (6.8) satisfied. In our measurements, $\alpha \approx 18°$ and $L_2/L_1 = 0.95$.

Another advantage of this tandem interferometer is that it is much less sensitive to temperature fluctuations since the two interferometers are mounted very close to each other, sharing the same environment. A tilt-free scanning stage consisting of a deformable parallelogram platform mounted on top of a roller translation stage for fine and coarse scanning. The translation stage is mounted on a dynamic isolation system with excellent directional and positional stability using an electronic feedback control, and then on top of an active vibration isolation table. This is necessary since any external influence which distorts the mirror spacing by more than a few angstroms will seriously distort the spectrum. In order to scan a FP interferometer through a

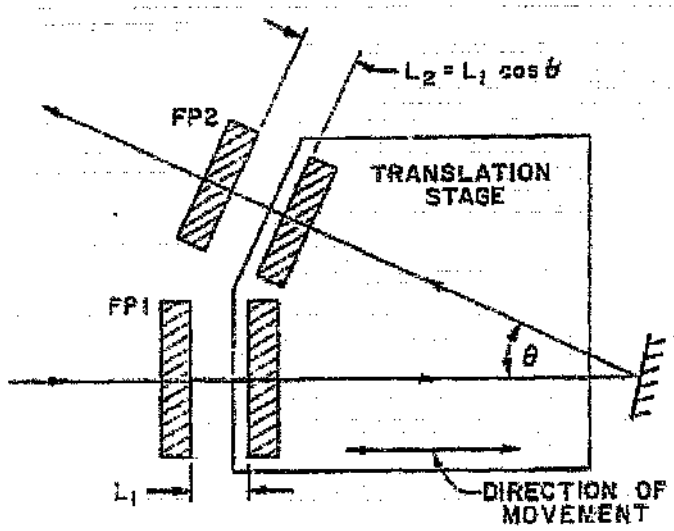


Figure 6.3: The translation stage of the tandem interferometer used in the experiments. The two interferometers are synchronized automatically by the translation stage when the mirror spacing is scanned in the measurements (from Ref. [78]).

single transmission peak a change in mirror spacing of about 25Å is required.

In measurements the mirror spacing is scanned rapidly, and the interferometer transmission thereby tuned to analyze spectral features of the incident light. A multichannel storage device is used to sum the spectrum over successive scans. While the scanning is performed, the interferometer must maintain dimensional stability to within a few Å, which can be achieved by making continuous corrections to the mirror spacing and parallelism using piezoelectric transducers. The mirror spacing is measured by a plane capacitor, and an active loop is used for regulating the scan

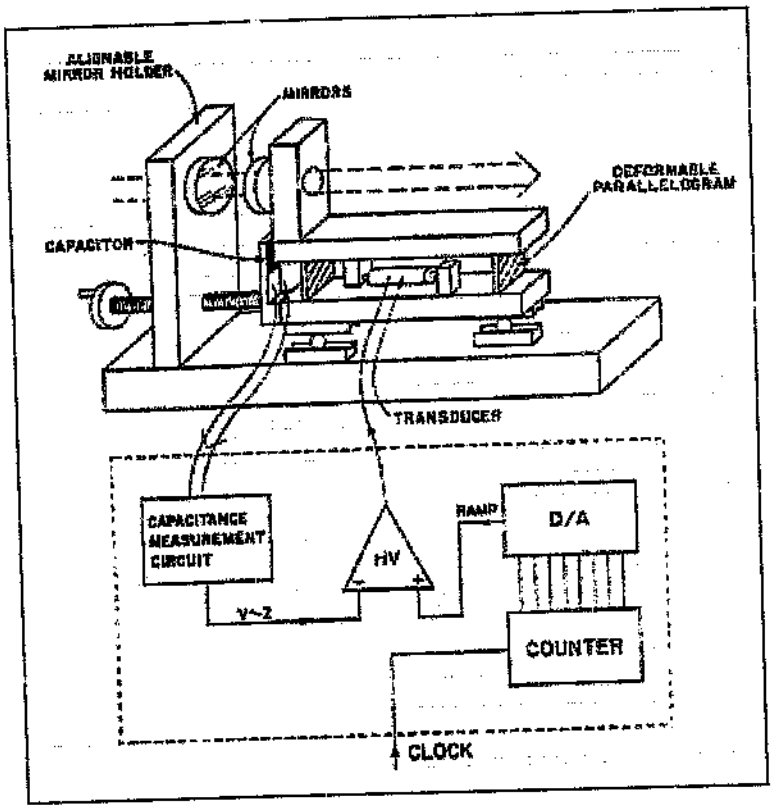


Figure 6.4: A schematic diagram of a tandem interferometer (from Ref. [78]).

voltage to the transducer. The parallel interferometer is extremely sensitive to mirror misalignment, and an active feedback loop must be used to regulate the parallelism of the mirrors. The construction of the scanning stage and interferometer is shown schematically in figure (6.4). The instrument is entirely enclosed in an aluminium box to protect the interferometer from sound waves from the outside, which can excite high-frequency resonances in the system.

The contrast of an interferometer can be greatly enhanced by placing two or more

interferometers in series or by passing the light two or more times through the same interferometer. In practice, the latter is usually adopted in order to avoid the problem of synchronization. In our experiment, we use a Sandercock (3 + 3) pass tandem interferometer, which has two interferometers in series and can achieve a contrast of greater than $10^{12}$, five or six orders of magnitude greater than that of a single interferometer. The design of a multi-pass interferometer has been discussed in detail in the literature [78] and [79]. The advent of this multi-pass tandem interferometer makes Brillouin scattering measurements of opaque materials possible.

### 6.2.2 Surface Brillouin Scattering Setup

The experimental setup incorporating Sandercock's (3+3) pass tandem interferometer that has been used in the measurements is shown in figure (6.5). An argon-ion laser beam with a wavelength of 514.5$nm$, is guided by a series of reflecting mirrors, and focused onto the sample's top surface by a 50 $mm$ focal length lens. With the back-scattering geometry, this lens also serves to collect the scattered light which is then guided into the tandem interferometer for processing by another series of mirrors. The interferometer works as a tunable optical filter for the spectral features in the light scattered from the samples. The scanning and stabilization of the interferometer is controlled by a control unit aided by a double beam oscilloscope. The scattered light passes the interferometer mirrors 6 times and the contrast is increased to a very high order to distinguish the weak inelastic scattering signals from those of the strong elastic scattering.

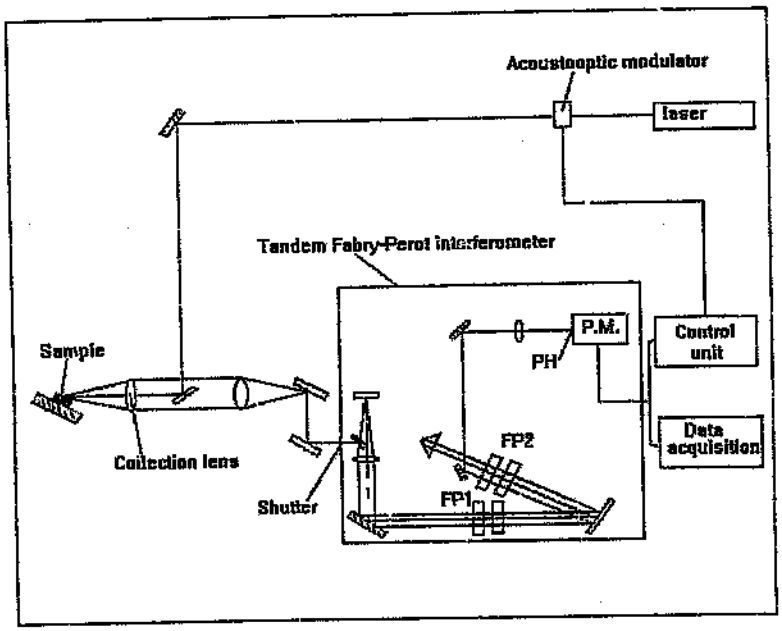


Figure 6.5: Experimental arrangement for Brillouin scattering measurements with a back-scattering geometry.

The filtered light is collected through an aperture and then enters the photo-multiplier tube (PMT) with overall sensitivity ratings $5000 A/lm$. The tube cathode is cooled by a thermoelectric refrigerated (TR) chamber to reduce the noise level. The cooling temperature of the TR was set at $-20°C$. The small signals from the PMT are amplified by a preamplifier with fast rise time and having low noise. The amplified signals are processed by gated photon-counter operating at rates up to 200 $MHz$, and then are reshaped and delayed by a logic shaper & delay (LSD) to provide suitable logical interface capability. The sequence of electric pulses from the LSD is stored in a PCA-II card, which consists of a 100 $MHz$ analogue to digital converter (ADC), single channel analyzer (SCA), multichannel Scaler (MCS) and on board memory. With this card and standard software installed in a personal computer, the computer can be used as a fully featured multichannel analyzer [illegible], with window style pull down menus for operational convenience. The BS [illegible] are collected and plotted by this computer.

An acousto-optic modulator with a shutter controlled by the scanning signal (appropriate windows set by the control unit) is used to attenuate or filter out the intensity of the elastically scattered peak in order to protect the photo-multiplier tube. In the absence of an elastically scattered peak from the sample, a supplementary weak and constant signal at the laser frequency is provided by a beam-splitter and fibre-optical cable. This is necessary to provide a reference signal for the stabilization of the interferometer scan and parallelism of the mirrors.

The details of the apparatus used in the experiment are listed in table 6.1.

| Items | Model | Manufacturer |
|---|---|---|
| Fabry-Perot Interferometer | Tandem | JRS |
| Vibration Isolation System | MOD-2 | JRS |
| Interferometer Control Unit | Attach. to TFP | JRS |
| Double Beam Oscilloscope | PM3230 | Philips |
| Argon Ion Laser | 2020 | Spectra-Physics |
| Acousto-optic modulater | ADM-40 | IntraAction Corp. |
| Photomultiplier Tubes | 9863Q/R464S | EMI Electronics Ltd. /Hamamatsu |
| Thermo Refrigerated Chambers | TE-104TS-RF | Products for Research, Inc. |
| Fast Preamplifier | SR445 | Stanford Reasearch Systems, Inc. |
| Gated Photo Counter | SR400 | Stanford Reasearch Systems, Inc |
| Logic Shaper & Delay | 2055 | Canberra Industries, Inc. |
| Multichannel Analyzer | PCA-II | The Nucleus, Inc. |
| Personal Computer | AT | IBM |

Table 6.1: Apparatus used in the experimental arrangement.

### 6.2.3 Measuring Method

The multi-pass tandem interferometers must be pre-aligned to be parallel and with correct relative spacing in the reflection mode before the Brillouin scattering measurements is taken. This can be done by measuring the doubly reflected beam from the two interferometers using a photomultiplier aided by a double beam oscilloscope. With the incident light passing through a beam-splitter, it is guided onto the first interferometer and reflected via a second beam-splitter onto the other interferometer, and then reflected and directed to the photomultiplier. The pre-alignment method based on the fact when an interferometer is transmitting, the reflected light intensity tends towards zero. In other words, a minimum is observed in the oscilloscope when one of the interferometers is optimally aligned. When the interferometer scans, the photomultiplier signal will, therefore, show a background intensity punctuated by two distinct series of minimum peaks (near zero intensity) after the two interferometers are independently optimally aligned. The fact that there are only two series of minima in scanning because the reflected light is almost monochromatic since the elastically scattered light dominates over the inelastically scattered light. A series of minima can be observed due to the fact that the relative spacing of the two interferometers does not conform to equation (6.9), and the interferometers are not in the tandem mode. Further adjustment is needed to bring a pair of peaks into coincidence for the correct relative spacing, and then the pre-alignment of the tandem interferometer is complete. On switching the optical system back to the multi-pass tandem mode, transmission of elastically scattered light will be observed with only minor adjustments necessary to

maximize the transmission. Switching on the acousto-optic modulator to attenuate the elastic central peaks while the "ghosts" is kept at a lower level, the measurements of Brillouin scattering can be started.

For scattering from surface acoustic modes, conservation of wavevector parallel to the surface holds, i.e.

$$k_{||} = k_i \sin\theta_i + k_s < \sin\theta_s >, \tag{6.10}$$

where $k_{||}$ is the surface phonon wavevector, $k_i$ and $k_s$ are the modulus of the wavevectors of the incident light and the scattering light respectively. $\theta_i$ is the incident angle with respect to the surface normal. $\theta_s$ is a range of scattering angles depending on the finite aperture of collection lens and $\langle \sin\theta_s \rangle$ is the average of $\sin\theta_s$ over the range from $\theta_i$-$\Delta\theta$ to $\theta_i + \Delta\theta$. For $\theta_i = 70°$ and collection lens of diameter $D = 27.8mm$ and focal length $F = 50mm$ in our measurements, $\Delta\theta = D/2F \approx 15.5°$, and

$$\langle \sin\theta_s \rangle = \frac{\int_{\theta_i-\Delta\theta}^{\theta_i+\Delta\theta} \sin\theta d\theta}{\Delta\theta} = \frac{\sin\Delta\theta \sin\theta_i}{\Delta\theta} \approx 0.928. \tag{6.11}$$

In the $k_i \approx k_s$ approximation for Brillouin scattering and for back scattering geometry, the phase velocity $v$ of the thermally excited phonons that engage in the scattering is

$$v = \frac{\lambda_i f}{(\sin\theta_i + \frac{\sin\Delta\theta \sin\theta_i}{\Delta\theta})}, \tag{6.12}$$

where $f$ is the frequency shift corresponding to the surface modes in the BS spectrum.

The highly polished sample was located on the sample holder which can be rotated for a chosen incidence angle. The incident angle of the laser beam with respect to the normal of the sample was kept fixed during a measurement. The incident light beam was of power $300 - 400mW$ and its $\vec{E}$ vector was polarized in the plane of incidence

in all cases. The observation was performed in air and at room temperature. The mirror spacing of TFP1 was chosen to be $4.000\,mm$, enabling the surface wave peak position to be clearly separated from the elastic scattered peak. A scan amplitude of 2.30 is used for data accumulation. "Windows" of the control unit are set to cover the elastic peak width and used to operate the modulator substantially reducing the intensity of elastic scattering.

In the experiments the sample surface condition and the optical alignment of the back-scattered light have a crucial effect on the successful measurement of spectra, and patience must be exercised with regard to the measurement period.

### 6.2.4 Calibration Procedure for a Measured Brillouin Spectrum

Data collected is stored in the MCA in a form of counts (intensity) as the vertical axis and number of channels as the horizontal axis. The number of channels can be converted into a frequency shift using the first ghost and the spacing of either of two mirrors ($L_1$ or $L_2$). A typical Brillouin scattering spectrum is sketched as figure (6.6), where the central peak is the elastic scattering signals and the other two peaks on each side are the first order "ghosts". From the positions of the ghosts ($X_1$ and $X_2$), it is possible obtain the calibrated frequency shift ($\omega$) per channel number, and hence the frequency shift of the Brillouin scattering peaks can be determined from their positions ($X_B$). Corresponding to the Brillouin peaks shown in figure (6.6), the

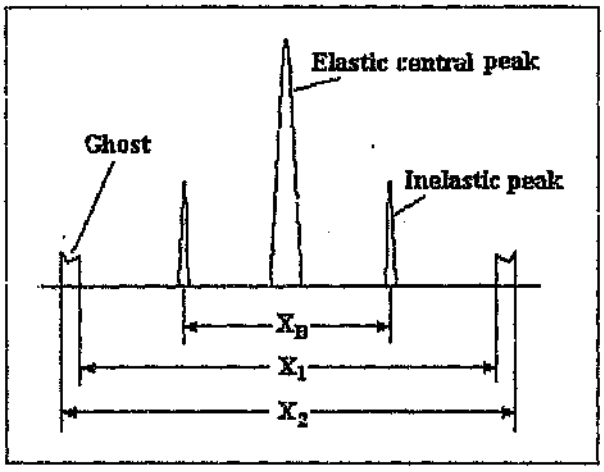


Figure 6.6: A schematic diagram for the description of the calibration procedure of measured Brillouin spectra.

frequency shift can be obtained using

$$\Delta f = (\frac{X_B}{2})\nu = (\frac{X_B}{2})(\frac{c}{2L_1X_1} + \frac{c}{2L_2X_1})$$

where $c$ is the speed of light and $L_2 = L_1 \cos\alpha$.

Some errors may be induced if the shape of the ghost is distorted so that $X_1$ and $X_2$ cannot be determined precisely. The broadening of the Brillouin peaks, which is not unusual in measurements, also makes the determination of $X_B$ difficult on occasion, and hence errors can occur.

# Chapter 7

# Sample Preparation and Analysis

In this chapter, sample preparation technique and physical properties of *TiN* films determined by various analytical techniques are discussed. Section 1 describes the deposition process of *TiN* films and sample preparation for Brillouin scattering. Section 2 consists of the investigation of the physical properties of the samples. The *TiN* films deposited using magnetron sputtering and hollow cathode discharge plating have a preferred orientation which is detected by X-ray diffraction. The topography and the thickness of the films are investigated using SEM, and the elemental composition of the films is probed using EDX-ray analysis. XPS is used to investigate the composition variations at the interface region. The film thickness is also confirmed by Rutherford backscattering measurements using the bulk values of density of TiN.

## 7.1 Samples of $TiN$ Films on $HSS$

The $TiN/HSS$ combination chosen for measurements is of practical significance since $HSS$ is the most widely used tool steel in industry. The cut substrates are slender bars of size of $25mm \times 8mm \times 8mm$. A notch is made at $10mm$ from one end in each bar for preparing fracture ons after coating. One face of the substrate is mechanically polished to a very high smoothness ($0.5\mu m$) using diamond powder. This is required not only to produce good adhesion at the interface but also for a good Brillouin spectrum. All substrates are ultrasonically cleaned with acetone and alcohol prior to being loaded into the deposition chamber.

$TiN$ hard films with various thicknesses are deposited on $HSS$ substrates using the DC magnetron sputtering apparatus at the Atomic Energy Corporation (AEC) of South Africa Limited. The purity grades of the materials involved are 99.9 $wt.\%$ of titanium, 99.997 $vol.\%$ of argon and 99.999 $vol.\%$ pure nitrogen. Three rectangular water cooled titanium targets are fixed around the cylindrical chamber inside. The substrate is located at a distance of $200mm$ from the targets and the polished face is kept upwards. Prior to deposition the system is evacuated with a rotary and a diffusion pump to a pressure around $10^{-5}$ $torr$ to eliminate oxygen, and the substrate is heated and sputter cleaned in an argon plasma under the pressure of $2 \times 10^{-3}$ $torr$.

The deposition process starts by introducing nitrogen into the chamber. Control of the flow of nitrogen enables the total chamber pressure ($Ar$ and $N_2$) to be $2.1 \times 10^{-3}$ $torr$. A substrate bias of $-70V$ is applied to all samples. Titanium nitride is deposited at a temperature of around $250°C$ with a deposition rate of 0.12

$\mu m$ $min^{-1}$ (see section 7.2). In order to have the samples deposited under exactly the same conditions, a rotational shutter system was designed and mounted inside the deposition chamber. After stable deposition conditions were achieved, a particular substrate was exposed for the deposition of $TiN$ by opening the shutter to that sample. With the deposition rate approximately 0.12 $\mu m$ $min^{-1}$, the film thicknesses were controlled by varying the period in which the shutter was open. The thicknesses of the $TiN$ films were subsequently confirmed using SEM (JSM - 840 Scanning Electron Microscope) on sample fracture sections, XPS depth profile measurements and Rutherford backscattering based on the bulk density of $TiN$.

Samples of the stressed $TiN_x$ films were deposited in an $Ar/N_2$ plasma on both mild steel and $HSS$ using a hollow cathode discharge ion plating technique. Various states of stress in $TiN_x$ films were obtained by altering the nitrogen partial pressure in the deposition precess from $6.7 \times 10^{-3}$ to $6.0 \times 10^{-1}$ $Pa$. For all the films the substrate temperature was kept at $500°C$ and the substrates were negatively biased at $-50V$. All the films in these measurements were $3.5\mu m$ thick, a typical thickness in tool coating applications. The $TiN_x$ films were analyzed using Auger spectroscopy and the nuclear reaction $^{15}N\ (p, \alpha\gamma)^{12}C$ by D Pietersen of the AEC, showing that the variation of nitrogen partial pressure does not significantly change the stoichiometry ($x$ in of $TiN_x$) of the films. The residual stresses of our $TiN_x$ films are measured through the variation of the lattice parameter, but the reason for these variations is not fully understood. It has been shown that the residual stress of $TiC$ films is affected by the film deposition rate and/or argon incorporation into the lattice [75].

For the Brillouin scattering measurements, the as-deposited face of the $TiN$ film

was mechanically polished to a flatness of $0.05\mu m$ using diamond and $Al_2O_3$ polishing powders. It was found that the surface quality of samples is crucial for the successful measurement of surface acoustic modes in the $TiN/HSS$ combination; smooth surfaces produce less elastic scattering of light which is necessary in order to detect the weak inelastic scattering peaks present in the spectrum.

## 7.2 Physical Properties of $TiN$ Films

### 7.2.1 Film Thickness

In order to obtain the dispersion relation for the $TiN/HSS$ combination, the thickness of a film must be known. With the above-mentioned deposition parameters, a $TiN$ film corresponding to 10 minutes deposition time was prepared. This sample was cooled down in liquid nitrogen for a few minutes and then knocked with a hammer to obtain a fracture section. The SEM photograph for this section is shown in figure (7.1). The layer on the right hand side in the micrograph is the $TiN$ film which has an obviously denser structure than the $HSS$ substrate. It can be seen in the micrograph that the thickness of the film is approximately $1200nm$. Therefore the deposition rate of $TiN$ film under the same deposition conditions can be regarded as $120nm\ \mathrm{min}^{-1}$. Thus, the film thickness can be fairly well controlled by varying the deposition time although the growth rate of a $TiN$ film is not strictly linearly proportional to this time.

The thickness of a film deposited in this way was further determined using an

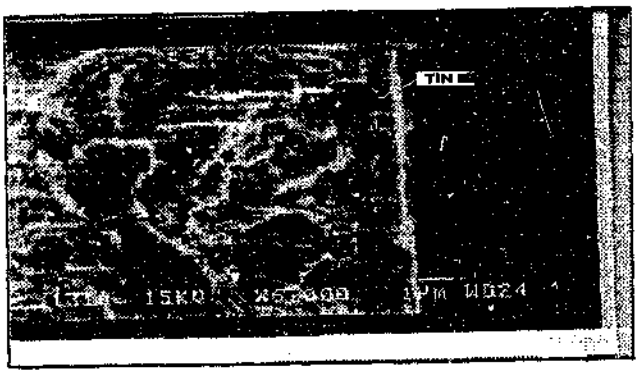


Figure 7.1: SEM fractograph of the $TiN/HSS$ deposited in 10 minutes using the parameters described in text. The layer at the right hand side is $TiN$.

SEM investigation of its fracture section. Figure (7.2) shows the micrograph of the $TiN$ film deposited in 2 minutes. As one can see the thickness of this film is indeed around $240nm$ in thickness. Since the film is not one hundred per cent uniform in thickness and because of some difficulty in obtaining a sharp micrograph of the very thin films ($< 100nm$) in the SEM observation, the error in thickness measurement is estimated to be up to 10%.

The film thickness can also be inferred from the XPS measurements of the depth profiles used to determine a composition variations at the interface region (see section 7.2.4). Since, in this case the ratio between the film thickness of each sample is correct, the film thickness can be inferred from a precisely measured film thickness for a thick sample. The value of the thickness for this sample is $0.87um$ obtained through three different methods.

In the deposition process, a standard sample was mounted inside the deposition

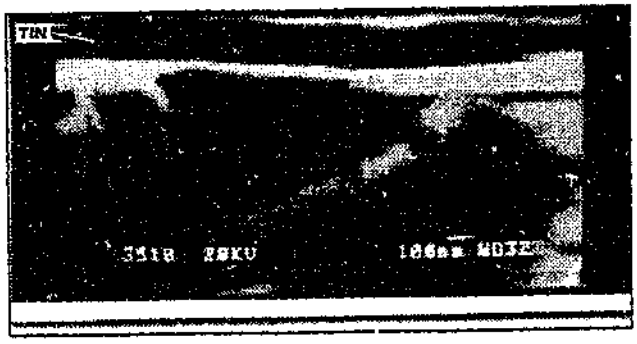


Figure 7.2: SEM fractograph of the $TiN/HSS$ deposited in 2 minutes using the parameters described in text. The layer at the top is $TiN$.

chamber next to the steel substrate. The standard sample has an as-deposited surface which has an accurate area. The film thickness of this sample was obtained by SEM micrography of its cross section and also by a the mass variation of the sample provided the density of the film is $5.4 g/cm^3$. The thickness of this sample was further verified by nitrogen depth profiling using the nuclear reaction $^{15}N(p,\alpha,\gamma)^{12}C$. The accuracy of the thickness measurements for this sample is estimated to be better than 5%.

### 7.2.2 Topography and Composition of TiN Film and HSS

The topography of the $TiN/HSS$ and $HSS$ samples is observed through SEM, and inhomogeneous structures are found for bare $HSS$ as shown in figure (7.3). In this figure, the scattered white spots located on the surface are obviously something different from the remaining area. The EDX-ray (LINK AN 10000 ) technique was used to

investigate their chemical composition, showing that the white spots have much more $W$ and $Mo$ than in the remaining area. For a thick film ($4.18\mu m$) and a thin film ($240nm$), the SEM micrographs are shown in Figures (7.4, 7.5), and no pronounced inhomogeneous structure is found. It should be noted that the electron energy used for taking the micrograph in figure (7.5) was $6kV$, sufficiently low to avoid revealing information from the substrate. An EDX-ray analysis was also carried out for the films. For the thin film shown in figure (7.6), there are peaks from $Fe$, $W$, $Mo$, $V$ and $Cr$ in addition to $Ti$. Unfortunately the penetration of the electron in the EDX ray method was of order $1\mu m$, so that the technique detected not only the composition of the film but also that of substrate. For the thick film only $Ti$ is detected appreciably as shown in figure (7.7). Nitrogen can not be detected by the EDX-ray analyzer due to its low atomic weight.

The atom percentage of films and substrate by EDX-ray are given in table 7.1. For the thin film, various areas on the surface were measured, and it was found that the atom percentage of $TiN$ was always from 14 to 20, indicating that the film indeed covered the whole area of the substrate. It should be noted that the figure of 20 results from the white spot areas which are only a very small portion of the total area.

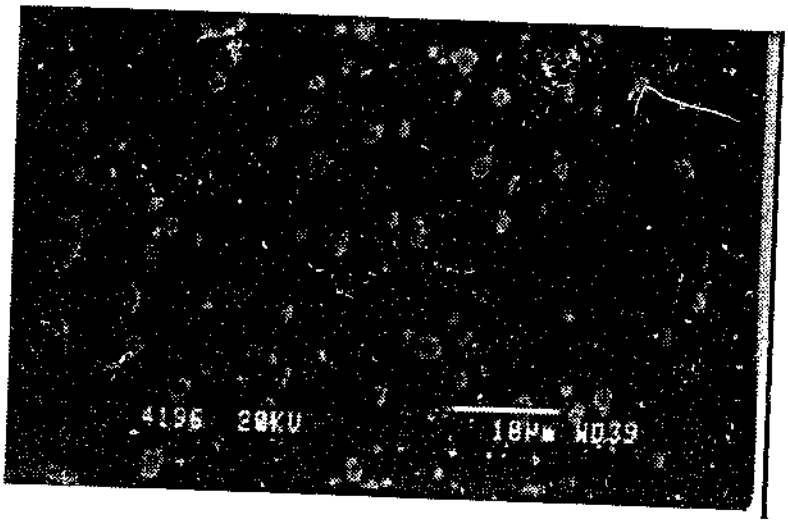


Figure 7.3: SEM topography of the $HSS$ substrate at $20kV$. The white spots on the surface are $W$ and $Mo$ enriched areas.

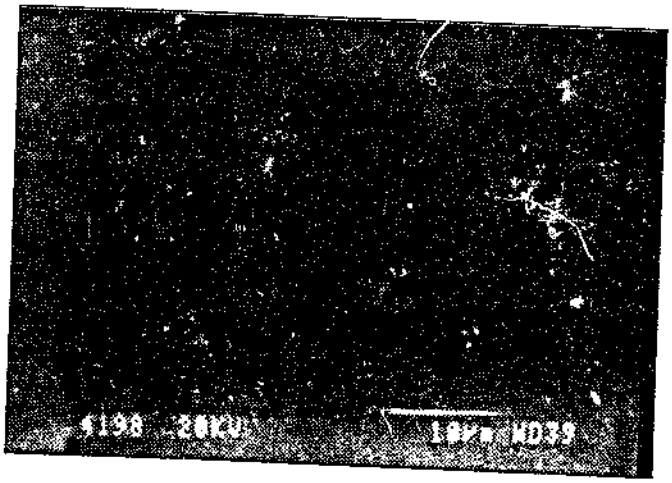


Figure 7.4: SEM topography of the $TiN/HSS$ with the film thickness 4180nm at $20kV$.

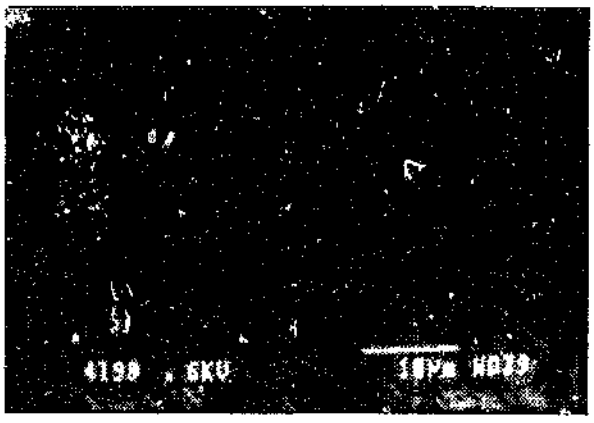

Figure 7.5: SEM topography of the $TiN/HSS$ with the film thickness about 200nm at $6kV$, sufficiently low to avoid penetrating the substrate.

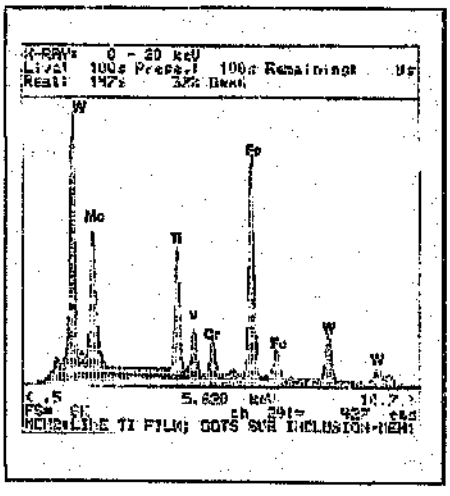


Figure 7.6: The elemental composition of the $TiN$ film of about $200nm$ thickness by EDX-ray including contributions from the $HSS$ substrate. The electron energy used was $20keV$.

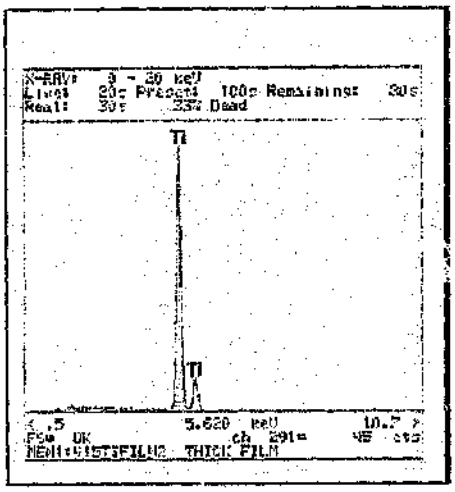


Figure 7.7: The elemental composition of the $TiN$ film of $4.18\mu m$ thickness by EDX-ray. The electron energy used was $20keV$.

| Sample/Atom.% | $V$ | $Cr$ | $Fe$ | $W$ | $Mo$ | $Ti$ | Description |
|---|---|---|---|---|---|---|---|
| $HSS$ * | 6.4 | 7.4 | 37.5 | 21.0 | 26.9 | — | White spot areas |
| $HSS$ | 1.9 | 7.9 | 84.8 | 1.80 | 2.40 | — | The remaining area |
| $TiN$ *$(200nm)$ | 4.8 | 6.0 | 30.5 | 17.9 | 20.9 | 19.5 | $TiN$ on white spot areas |
| $TiN$ $(200nm)$ | 1.7 | 6.9 | 71.3 | 1.69 | 2.88 | 14.9 | $TiN$ on remaining area |
| $TiN$ $(4180nm)$ | — | — | .395 | — | — | 97.9 | Thick film |

Table 7.1: Atomic percentage of the main elements in the substrate and in the TiN films. For EDX-ray analysis, the depth of the electron penetration is around $1\mu m$ at 20keV.

### 7.2.3 Lattice Parameter and Preferred Orientation of *TiN* Films

Figure (7.8) shows the measured results of the *TiN* film samples using scanning X-ray diffraction. *Cu Kα* radiation generated with a $39kV$ potential difference between the heated cathode and the copper anode of the X-ray tube was used. The strongest narrow peak is found at a diffraction double angle of $2\theta = 36.85°$. Using Bragg's law

$$2d\sin\theta = m\lambda, \quad m = 1, 2, 3, \tag{7.1}$$

where $d$ is the atomic interplanar spacing and $\lambda$ (0.1540 $nm$) is the wavelength of *Cu Kα* radiation, the calculated value of $d$ for the strongest peak is 0.2436 $nm$. The value of $d$ was also calculated for the other peaks. Through the comparison of the obtained $d$ values with the X- ray diffraction ASTM standard card (No. 6-0642) of *TiN* material, it is inferred that the strongest peak comes from the [111] planes. In other words, we can say that the *TiN* films are strongly of [111] preferred orientation, i.e. the crystallites of the films are mainly distributed with their [111] planes parallel to the film surface. Since a single crystal of *TiN* is of face centered cubic structure, the [111] plane is the most close-packed surface with the lowest surface energy. The average of elastic constants for this type of distribution of crystallites have been discussed in section 2.2.

An ideal single crystal of *TiN* at the stoichiometric composition has a lattice parameter of 0.4240 $nm$. The interplanar separation of the [111] planes for this single crystal is calculated to be 0.2447 $nm$. The measured $d$ value of [111] planes for the polycrystalline film is a little less than that of the single crystal. This may be caused

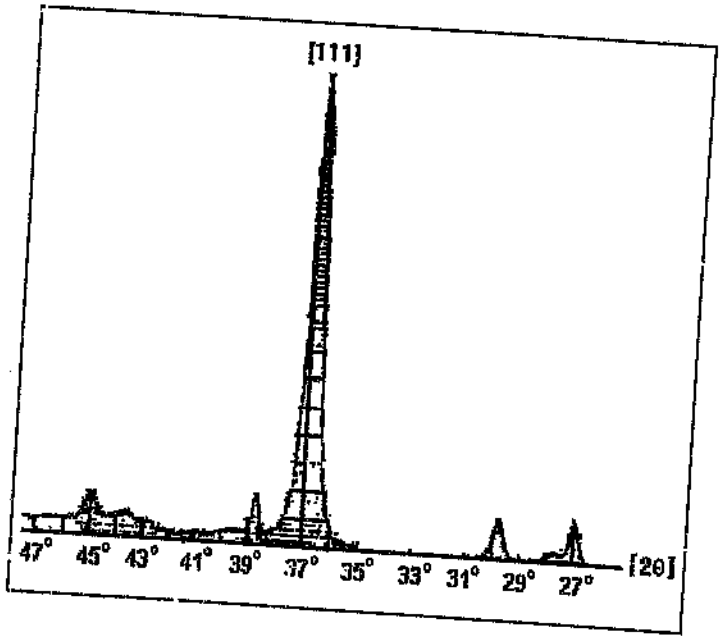


Figure 7.8: X-ray diffraction measurement of lattice parameter and preferred orientation of polycrystalline TiN films deposited by D. C. magnetron sputtering. $Cu\ K\alpha$ radiation from an X-ray tube operated at $39kV$ was used. The chart speed was $2cm\ min^{-1}$.

by the stress in the film formed in the deposition process due to the differences in thermal expansion coefficients between the film and the substrate and thus the lattice parameter is perturbed. Because sputtering involves many argon particles in the plasma, another possible reason is that the incorporation of argon into the lattice causes high compressive stress in the film and affects the lattice parameter. The elastic properties of the films to a certain extent are also influenced by this existing stress.

### 7.2.4 XPS Profile Analysis of Composition at $TiN/HSS$ Interface Region

In order to interpret the measured SAW velocity for the thinner $TiN$ films, we have performed XPS measurements as a function of depth on all the samples using a Physical Electronics Quantum model 2000 instrument. The $40W$ beam of monochromatic Al $K_\alpha$ X-rays used in these measurements had a focal point size of about $200\mu m$. The depth profiles have been performed by alternately sputtering the surface with argon ions (2KeV) and measuring the XPS spectrum. The calibration was performed using a $SiO_2$ layer on silicon, where the layer thickness is precisely known. Representative results, for film thicknesses of $350nm$ and 190, and $20nm$, are shown in figures (7.9, 7.10, 7.11). These figures demonstrates rather complicated compositional variations in the interface region with the oxide layers ($TiO_2$ or $TiO$) being distinguishable, while other compositional variations are present at smaller concentrations.

It should be noted that although most of the samples were deposited in the same

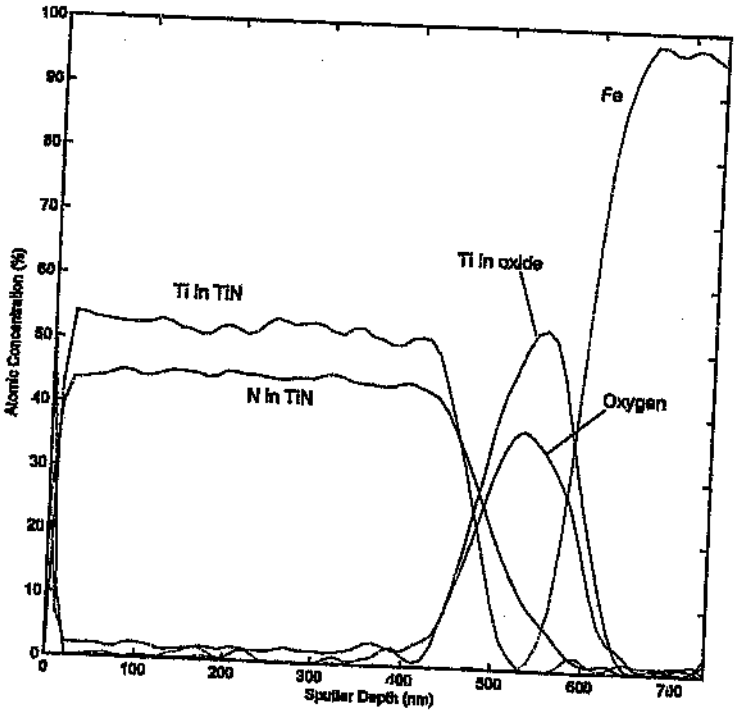


Figure 7.9: XPS depth profile measurements for the $350nm$ film. Oxide layers are distinguishable at the interface, while other compositional variations are present at smaller concentrations.

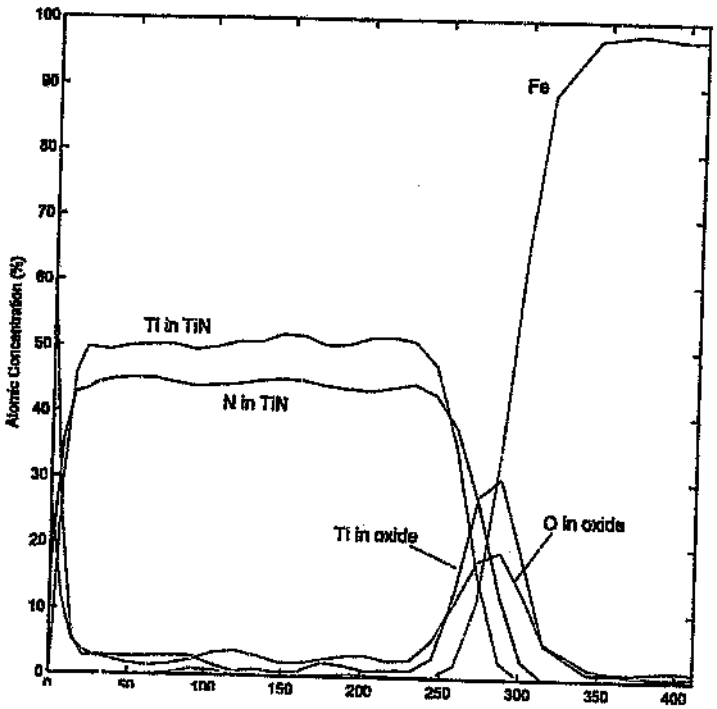


Figure 7.10: XPS depth profile results for the $190nm$ film. Oxide layers are distinguishable at the interface, while other compositional variations are present at smaller concentrations.

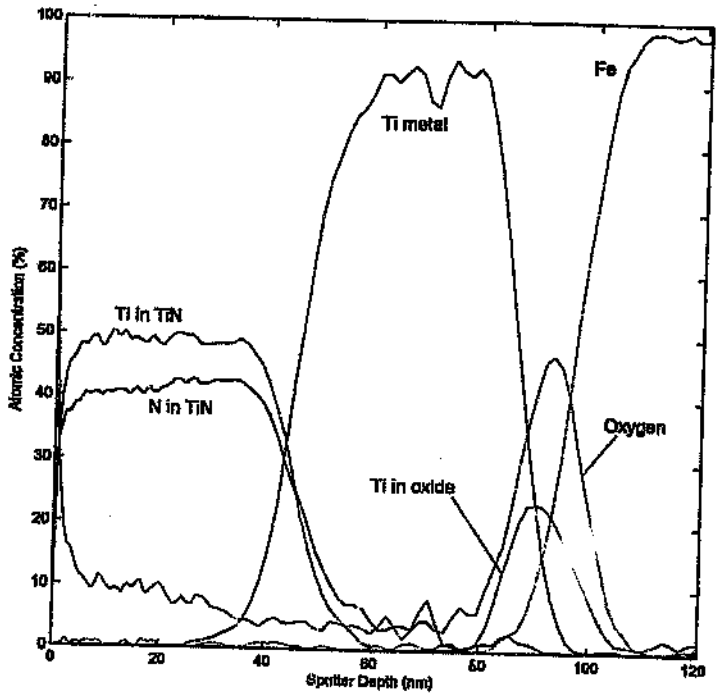


Figure 7.11: XPS depth profile measurements for the $20nm$ film. There is a $Ti$ layer in addition to oxide layers.

batch, the samples of $20nm$ and $90nm$ thickness were deposited separately. The XPS results show that there is an additional $Ti$ layer over the titanium oxide in these two samples, which offers a rather complicated multi-layer system. The absolute values of the $TiN$ depths (film thickness) revealed in XPS measurements are significantly in error (up to 30%) by comparing these directly with the measurements described in section 7.2.1 for these films, but the ratio between the thicknesses of the films must be correct since the calibration is the same for all the samples.

# Chapter 8

# Brillouin Scattering Measurement of the Elastic Properties of *TiN/HSS*

Surface Brillouin scattering probes thermally excited phonons in the GHz frequency range which give rise to surface displacements in opaque or semi-opaque materials. Depending on the substrate and film combination, there are various excitations localized near the surface that can be probed, including Rayleigh or surface acoustic waves (SAWs), Sezawa waves, Lamb waves and pseudo-surface acoustic waves (p-SAWs). For some combinations, Stoneley waves and other interface excitations can also be measured [31], [30]. By analyzing Brillouin scattering (BS) spectra, identifying the presence of particular acoustic modes and comparing these with calculations, one can extract information pertaining to the texture, adhesion, film thickness and elastic

properties of supported solid films [37]-[40].

The use of surface Brillouin scattering to study the elastic behaviour of $TiN$ films on glass substrates[ ], on <111> oriented silicon wafers [50] and $TiN/(V_xNb_{1-x})N$ superlattices [51] has been reported recently. In these measurements, only true SAWs have been reported, and then only for a very limited range of film thicknesses.

We have conducted Brillouin scattering measurements of the elastic properties of $TiN$ films over steel, a stiffening system, as a function of film thickness, nitrogen partial pressure and temperature. In contrast to softening layers, relatively few papers have been published on the effects of stiffening, particularly with regard to p-SAWs [34] and their higher modes in the region beyond where the Rayleigh wave degenerates into the bulk wave continuum. The $CaF_2/GaAs(111)$ heterostructure [52] was studied as a fast-on-slow structure, and a pre-Rayleigh mode has been identified. There have been acoustic microscopy studies of leaky surface waves in $AlO/Al$ [53]-[54] and $TiN$ coatings on steel [55]-[56], both of which combinations are fast on slow systems. A theoretical study has been reported of the leaky p-SAWs using a reflectance function [57].

In this chapter, measured Brillouin spectra for some typical film thicknesses are presented in section 1. The various acoustic modes and the way they come into and out of prominence are described, including SAW, p-SAW and its higher order modes. Measured spectra are compared with spectra calculated using the Greeen's function method of the previous chapter. Good consistency is found for thick films ($h > 0.8um$) and the bare substrate ($h = 0$). The discrepancy for fairly thin films ($\leq 500nm$) is interpreted in terms of a reduction of the elastic constants of these films and internal

stress in the films. Comparison between the measured and calculated dispersion curves ($v$ vs. $h$ and $v$ vs. $k_{||}h$) shows that the elastic constants of the thinner film decrease as the film thickness decreases. A reasonable conformation between the measured and calculated dispersion curves is obtained using elastic moduli for $TiN$ which are about 25% smaller than those of bulk $TiN$. A possible explanation for the lowered elastic moduli of the thinner films could be composition variations at the $TiN/HSS$ interface.

Section 2 describes the correlation between the measured SAW velocity and residual stress and adhesion force of the TiNx films to their substrates. The lattice parameter and preferred orientation of the TiNx films were measured using X-ray diffraction and the compressive stress determined using the $\sin^2\theta$ method [60]. The stress in the films has a trend opposite to that of the SAW velocity. The adhesion force of the film to the substrate is measured by the critical load method which has the same trend as the SAW velocity. The good correlations between the SAW velocity and stress and critical load indicates that Brillouin scattering can thus be used as a non-destructive method for investigating the stress states and adhesion force of coatings. All the measured values of phase velocities are above the Rayleigh velocity of the $HSS$ substrate indicating that there is proper contact at the interface. A quasi free standing thin film would have a much lower velocity.

In section 3, the elastic constants of thick TiN films at temperatures up to $600°C$ are obtained from measured SAW velocities. There is a downward trend of the SAW velocity and hence elastic moduli with increasing temperature.

## 8.1 Measured Spectra from Various Guided Acoustic Modes

A series of Brillouin scattering measurements have been carried out on $TiN/HSS$ for various film thicknesses ranging from 20 to 4180 $nm$, and on the bare $HSS$ substrate. Some typical measured results for scattering intensity vs. frequency shift are shown in figure (8.1). In this figure, it can be seen that for the bare substrate, there is a single peak centered at 10.5 GHz, which corresponds to the Rayleigh wave of $HSS$. For the given scattering geometry, the Lamb shoulder extends from the transverse wave threshold at 11.4 GHz through the longitudinal wave threshold at 21.3 GHz and to higher frequencies. For the $HSS$ substrate, the Lamb shoulder cannot easily be distinguished above the noise background.

A true SAW is obtained for the very thin film ($h \simeq 20nm$, $k_{\|}h \simeq 0.46$). The frequency shift of the peak in the Brillouin spectrum is slightly larger than that for $HSS$ due to the stiffening effect of the $TiN$ film on the $HSS$. As the film thickness increases further, the Brillouin peak approaches and then merges into the Lamb shoulder. As this occurs, the corresponding mode transforms into a p-SAW. The bulk wave component of the p-SAW radiates the energy of this mode into the substrate, and this is responsible for the Brillouin peaks for the $60nm$ ($k_{\|}h \simeq 1.37$) and $110nm$ ($k_{\|}h \simeq 2.51$) samples being somewhat broader than for the $HSS$ and $20nm$ sample. The frequency shift of the p-SAW in this region varies rapidly with film thickness.

For the $350nm$ ($k_{\|}h \simeq 7.98$) and $420nm$ ($k_{\|}h \simeq 9.58$) films, two prominent peaks

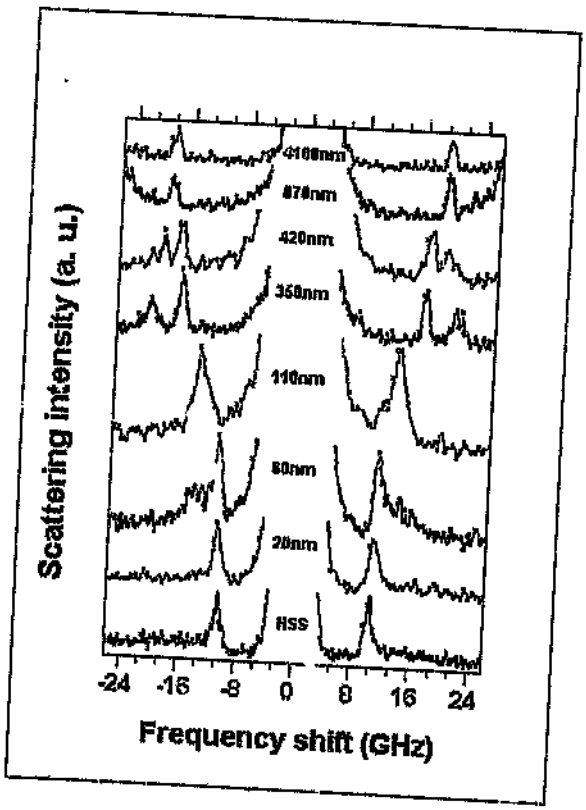


Figure 8.1: Some typical measured Brillouin spectra for $TiN/HSS$. The laser beam intensity was $300mW$ with the $\vec{E}$ vector polarized in the plane of incidence, while the collected light was unpolarized. The incident angle $\theta_i$ with respect to the surface normal was 70°.

are observed in the Brillouin spectrum. The lower frequency peak is due to the p-SAW and the other peak is due to a higher order p-SAW (see discussion below). The p-SAW has a relatively higher scattering intensity and a relatively sharper peak in the spectrum than the higher mode, which suggests that the latter mode is more strongly coupled to the bulk modes of the substrate. For the $870nm$ ($k_{\|}h \simeq 19.84$) film, several peaks are observed (see figure (8.2)) which are due to the p-SAW and its higher order modes. Only a single peak is observed for the $4180nm$ ($k_{\|}h \simeq 95.34$) film, corresponding to the Rayleigh wave of $TiN$.

### 8.1.1 Comparison Between the Measured and Calculated Spectra Using Adjusted Elastic Moduli of $TiN$

While the above explanation is able to qualitatively account for the observed Brillouin spectra, there is a discrepancy between the calculated and measured positions of the peaks for the thinner films.

The frequency shifts for film thickness in the range $?\,nm$ to $420nm$ all lie below their calculated values, the discrepancy being most pronounced for the thinnest films. The most ready explanation for this is that the elastic constants for the thin films are effectively smaller than those of bulk $TiN$. Density variations, due for example to porosity, are likely to be in the form of a reduction, which would have the opposite effect of increasing the surface velocity. Figure (8.2) shows a comparison between measured and calculated Anti-Stokes spectra using suitably adjusted values of the elastic constants of $TiN$. The measured spectra are fitted using a Gaussian

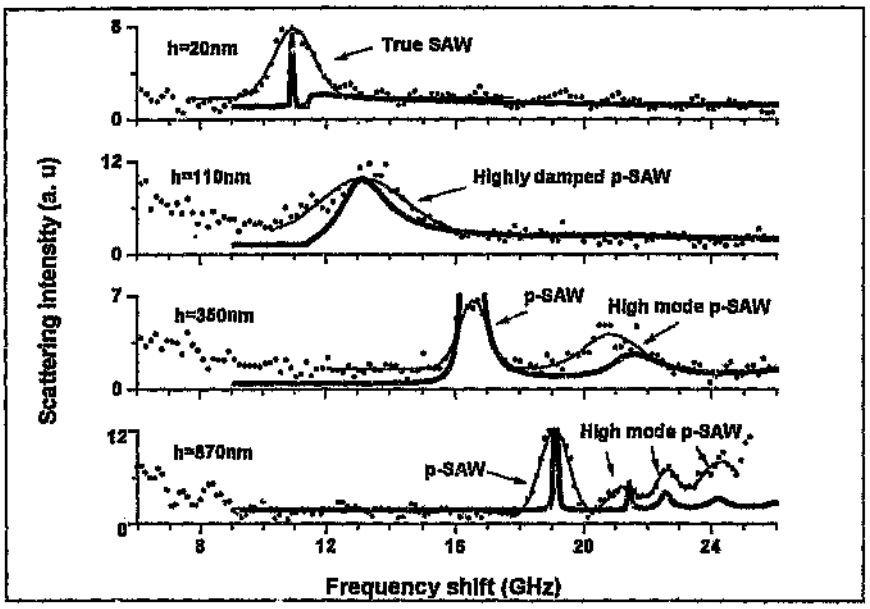


Figure 8.2: Comparison between the measured and calculated spectra of $TiN/HSS$ for some typical film thicknesses. In the figure, the thin solid line is the Gaussian fitting of the measured data (the dots), and the thick line is the calculated spectrum. Reduced stiffness constants for the $TiN$ films are used in calculating the spectra.

distribution function.

Good agreement is obtained for the $20nm$ and $110nm$ films when the elastic constants of $TiN$ are reduced to 60% of their bulk values. For the $350nm$ film, the best fit is obtained when the elastic constants of $TiN$ are reduced to 75% of their bulk values. For the $870nm$ film, no adjustment of the elastic constants of $TiN$ is necessary to account for the main Brillouin peak, which lies very close to the frequency predicted for the Rayleigh wave of $TiN$. Likewise, for the $HSS$ substrate and $4180nm$ films, no

adjustment of elastic constants is required to quantitatively account for the Brillouin peaks.

### 8.1.2 Experimental Errors in Surface Brillouin Scattering

It should be noted that whereas the calculated and measured peak positions are in good agreement, the peak widths differ. The calculated spectra include a small damping factor to deal with the computational difficulties arising from the singularity in $\mathbf{B}^{-1}$ (see equation (5.21)). The difference between the calculated and measured spectra for the $20nm$ and $870nm$ films results largely from instrumental broadening. For the p-SAW calculations, where the same damping factor was used, the peaks are considerably broader. This arises from the form of the respective minima in $|\mathbf{B}|$. For purposes of comparison and clarity of presentation, arbitrary adjustments have been made to the vertical scale for the calculated spectra.

Although adjusted values of the elastic constants of $TiN$ have been used, there is still a slight discrepancy between the measured and calculated frequency shifts in figure (8.2). This can be attributed to experimental error. The errors induced in surface BS measurements have been studied in detail [39] [80] and are associated with various factors such as the finite collection lens aperture, sample surface roughness and residual stress in the films. These factors also contribute to the broadening of measured spectra as discussed above. Generally speaking, the error in measurement is around 1% with the incidence angle deviation and calibration error being taken into account.

### 8.1.3 Acoustic Behaviour of Thinner $TiN$ Films

The conclusion from the above discussion is that the effective elastic constants of the films vary with the film thickness. Overall, for the films of thickness less than $500nm$, the measured data can be reasonably well accounted for by elastic constants which are 75% of the values of those of bulk $TiN$. This is demonstrated in figure (8.3), which shows the dispersion curve of $v$ vs. $h$ for the fixed $k_{||}$ in our experiment. Overall there is reasonable agreement between the measured data and the calculated dispersion curves. For the thinner films, the data lie a little below the calculated curve, indicating slightly lower elastic constants for the films, while for $500nm$, the data lies slightly above the dispersion curve, indicating elastic constants that approach those of bulk $TiN$.

### 8.1.4 Acoustic behaviour of Thick $TiN$ Films

For the thickest films ($h \geq 870nm$), the measured p-SAW velocity is very close to the Rayleigh velocity for bulk $TiN$. The measured phase velocities of p-SAW and its higher order modes conform rather well with the calculated results. The Rayleigh wave propagating on these films has a wave length $2\pi/k_{||} = 275.4nm$, which is much less than the film thickness. The p-SAW on these "thick" $TiN$ films are not much affected by the existence of the $HSS$ substrate, although their higher modes are. Measurements on films of thickness $1320nm$, $2630nm$, and $4180nm$ have also been carried out. The results for these films are very close to those for $870nm$, i.e. the p-SAW velocities are very close to the Rayleigh velocity for $TiN$ except that the

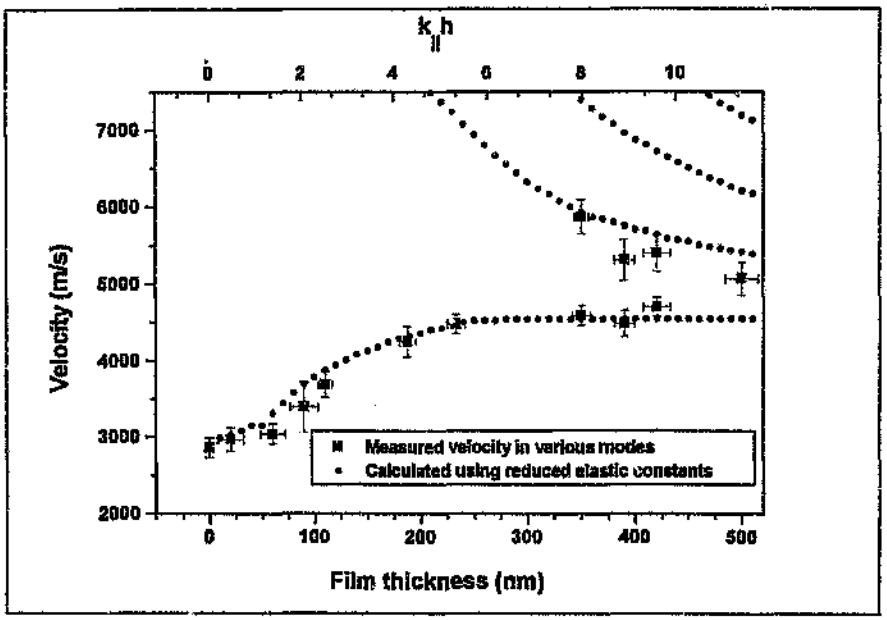


Figure 8.3: Comparison between the measured and calculated wave velocities of $TiN/HSS$ as a function of film thickness (bottom axis) and $k_{\|}h$ (top axis), where reduced elastic constants of $TiN$, which are 75% of the values for bulk $TiN$, are used in calculating the dispersion curves. For film thickness $h > 870nm$ (not included in the figure), the measured results conform rather well to the calculated ones based on the elastic constants of bulk $TiN$.

frequency shifts of the higher modes of their p-SAWs vary with film thickness. As the film thickness increases, more peaks representing higher modes appear, but these peaks are compressed into a quasi-continuous spectrum and cannot be resolved in the measurements. This is demonstrated in figure (8.4), where comparison between the measured and calculated Brillouin scattering spectra for the thick films of $870nm$ and $4180nm$ is presented. If the Poisson's ratio of the films is assumed to be 0.2 [49], the averaged stiffness constants of these "thick" $TiN$ films obtained from the measured SAW velocity of the $4180nm$ film are $c_{11} = 4.652 \times 10^2 GPa$, $c_{12} = 1.163 \times 10^2 GPa$ and $c_{44} = 1.745 \times 10^2 GPa$ (see section 8.3). For $h = 0$, the measured SAW velocity is the Rayleigh velocity of the bulk substrate, which also conforms well with the calculated value.

The measured phase velocities obtained from equation (6.12) together with the theoretical values for $TiN/HSS$ are given in table 8.1, where the theoretical values are calculated using the bulk elastic constants of $TiN$.

### 8.1.5 Measured p-SAW and its Higher Order Modes for the $350nm$ Film as a Function of Incident Angle

Brillouin spectra measured at different incident angles for the $350nm$ film are shown in figure (8.5). As the incident angle increases from 50° to 80°, corresponding to $kh$ varying from 6.5 to 8.4, double peaks are observed in all cases and the frequency shifts of the p-SAW undergo more change than those of the higher order p-SAW mode. Because the scattering cross section is a function of the incident angle of the light on

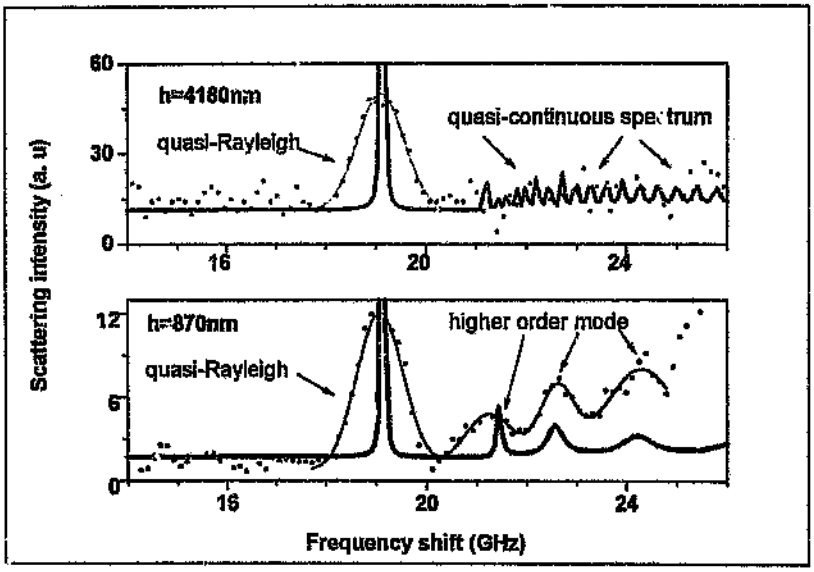


Figure 8.4: Comparison between the measured and calculated Brillouin scattering spectra for thick $TiN$ films over $HSS$. Higher order modes can be seen clearly in this figure, but the quasi- continuous spectrum can not be resolved in the spectra.

| thickness(nm) | velocity$^{the}$(m/s) | velocity$^{mea}$(m/s) |
|---|---|---|
| 4180 | 5245.23 | 5217.04 |
| 4180 | 5245.23 | 5211.07 |
| 1320 | 5245.23 | 5146.68 |
| 870 | 5245.23 | 5223.33 |
| 870 | 5871.65 | 5817.39 |
| 870 | 6181.45 | 6184.23 |
| 870 | 6638.51 | 6652.36 |
| 500 | 4538.93 | 5061.82 |
| 420 | 4538.93 | 4697.72 |
| 420 | 5633.97 | 5398.54 |
| 390 | 4538.93 | 4484.18 |
| 390 | 5748.95 | 5308.21 |
| 350 | 4538.93 | 4585.48 |
| 350 | 5929.63 | 5869.41 |
| 230 | 4470.49 | 4475.97 |
| 180 | 4287.08 | 4251.49 |
| 110 | 3876.43 | 3690.28 |
| 90 | 3695.76 | 3394.62 |
| 60 | 3307.02 | 3041.47 |
| 20 | 3033.25 | 2970.29 |
| 0 | 2913.68 | 2860.79 |

Table 8.1: Theoretical and measured phase velocities of guided acoustic modes for *TiN/HSS* with various film thicknesses.

the scattering surface [39], the intensity is largest near 65° ($k_{||}h = 7.7$). A comparison between the measured and the calculated wave velocity $v$ vs. $k_{||}h$ is shown in figure (8.6). A reduction of the elastic constants of $TiN$ to 75% of their bulk values is able to account reasonably well for the measured data.

### 8.1.6 Discussion of the Lowered Elastic Moduli

In an effort to understand why the effective elastic constants of the thinner films should be less than those of bulk $TiN$, we have performed XPS measurements as a function of depth on all the samples (see section 7.2.4). The reduction of the elastic constants is likely to be due, partly at least, to the rather complicated composition variations at the $TiN$ - $HSS$ interface. For most of the samples, the depth of mixing of $TiN$ and oxide ($TiO_2$ and/or $TiO$) is about $100nm$ which remains nearly constant. Because the mixed layers have unknown mechanical properties (density and elastic constants) and/or physical properties, their elastic properties could be significantly different from $TiN$ and/or $HSS$, but its bulk shear velocity ($\sqrt{c_{44}/\rho}$) must lie between those of $TiN$ and $HSS$ since all the measured velocities are larger than the Rayleigh velocity of $HSS$. The effective elastic constants used in the calculation of the figure (8.3) were just an indication of overall mechanical properties of the interface region in which the density was assumed to be that of bulk $TiN$. As the film thickness decreases, the effect of the interface region on the elastic moduli of the $TiN$ film should increase, as observed experimentally. This is because the thickness of the interface layer occupies a larger proportion of the film volume in the case of thinner films. In

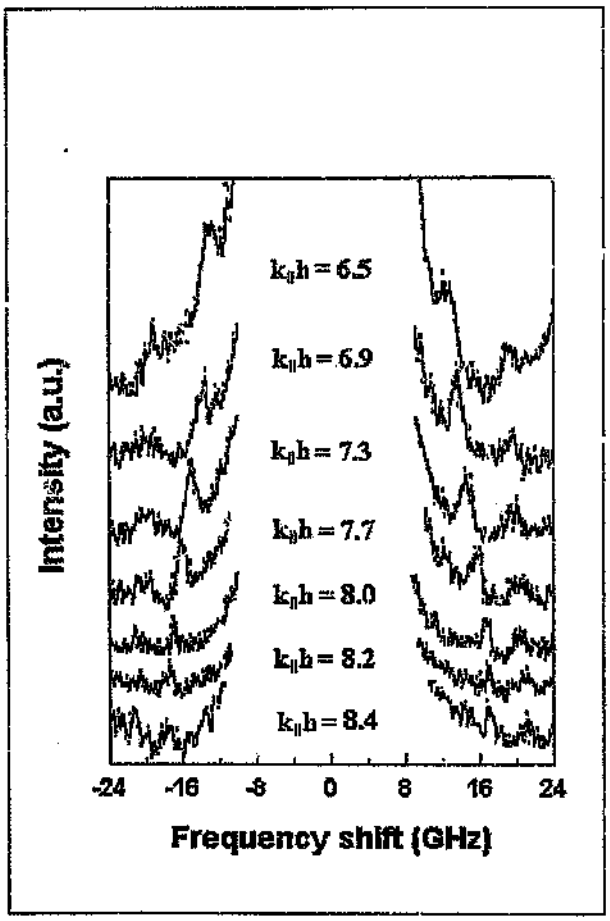


Figure 8.5: Measured spectra for the $350nm$ film obtained by varying the light incident angle between 50° ($k_{||}h = 6.5$) and 80° ($k_{||}h = 8.4$). The collection lens has a focal length of $50mm$ and aperture $f/2.3$. The peak with lower frequency shift corresponds to the p-SAW and the other one to its higher order mode.

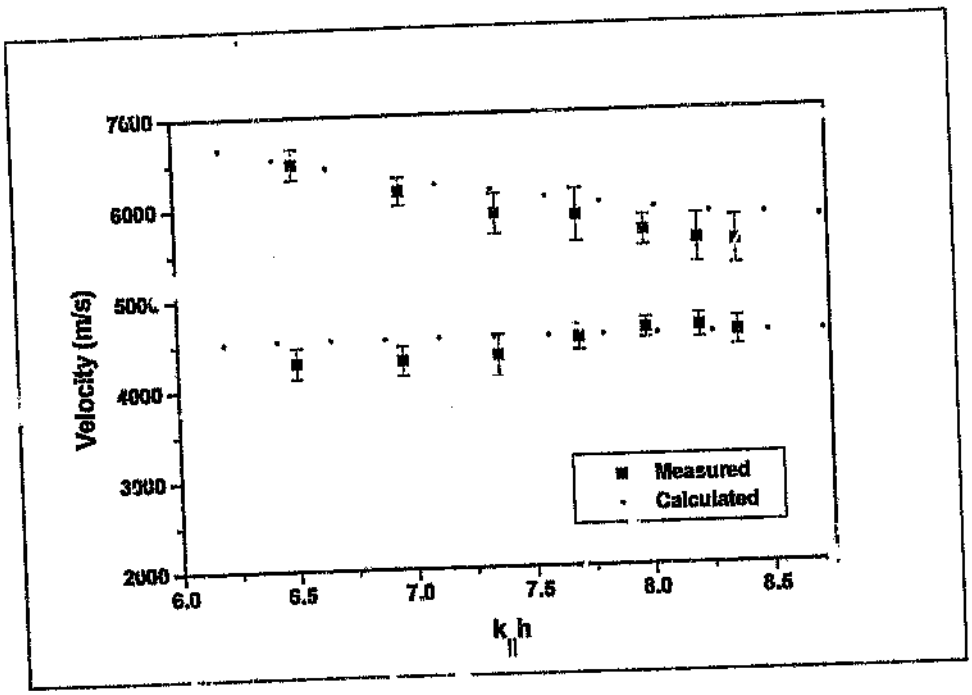


Figure 8.6: Comparison between the measured and calculated dispersion relations of p-SAW and its higher order mode for the $350nm$ film through varying the incident angle $\theta_i$ from 50° to 80°. The calculated curve is based on the reduction of the elastic constants of the film to 75% of the bulk $TiN$ values.

fact, the existence of oxide layers over the HSS makes this system a rather complicated multi-layer structure. A complete theoretical analysis of this "f structure" in the film would require further extensions of the Green's function treatment, and is beyond the scope of this thesis.

Various other factors may play a secondary role in modifying the elastic constants of the thinner films. For example, when the grain size of the $TiN$ is comparable to the film thickness, one has a situation where the grains are not yet properly consolidated into a mass, and so the resistance to deformation of thin films is less than for the bulk material. Non-uniformity in the film thickness which may be relatively more pronounced for the thinner films, can also yield lowered effective elastic constants. The inhomogeneous structure (white spots) existing in the substrate as shown in the figure (7.3) could bring about the discrepancy with the theoretical calculations which are based on the assumption of homogeneous isotropic media. Since the proportion of white spots on the surface is less than 10%, the effect might be expected to be small. Other possible contributions could be the variation of the elastic constants caused by the incorporation of argon atoms into the lattice (also see section 7.2.3), and high internal stress in the thin films accompanying the short deposition process.

Elena et al. [50] observed $TiN$ films on Si wafers using Brillouin scattering. It is also found in their measurements that $TiN$ films having thickness of $120nm$ and $60nm$ have a much lower value of SAW velocity than expected. Their proposed reason is that the shear modulus of the interface layer should be considerably lower than that of both film $TiN$ and substrate Si. This is not what we have observed. Since all our measured velocities are higher than that of $HSS$, the elastic constants of the interface

lie between that of $TiN$ and $HSS$. Jiang [49] studied the $TiN/glass$ system with a film thickness between $300 - 900nm$, and no exceptionally low value of the SAW velocity was reported. The model in their calculation was essentially that described by equation (4.8) for a half space medium.

Hillebrands et al. [24] have investigated elastic surface and localized modes using the $Au/glass$ combination. They found that a deviation from the dispersion relation described by elastic continuum theory occurred for a film thickness $\leq 100nm$. It was claimed that there is island formation (inhomogeneous film growth), which causes the deviation. Our SEM and EDX-ray investigation (see section 7.2.2) shows that there is no island structure obvious in the thinner $TiN$ films ($\leq 500nm$). For Rayleigh modes of the $ZnO$/Si combination studied by Carlotti et al. [27], appreciably lowered values of phase velocities occurred for $ZnO$ thicknesses $\leq 150nm$. This was interpreted as a result of a reduction of the effective elastic constants of the film in a layer near the interface, due to the lattice misfit between the film and the substrate.

All the measured phase velocities are greater than the Rayleigh surface wave velocity of the pure substrate indicating that proper contact exists between the films and the substrate. This conclusion is based on the theoretical calculations which assume that intimate mechanical contact exists at the interface. From this assumption, the boundary conditions, i.e. traction components of stress and particle displacements are continuous across the interface have been applied to solve the surface wave propagation in the supported films. If intimate contact (e.g. a air gap) were not to exist at the interface, the measured surface wave velocities for the thin unsupported films would be much less than the Rayleigh velocity of $HSS$.

## 8.2 Measured SAW Velocity for Stressed $TiN_x$ Films

### 8.2.1 Measured Brillouin Scattering Spectrum as a Function of $N_2$ Partial Pressure

We have carried out Brillouin scattering measurements of $TiN_x$ films on mild steel and $HSS$ as a function of the nitrogen partial pressure during film growth. Figure (8.7) shows the measured results for the $TiN$ film on mild steel. The peak position moves towards a larger frequency as the nitrogen partial pressure increases in the range of $6.7 \times 10^{-3}$ to $3.3 \times 10^{-1}$ $Pa$, and then the frequency decreases a little at $6.0 \times 10^{-1}$ $Pa$ of $N_2$ partial pressure. The peaks in the figure represent a quasi-Rayleigh mode since the films are rather thick and the substrate has little effect on acoustic behaviour of the system.

### 8.2.2 Correlation Between the SAW Velocity and Residual Stress and Adhesion Force

The SAW velocity as a function of nitrogen partial pressure is obtained using equation (6.12), which is plotted together with the residual stress in the films as figure (8.8). The lattice parameter and preferred orientation of the $TiN_x$ films were measured using X-ray diffraction and the compressive residual stress determined using the $\sin^2\theta$ method [9], [60]. The possible reason for change in residual stress has been discussed in section 7.1. As evident in the figure, the measured SAW velocity increases as the $N_2$ partial pressure increases in the range of $6.7 \times 10^{-3}$ to $3.3 \times 10^{-1} Pa$, and then

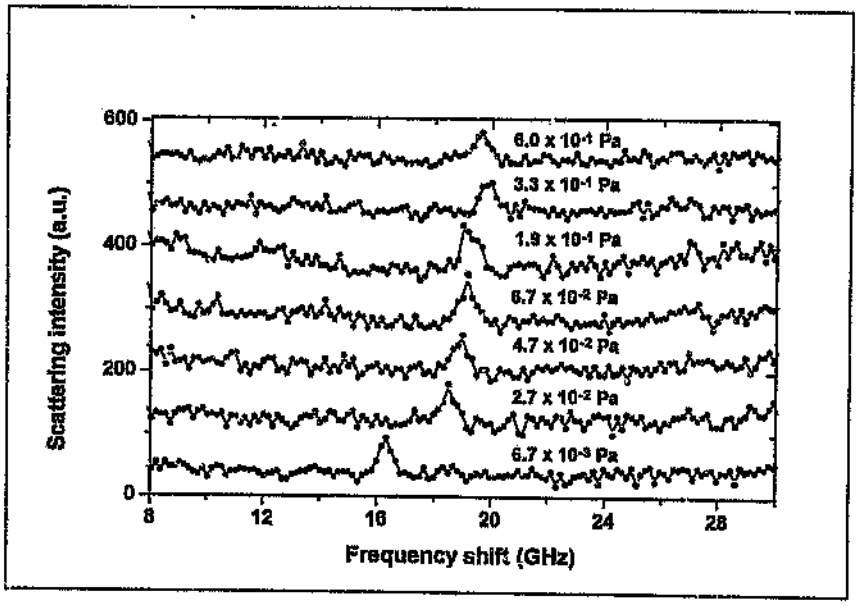


Figure 8.7: Measured anti-Stokes Brillouin scattering peaks as a function of the nitrogen partial pressure for $3.5\mu m$ $TiN$ films on mild steel. The laser beam intensity was $400mW$ with the $\vec{E}$ vector polarized in the plane of incidence, while the collected light was unpolarized. The incident angle $\theta_i$ with respect to the surface normal was 70°.

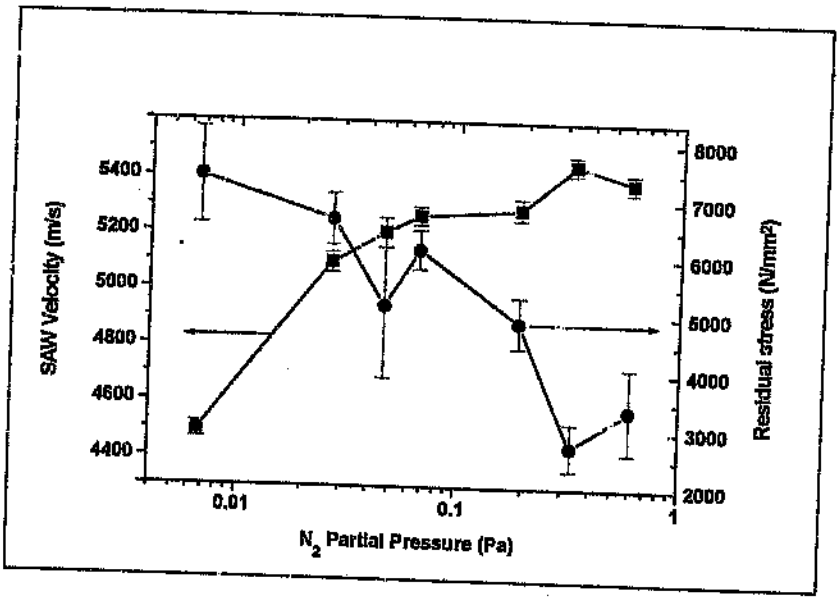


Figure 8.8: Correlation between the measured SAW velocity and residual stress in $3.5\mu m$ TiN films. The stress was obtained using a $\sin^2\theta$ method based on the X-ray diffraction measurements of lattice parameter and preferred orientation of the films.

drops slightly for largest $N_2$ partial pressure. The residual stress in the films has a trend opposite to that of the SAW velocity. This good correlation indicates that Brillouin scattering can be used as a non-destructive method for investigating the stress states of coatings.

The adhesion force of the film to the substrate is measured by the critical load method for the stressed samples. These samples are prepared under proper deposition conditions to ensure that tightly adhesive films are obtained, and this is confirmed by a scratch test where no adhesive failure is detected. The critical load $L_c$ is defined as the smallest load at which the film is damaged when an increasingly loaded diamond

stylus is drawn across the film. The damage is judged by emitted acoustic signals. The measured SAW velocities and critical loads for the TiN films on both mild and high speed steel are shown in figure (8.9), in which it can be seen that the saw velocity has the same trend as that of the critical load, at least for the combination of TiN on high speed steel. The values of the critical load for the film on high speed steel are much different from the film on mild steel. This is likely due to the fact that the mild steel is much softer than the high speed steel and therefore tends to deform plastically under the applied load, leading to earlier crack propagation in the films and th:  :oating failure at lower loads.

As revealed in the above discussion, the correlations between the SAW velocity and the stress and adhesion force indicates that Brillouin scattering is a promising non-destructive technique to characterize the mechanical properties of solid films. For the thinner films, Brillouin scattering measurements of the concerned acoustic modes provide information on the adhesion state between the film and the substrate. For the $TiN/HSS$ system, the measured SAW velocity is always larger than that of the bare substrate, and this shows there is good mechanical contact between the $TiN$ and $HSS$, since otherwise the SAW velocity would drop below that of the substrate for the thinner films.

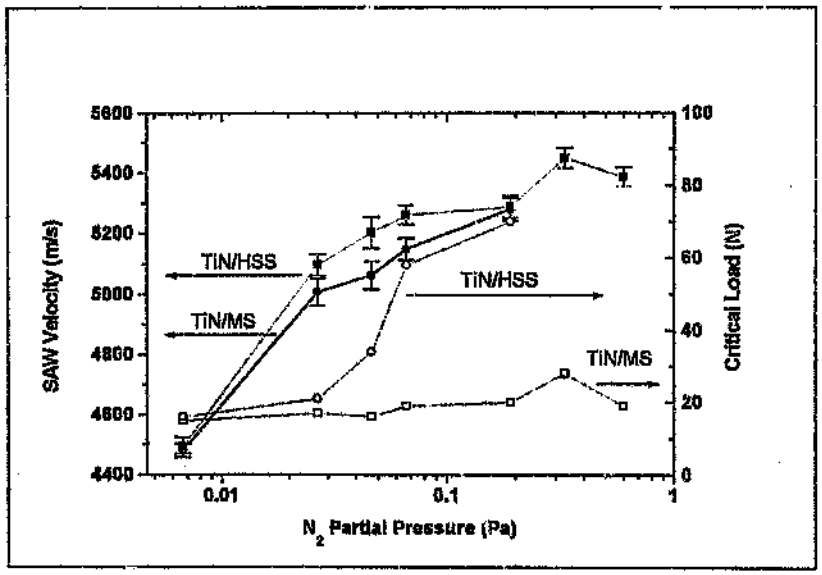


Figure 8.9: Correlation between the measured SAW velocity and critical load of 3.5$\mu m$ TiN films on both high speed and mild steel. The SAW velocity is insensitive to the substrate due to the large film thickness.

## 8.3 High-Temperature Measurements of Elastic Properties of $TiN$ films

### 8.3.1 High-Temperature Measurement Setup

For high temperature measurements the samples were mounted in a specially designed optical furnace (figure 8.10) with rotatable sample holder, and a 120-$mm$ focal length lens of aperture f/5.3 was used to illuminate the sample and collect the scattered light. The sample holder is made of quartz to minimize sample heat loss and variation of sample position caused by thermal expansion. The furnace has a hot zone which is provided by a molybdenum heating coil and surrounded by two cylindrical tantalum heat shells to prevent heat loss. The sample temperature is monitored by a Pt-Pt (13% Rh) thermocouple placed adjacent to the sample. A temperature controller is used to maintain thermal stability of better than $1°C$ during the rather lengthy measurement series. The sample mounted into the quartz holder makes a 70° angle between the sample surface normal and incident laser light. The fused quartz windows allow the Brillouin scattering to be performed in a backscattering geometry. The furnace can be operated in vacuum or an inert gas atmosphere and can reach a temperature of $1200°C$. Our measurements were carried out in vacuum and up to $600°C$. Surface deterioration of the $TiN$ sample occurs after $600°C$, preventing us from measuring the SAW velocity at higher temperatures. The reason for the surface contamination has been found to be associated with the material released from the molybdenum heating coil.

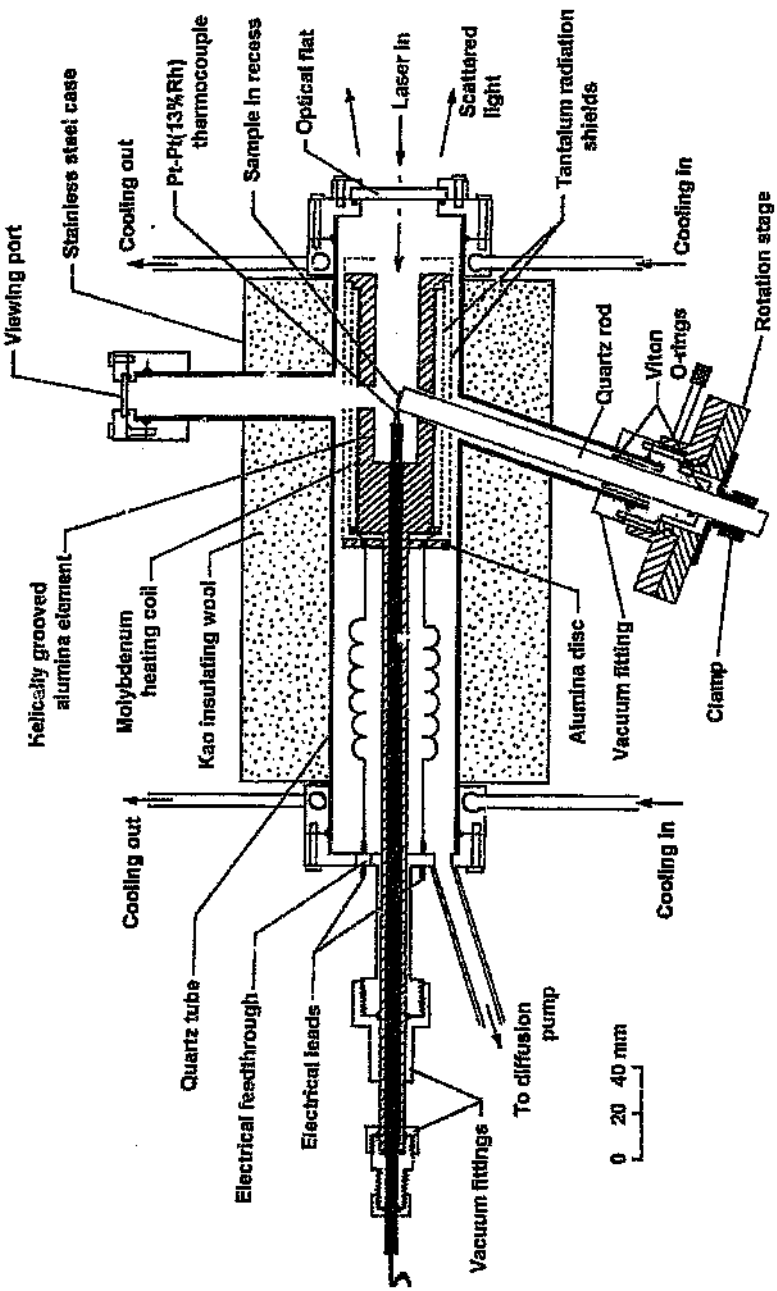


Figure 8.10: Optical furnace used in high-temperature Brillouin scattering measurements.

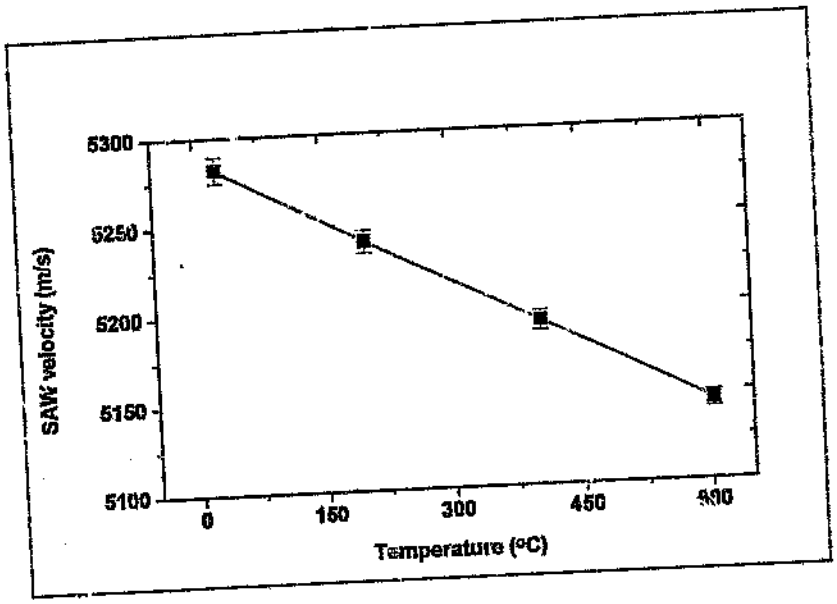


Figure 8.11: Measured SAW velocity as a function of temperature for the $4.18\mu.n$ thick $TiN$ film on $HSS$.

### 8.3.2 Elastic Moduli of Thick $TiN$ Films at High Temperatures

On the basis of the measured Brillouin spectra at high temperatures up to $600^{\circ}C$, the SAW velocity as a function of temperature in the thickest $TiN$ film ($4.18\mu m$) is shown in figure (8.11). A steady reduction in the SAW velocity with increasing temperature is noticeable.

The elastic constants of the $TiN$ films as a function of temperature can be obtained from the measured SAW velocity if Poisson's ratio is assumed to be fixed at 0.2 over the range of temperatures. This is a reasonable assumption for most solids of which

both of the elastic constants $c_{11}$ and $c_{12}$ are a near linear function of temperature. For a thick film which is assumed to be isotropic, we can use equation (4.8) and the Poisson's ratio's expression

$$\sigma = \frac{c_{12}}{c_{11} + c_{12}} = \frac{c_{11} - 2c_{44}}{2(c_{11} - c_{44})} \tag{8.1}$$

to calculate the two independent elastic constants $c_{11}$ and $c_{44}$. In equation (4.8), $v$ is the measured SAW velocity and $v_l$ and $v_t$ are a function of $c_{11}$ and $c_{44}$. The results are shown in figure (8.12). There is a near linear downward trend of the elastic moduli with increasing temperature. Such results are accounted for by normal lattice expansion resulting from anharmonicity [81].

These are, to the best of our knowledge, the first high temperature measurements on the elastic properties of $TiN$ films. There is no ultrasonic data on the elastic moduli of $TiN$ films at high temperatures. Since the working temperature of $TiN$ protective coatings on cutting tools is usually fairly high, this information could be of practical use.

In this chapter, Brillouin scattering measurements have been presented of guided acoustic modes in $TiN$ films on high speed steel ($HSS$) with the film thickness ranging from $20nm$ to $4180nm$, and a highly damped p-SAW and its higher modes identified by the presence of double and multiple peaks in the spectra. Comparison between the measured and calculated dispersion relation indicates that the effective elastic moduli of $TiN$ for the film thickness $< 500nm$ are about 25% smaller than those of bulk $TiN$. A possible explanation for the lowered elastic moduli of the thinner films could be composition variations at the $TiN/HSS$ interface. The good correlation between the

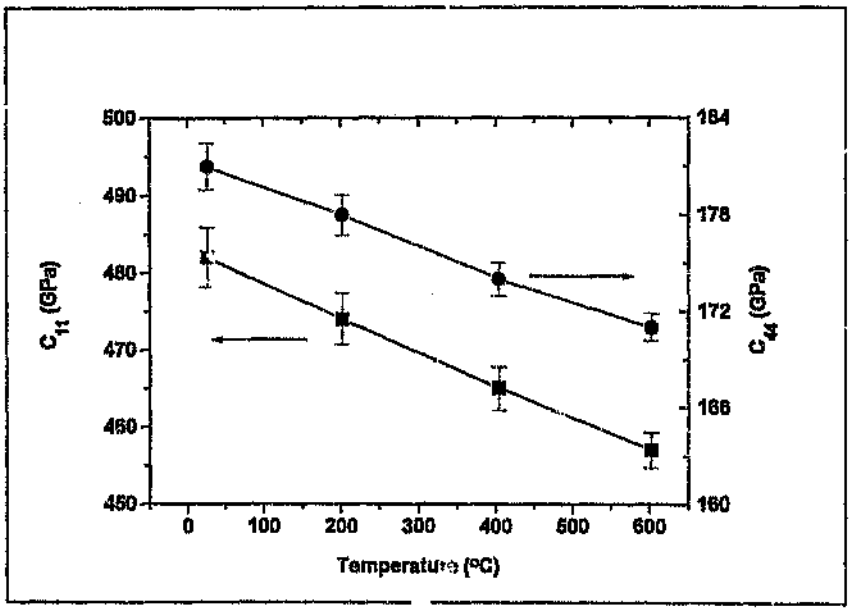


Figure 8.12: The two independent stiffness constants ($c_{11}$ and $c_{44}$) as a function of temperature for the 4.18$\mu m$ thick $TiN$ film on $HSS$.

SAW velocity and residual stress and adhesion force indicates that Brillouin scattering is a promising non-destructive technique to characterize the mechanical properties of solid films. High-temperature measurements of elastic moduli of *TiN* films are also presented.

# Chapter 9

# Conclusion

The acoustic behaviour of a stiffening system has been studied both theoretically and experimentally. The combination of a $TiN$ film on a $HSS$ substrate offers a good example of a stiffening system since the shear velocity of the $TiN$ is much higher than that of $HSS$. The $TiN$ hard polycrystalline films with thickness ranging from 20 to $4180nm$ were deposited on $HSS$ substrates using D. C. magnetron sputtering, making use of a specially designed shutter system to enable the samples to be deposited under exactly the same conditions. $TiN_x$ samples of various stress states were prepared by varying the nitrogen partial pressure in the deposition process involving a Hollow Cathode Discharge Plating. For successful Brillouin scattering measurements, the sample surface needed to be polished to a flatness of $0.05\mu m$ to reduce the elastic scattering intensity.

Physical properties of the films, such as micro-topography, fractography, chemical compositions and preferred texture structure have been investigated by SEM, EDX, X-ray diffraction and Rutherford backscattering, showing that the films have

a homogeneous and (111) preferred orientation texture covering the substrate. The substrate is inhomogeneous in the surface region, where there are $W$ and $Mo$ enriched areas. The X-Ray results also indicate there is stress in films formed in the deposition process. XPS depth profiling reveals that there is a mixing region, with $TiO$ and/or $TiO_2$ being the predominant molecular species at the $TiN/HSS$ interface. This could be a possible reason for the lowered effective elastic moduli of the thinner films that have been studied. The accurate measurement of the thickness of the thinner films has turned out to be a challenging task. We have used several different methods to do the measurement, and the results are essentially in agreement.

The SAW was calculated for a half infinite elastic continuum, using an iterative seeking procedure to determine velocity. Numerical results on the angular dispersion relation were obtained for a single cubic $TiN$ crystal using a coded computer program. The dispersion relation of $TiN/HSS$ has been calculated using a model involving suitable boundary conditions at the free surface and interface. The extension of the calculations to large values of $k_{||}h$ reveals for the first time that there is a highly damped p-SAW in the stiffening system.

Brillouin scattering measurements have been presented of guided modes in $TiN$ films on $HSS$. Because of its relatively high elastic moduli, $TiN$ has a stiffening effect on the surface wave velocity of $HSS$. With increasing $k_{||}h$, the Rayleigh surface wave of $HSS$ increases in velocity and then merges into the bulk wave continuum and becomes a highly damped pseudo-surface acoustic wave. Its higher order modes can also be observed. It is found that the elastic constants of the $TiN$ film play a crucial role in the acoustic behaviour of $TiN/HSS$. There is a discontinuity in the calculated

dispersion curve for normal $TiN/HSS$ - a strong stiffening system, but not for reduced elastic moduli $TiN/HSS$ - a relatively weak stiffening system. However, the acoustic modes in both situations evolve into a "quasi-Rayleigh" wave of the corresponding systems at large $k_{\|}h$, which are very close to the Rayleigh waves of $TiN$.

A Green's function method, invoking the surface ripple mechanism for the inelastic scattering of light, has been used to calculate the Brillouin spectrum for scattering from surface acoustic excitations. Comparison between the measured and calculated dispersion relation for $TiN$ thicknesses ranging from $20nm$ to $4180nm$ indicates that while excellent agreement is found for the thicker films ($> 870nm$) and bare substrates, the measured SAW velocities have lower values than calculated for thinner films (<500nm). This implies that the elastic moduli of the thicker films are close to those of bulk $TiN$, but the effective elastic moduli of the thinner films decrease with reducing film thickness. This conclusion is reinforced by backscattering measurements of Brillouin spectra at incident angles between 50° and 80° for a film thickness of $350nm$, in which p-SAW and its higher order modes are presented as double peaks in the spectrum. Compositional variations at the interface have been investigated using X-ray Photoelectron Spectroscopy (XPS) in an effort to understand this reduction in the elastic constants. All the measured velocities are higher than the Rayleigh velocity of bare substrate showing that there is good adhesion between $TiN$ and $HSS$.

We have also conducted measurements on the SAW velocity of TiN hard films on steel as a function of nitrogen partial pressure used in the deposition process and temperature. Good correlation has been found between the SAW velocity and residual

stress and adhesion force (critical load) of the films. The residual stress in the films has a trend opposite to that of the SAW velocity while the adhesion force has the same trend as that of the SAW velocity. This indicates that Brillouin scattering can be used as a nondestructive method for investigating the stress states and adhesion force of coatings. Brillouin scattering measurements of the elastic properties of thick TiN films at temperatures up to $600°C$ are presented. There is a downward trend of the SAW velocity and hence elastic moduli with increasing temperature, which is explained by normal anharmonic vibrations which lead to lattice expansion.

The averaged elastic constants have been calculated from the known elastic constants of a single crystal for both the random and preferred orientations of crystallites using a tensor averaging method. Computer programs have been coded both for a random distribution of crystallites and polycrystalline aggregates with preferred orientations. It is the first time that algebraic results of the average elastic constants of arbitrary crystal classes have been obtained directly by symbolic computation rather than from an analytical method. The average elastic constants of several polycrystalline hard films are calculated using this method. The calculated results for the $TiN$ polycrytalline film were used to simplify the theoretical model in the calculation of Brillouin spectra and dispersion relation for $TiN/HSS$.

Wave propagation properties in an anisotropic solid have been studied in the context of the slowness surface, from which pure acoustic modes and transonic states can be easily identified. The three dimensional computer visualization of the directionally dependent slownesses of bulk $TiN$ was plotted to show the anisotropic wave propagation behaviour of $TiN$.

Four different methods for inversion of the measured phase velocities of bulk sound waves to optimally recover the elastic constants for the over determined systems of equations have been discussed and compared. The convergence of the algorithms used in the different methods have been investigated through extensive numerical calculations in which suitable "seeking procedures" have been used to minimize recursion times in computation. It is found that some methods are rigorous and can be used in the most general cases, and some others must be used with some caution and great care. All the methods studied here can be applied to wave propagation in arbitrary directions for any symmetry classes of crystals.

Several computer programs have been coded and are available to be used for:

1: symbolically calculating the averaged elastic constants for both a random and a preferred orientation distribution of crystallites;

2: calculating and plotting three dimensional slowness surfaces of crystals.

3: calculating and plotting slowness curves on an arbitrary crystal plane.

4: extracting the elastic constants from bulk mode phase velocities in arbitrary directions for any of the symmetry classes of crystals;

5: calculating and plotting the angular dispersion (Rayleigh velocity vs. propagation direction) curves for a single crystal half space on any crystal plane.

6: computing the dispersion relation (SAW velocity vs. $k_{||}h$) for a supported polycrystalline film.

## REFERENCES

[1] M Ohring, The Materials Science of Thin Films, (Academic Press, New York 1992) 547-587.

[2] M. Wittmer, B. Stuer and H. Melchior, J.Appl. Phys.52(1931) 5722-5726.

[3] B. Karlsson, J. E. Sundgren and B. O. Johansson, Thin Solid Films, 87(1982) 181-187.

[4] L. De Schepper, M. D. Olieslaeger, G. Knuyt, L. M. Stals, M. Van Stappen, B. Malliet, P. Celis and J. R. Roos, Thin Solid Films, 173(1989) 199-208.

[5] J. E. Sundgren, Thin Solid Films, Vol. 128 (1985) 21-44.

[6] E. Török, A. J. Perry, L. Chollet and W. D. Sproul, Thin Solid Films, 153(1987) 37-43.

[7] A. J. Perry, Thin Solid Films, 193/194(1990) 463-471.

[8] A. J. Perry, Thin Solid Films, 170(1989) 63-70.

[9] A. J. Perry and V. Valvoda, Thin Solid Films, 214(1992) 169-174.

[10] J. O. Kim, J. D. Achenbach, P. B. Mirkarimi, M. Shinn and S. A. Barnett, J.Appl. Phys., 72(5) (1992) 1805-1811.

[11] J. O. Kim and J. D. Achenbach, Thin Solid Films, 214 (1992) 25-34.

[12] G. B. Benedek and K. Fritsch, Phys. Rev., 149(1966) 647-662.

[13] M. H. Grimsditch and A. K. Ramdas, Phys. Rev., B11 (1975) 3139–3148.

[14] J. D. Comins, P. E. Ngoepe and C. R. A. Catlow, J. Chem. Soc Faraday Trans. 86(1990)1183-1192.

[15] J. Xu and M. H. Manghnani, Phys Rev. B45(1992) 640-645

[16] P. E. Ngoepe and J. D. Comins, Phys. Rev. Lett. 61(1988) 978-981.

[17] J.R. Sandercock, Solid State Communication, 26 (1978) 547-551.

[18] M. H. Grimsditch, K. E. Gray, R. Bhadra, R. T. Kampwirth and L. E. Rehn, Phys Rev. B35 (1987) 883-885.

[19]R. P. Sharma, R. Bhadra, L. E. Rehn, P. M. Baldo, M. H. Grimsditch, J. Appl. Phys., B66 (1989) 152-155.

[20] M. Mendik, S. Sathish, A. Kulik, G. Gremaud, P. Wachter, J. Appl. Phys., B71 (1992) 2830—2834.

[21] G. Carlotti, D. Fioretto, L. Giovannini, F. Nizzoli, G. Socino, L. Verdini, J. Phys. Cond. Matter, 4(1992) 257-262.

[22] L. Bassoli, F. Nizzoli and J. R. Sandercock, Phys. Rev., B34 (1986) 1296—1299.

[23] M. Mendik, M. Ospelt, H. von Känel and P. Wachter, Appl. Surf. Sci., 50 (1991) 303-307.

[24] B. Hillebrands, P. Baumgart, R. Mock, G. Güntherodt and P. S. Bechthold, J. Appl. Phys., 58(8) (1985) 3166-3169.

[25] G. Carlotti, G. Socino, A. Petri and E. Verona, Appl. Phys. Lett., 51 (23) (1987) 1889-1891.

[26] G. Carlotti, G. Socino and E. Verona, J. Appl. Phys., 65(3) (1989) 1370-1372.

[27] G. Carlotti, D. Fioretto, L. Palmieri, G. Socino, L. Verdini and E. Verona, IEEE, Transactions on Ultrasonics, Ferroelectrics and Frequency Control, 38(1) (1991) 56-60.

[28] M. H. Grimsditch, R. M. Bhadra and I. K. Schuller, Phys. Rev. Lett. 58(1987) 1216-1219.

[29] R. M. Bhadra, M. H. Grimsditch, I. K. Schuller and F. Nizzoli, Phys Rev. B39(1989) 12456-12459.

[30] J. A. Bell, R. J. Zanoni, C. T. Seaton, G. I. Stegeman, J. Mokous, W. R. Bennet and C. M. Falco, Appl. Phys. Lett. 52, (1988) 610-612.

[31] R. Jorna, D. Visser, V. Bortolani and F. Nizzoli, J. Appl. Phys. 65 (1989) 718-725.

[32] R. Zanoni J.A. Bell, G. I. Stegeman and C. T. Seaton, Thin Solid Films 154, (1987) 225-237.

[33] P. R. Stoddart, J. D. Comins and A. G. Every, Phys Rev. B 51 (24) (1995) 17574-17578.

[34] W. Pang, P. R. Stoddart, J. D. Comins, A. G. Every, D. Pietersen and P. J. Marais, Int. J. of Refractory Metals & Hard Materials, 15 (1997) 179-185.

[35] V. Bortolani, F. Nizzoli, G. Santoro and J. R. Sandercock, Phys Rev. B 25 (1982) 3442-3445.

[36] X. Zhang, J. D. Comins, A. G. Every, P. R. Stoddart, W. Pang and T. E. Derry, submitted for publication.

[37] M. H. Grimsditch, E. S. Zouboulis and A Polian, J. Appl. Phys. 76 (1994) 832-834

[38] F. Nizzoli and J. R. Sandercock, Dynamical Properties of Solids, ed. G. K. Horton and A. A. Maradudin, (North-Holland, Amsterdan, 1990) 281-335.

[39] P. Mutti, C. E. Bottani, G. Ghislotti, M. Beghi, G. A. D. Briggs, and J. R. Sandercock, Advances in Acoustic Microscopy, ed. Andrew Briggs, (Plenum Press. New York, 1995) Vol. 1, 249-300.

[40] W. Pang, A. G. Every, J. D. Comins, P. R. Stoddart, X. Zhang, J. C. Crowhurst and D. Pietersen, Review of Progress in Quantitative Nondestructive Evaluation, edited by D. O Thompson and D. E. Chimenti, Vol. 17 (Plenum Press, New York, 1997) in press.

[41] R. Loudon, Phys. Rev. Lett., 40, (1978) 581-583.

[42] A. M. Marvin, V. Bortolani and F. Nizzoli, J. Phys., C(13) (1980) 299-317.

[43] V. Bortolani, A. M. Marvin, F. Nizzoli, and G. Santoro, Solid State Physics 16 (1983) 1757-1776.

[44] V. Bortolani, F. Nizzoli and G. Santoro, Phys. Rev. B 25(5) (1982) 3442-3445.

[45] B. A. Auld, Accoustic Fields and Waves in Solids, (John Wiley & Sons, Inc., New York, 1973) Vol.(1).

[46] G. W. Farnell, Physical Accoustics, ed. W. P. Mason and R. N. Thurston, (Academic Press, New York, 1970) Vol. (6) 112-120.

[47] G. W. Farnell, Topics in Applied Physics, ed. A. A. Cliner, (Springer, Berlin, 1978) 14-60.

[48] G. W. Farnell and E. L. Adler, Physical Acoustics, ed. W. P. Mason and R.N. Thurston, (Academic Press, New York) (1972) Vol. (6) 35-127.

[49] X. Jiang, M. Wang, K. Schmidt, E. Dunlop, J. Haupt and W. Gissler, J. Appl. Phys., 69(5) (1991) 3053-3057.

[50] M. Elena, M. Bonelli, C. E. Bottani, G. Ghislotti, A. Miotello, P. Mutti and P. M. Ossi, Thin Solid Films, 236 (1993) 209-213.

[51] P. B. Mirkarimi, M. Shinn, S. A. Barnett, S. Kumar and M. Grimsditch, J. Appl. Phys., 71(10) (1992) 4955-4958.

[52] V. Aleksandrov, C. E. Bottani, G. Caglioti, C. Ghislotti, C. Marinoni, P. Mutti, N. L. Yakovlev and N. S. Sokolof. J. Phys. Cond. Matter, 6 (1994) 1947-1954.

[53] P. Zinin, O. Lefeuvre, I. Goldfarb, G. A. D. Briggs, B. D. Zeller, P. Cawley, A. J. Kinloch, L. Robert and G. E. Thompson, Proceeding of 1996 IEEE Ultrasonic Symposium (B. M. Levy, S. C. Scheider, ed.), Vol.? (New York), in press.

[54]P. Zinin, O. Lefeuvre, G. A. D. Briggs, B. D. Zeller, P. Cawley, A. J. Kinloch and G. E. Thompson, J. Appl. Phys. 82 (1997)1031-1035.

[55] O. Lefeuvre, P. Zinin and G. A. D. Briggs, Ultrasonics (1998), in press.

[56] O. Lefeuvre, P. Zinin, G. A. D. Briggs and A. G. Every, Appl. Phys. Lett. (1998), in press.

[57] D. B. Bogy and S. M. Gracewski, J. Acoust. Soc. Am.,74 (1983) 591-599.

[58] A. G. Every, W. Pang, J. D. Comins and P. R. Stoddart, Ultrasonics (1998) in press.

[59] W. Pang, A. G. Every, J. D. Comins and P. R. Stoddart, submited for publication.

[60] I. C. Noyan and J. B. Cohen, Residual Stress [illegible] C. Noyan and J. B. Cohen, Spring-Verlag, New York Inc. (1987).

[61] P. Chadwick and G. D. Smith, Mechanics [illegible] ed. H. G. Hopkins and M. J. Sewell, (Pergamon Press, Oxford, 1982), [illegible].

[62] A.G. Every, NDT & E International, 27(1) (1994) 3-10.

[63] A.G. Every, Phys. Rev., B22(4) (1980) 1746-1760.

[64] B. Castagnède, J. T. Jenkins and W. Sachse, J. Appl. Phys., 67(6) (1990) 2753-2761.

[65] J. R. Neighbours and G. E. Schacher, J. Appl. Phys., 38(13) (1967) 5366-5375.

[66] S. Harder, J. Geophys. Research, 90(B12), (1985) 10275-10280.

[67] J. F. Nye, Physical Properties of Crystals, (Oxford University Press, London, 1957).

[68] M. J. P. Musgrave, Crystal Acoustics, (Holden-Day, San Francisco, 1970). 175-185.

[69] R. Hill, Proc. Phys. Soc., A65 (1952) 349-354.

[70] A. G. Every and A. K. McCurdy, Landolt-Bornstein New Series Group III, , ed. O. Madelung, (Springer, Berlin, 1992) vol. 29a.

[71] D. S. Rickerby, A. M. Jones and B. A. Bellamy, Surface Coating Technology. 36 (1988) 661-669.

[72] W. Kress, P. Roedhammer, H. Bilz, W. D. Teuchert and A. N. Christensen, Phys. Rev., B17(1) (1978) 111-115.

[73] C. D. Gazis and R. Herman, Phys. Rev. 119(2) (1960) 533-544.

[74] D. M Barnett, J. Lothe, K. Nishioka and R. J. Asaro, J. Phys. F: Metal Phys., 3 (1973) 1083-1096.

[75] B. Bhushan and B. K. Gupta, Handbook of Tribology: Materials, Coatings, and Surface Treatments (McGraw-Hill , New York, 1991), p. 4.53.

[76] K. R. Subbaswamy and A. A. Maradudin, Phys. Rev. B18, (1978) 4181-4199.

[77] J. R. Sandercock, Light Scattering in Solids, Topics in Applied Physics, ed. M. Cardona and G. Güntherodt, (Springer, Berlin) (1982) 173-306.

[78] J. R. Sandercock, Operation Manual for Tandem Interferometer, (JRS Instruments, Affoltern A. Switzerland, 1993).

[79] S. M. Lindsay, M. W. Anderson and J. R. Sandercock, Rev. Sci. Instr. 52 (1981) 1478-89.

[80] P. R. Stoddart, J. C. Crowhurst, J. D. Comins and A. G. Every, submitted for publication.

[81] J. A. Garber and A. V. Granato, Phys. Rev. B11 (1975) 3990-3997.

# PUBLICATIONS (International)

1. Brillouin Scattering Characterization of Surfaces and Thin Supported Films,

   W. Pang, A. G. Every, J. D. Comins, P. R. Stoddart, X. Zhang, J. C. Crowhurst and D. Pietersen, The 36th Annual British Conference on Non-Destructive Testing, Sept., 1997.

2. Brillouin Scattering as a Tool for Characterizing Surfaces, Interfaces and Thin films,

   W. Pang, A. G. Every, J. D. Comins, P. R. Stoddart, X. Zhang, J. C. Crowhurst and D. Pietersen, The 24th Review of Progress in Quantitative Nondestructive Evaluation, edited by D. O Thompson and D. E. Chimenti, Vol. 17 (Plenum Press, New York, 1997) in press.

3. Elastic Properties of TiN Hard Films at Room and High Temperatures Using Brillouin Scattering,

   W. Pang, P. R. Stoddart, J. D. Comins, A. G. Every, D. Pietersen and P. J. Marais, Int. J. of Refractory Metals & Hard Materials, 15 (1997) 179-185.

4. Brillouin Scattering Study of Guided Modes in TiN Films on High Speed Steel,

   G. Every, W. Pang, J. D. Comins and P. R. Stoddart, Ultrasonics [illegible] in press.

5. Brillouin Scattering from Surfaces, Interfaces and Thin Supported Films-[illegible]uments,

   J. D. Comins, P. R. Stoddart, W. Pang, X. Zhang and J. C. Crowhurst, European Workshop on Surface Brillouin Scattering, Phonons, Magnons and Relaxation Phenomena, Oxford, United Kindom, April, 1997.

6. Surface Brillouin Scattering as a Tool for NDT&E,

   J. D. Comins, A. G. Every, P. R. Stoddart, W. Pang, X. Zhang and J. C. Crowhurst, Trends in NDE Science and Technology, Proceedings of the

14th World Conference on NDT, New Delhi, India 1996, edited by C. G. Krishnadas Nair, Baldev Raj, C. R. L. Murthy and T. Jayakumar, (Oxford & IBH Publishing Co. Pvt. Ltd.), Vol. (3) 1293-1296.

7. The Correlation Between Surface Acoustic Wave Velocity and Mechanical Properties of $TiN_x$ coatings,

   W. Pang, J. D. Comins, A. G. Every and D. Pietersen, submitted for publication.

8. Brillouin Scattering From Acoustic Excitations in $TiN$ films on High Speed Steel - a Stiffening System,

   W. Pang, A. G. Every, J. D. Comins and P. R. Stoddart, submitted for publication.